TECHNISCHE UNIVERSITÄT WIEN

Dissertation

Chemical Vapour Deposition, In-Situ Studies and Ice Nucleation Behaviour of Graphene on Iron/Steels and Copper

Ausgeführt zum Zwecke der Erlangung des akademischen Grades eines Doktors der Naturwissenschaften unter der Leitung von

Assistant Prof. Dr. Bernhard Bayer-Skoff

und

Univ. Prof. Dr. Dominik Eder

Institut für Materialchemie

E165

Eingereicht an der Technischen Universität Wien

Fakultät für Technische Chemie

von

Bernhard Fickl, MSc

01404858

Wien am: _____

Unterschrift

Abstract

Ultra-thin two-dimensional (2D) materials such as graphene have been proposed as exceptionally thin corrosion barriers and functional coatings for contemporary metallurgical alloys. The industrial application of such atomically thin coatings hinges on their direct synthesis on the target substrate and high quality and coverage. However, despite significant research efforts, large-scale monolayer graphene synthesis on complex multi-element substrates, such as steels, has not yet been achieved. Furthermore, even on pure iron direct synthesis of large-scale monolayer graphene remains elusive.

This work addresses the challenges of chemical vapour deposition (CVD) of such 2D materials, particularly graphene, on modern metallurgical alloys. It focuses on the problems of surface oxidation under scalable synthesis conditions and the complex interplay of carbon with the metal substrate. Within the practical part of this work, the CVD synthesis of large-scale high-quality monolayer graphene on iron was achieved. Furthermore, the growth of graphene coatings on a variety of steel substrates was significantly improved. In-situ material characterization methods, such as in-situ near ambient pressure X-ray photoelectron spectroscopy (NAP-XPS) and in-situ X-ray diffraction (XRD), were employed to advance the understanding of substrate surface and bulk behaviour during CVD graphene growth and inform ideal synthesis conditions. Additional characterization, including nano-indentation, revealed that the iron substrate undergoes concurrent surface hardening during CVD graphene growth, demonstrating the ability to incorporate graphene synthesis into industrial carburization hardening processes. Furthermore, graphene's role as an ultimately thin functional coating was investigated with respect to water ice nucleation on monolayer graphene/copper surfaces, revealing a novel, fundamentally interesting phenomenon termed "freezing transparency". Additionally, different graphene functionalization approaches were shown to influence water freezing behaviour, shift freezing temperatures and remove this so-called "freezing transparency".

Kurzfassung

Ultradünne zweidimensionale (2D) Materialien wie Graphen wurden als außergewöhnlich dünne Korrosionsbarrieren und funktionelle Beschichtungen für moderne metallurgische Legierungen vorgeschlagen. Die industrielle Anwendung solcher atomar dünnen Beschichtungen hängt von ihrer direkten Synthese auf dem Zielsubstrat und ihrer hohen Qualität und Bedeckung ab. Bislang ist es jedoch noch nicht gelungen, einlagiges Graphen in großem Maßstab auf komplexen Multielement-Substraten wie Stählen zu synthetisieren. Darüber hinaus ist selbst auf reinem Eisen die direkte Synthese von einlagigem Graphen in großem Maßstab nach wie vor schwer zu erreichen.

In dieser Arbeit werden die Herausforderungen der chemischen Gasphasenabscheidung (CVD) solcher 2D-Materialien, insbesondere von Graphen, auf modernen metallurgischen Legierungen erörtert, wobei der Schwerpunkt auf Problemen der Oberflächenoxidation unter skalierbaren Synthesebedingungen und dem komplexen Zusammenspiel von Kohlenstoff und Metallsubstrat liegt. Im praktischen Teil dieser Arbeit wurde die CVD-Synthese von qualitativ hochwertigem Monolayer-Graphen auf Eisen unter skalierbaren Bedingungen erreicht. Darüber hinaus wurde das Wachstum von Graphenschichten auf einer Vielzahl von Stahlsubstraten deutlich verbessert. In-situ-Materialcharakterisierungsmethoden wie In-situ-Röntgenphotoelektronenspektroskopie bei Umgebungsdruck (NAP-XPS) und In-situ-Röntgendiffraktometrie (XRD) wurden eingesetzt, um das Verhalten der Substratoberfläche und des Volumens während des CVD-Graphenwachstums zu beleuchten und ideale Synthesebedingungen zu ermitteln. Zusätzliche Charakterisierungen zeigten die gleichzeitige Oberflächenhärtung des Eisensubstrats während des CVD-Graphenwachstums, was die Möglichkeit aufzeigt, die Graphen-Synthese in industrielle Härtungsprozesse einzubinden. Des Weitern wurde die Rolle von Graphen als dünne funktionelle Beschichtung im Hinblick auf Eisnukleation von Wasser auf einlagigen Graphen/Kupfer-Oberflächen untersucht, wobei das neuartige Phänomen der „Gefriertransparenz“ festgestellt wurde. Darüber hinaus wurde gezeigt,

dass verschiedene Graphen-Funktionalisierungsansätze das Gefrierverhalten von Wasser beeinflussen, die Gefriertemperaturen verschieben und die Gefriertransparenz aufheben.

Publication List

Primary

1. **B. Fickl**, W. Artner, D. Matulka, J. Rath, M. Nastran, M. Hofer, R. Blume, M. Haevecker, A. Kirnbauer, F. Fahrnberger, H. Hutter , D. Zhang , P. Mayrhofer, A. Knop-Gericke, R. Schlögl, C. Diplot , D. Eder & B. C. Bayer. Realizing Scalable Chemical Vapour Deposition of Monolayer Graphene Films on Iron with Concurrent Surface Hardening by in situ Observations.(2024) -*submitted*

2. **B. Fickl**, T. M. Seifried, E. Rait, J. Genser , T. Wicht , J. Kotakoski , G. Rupprechter , A. Lugstein , D. Zhang , C. Diplot , H. Grothe , D. Eder & B. C. Bayer. Controllable Freezing Transparency for Water Ice on Scalable Graphene Films on Copper. arXiv preprint arXiv:2403.15629. (2024) -*submitted*

3. **B. Fickl**, S. Heinzle, S. Gstoettenmayr, D. Emri, F. Blazevic, W. Artner, C. Diplot , D. Eder & B. C. Bayer. Challenges in Chemical Vapour Deposition of Graphene on Metallurgical Alloys exemplified for NiTi Shape Memory Alloys.(2024) BHM Berg-und Hüttenmännische Monatshefte -*accepted*

4. **B. Fickl** et al. Enabling Chemical Vapour deposition of graphene on steels through in-situ insights. (2024) -*in preparation*

Secondary

5. H. Rabl, S.N. Myakala, J. Rath, **B. Fickl**, J. Schubert, D. Apaydin, D. Eder. Microwave-assisted synthesis of metal-organic chalcogenolate assemblies as electrocatalysts for syngas production. Commun Chem 6, 43 (2023). https://doi.org/10.1038/s42004-023-00843-3 -*published*

6. J. S. Schubert, E. Doloszeski, P. Ayala, S. N. Myakala, J. Rath, **B. Fickl**, A. Giesriegl, D. H. Apaydin, B. C. Bayer, S. Kashiwaya, A. Cherevan, D. Eder. Nature of the Active Ni State for Photocatalytic Hydrogen Generation. Adv. Mater. Interfaces (2024), 11, 2300695. https://doi.org/10.1002/admi.202300695 -*published*

7. M. Nastran, P. Peschek, I. Walendzik, J., **B. Fickl**, J. S. Schubert, G. Szabo, R. A. Wilhelm, J. Schmidt, D. Eder, B.C. Bayer. Liquid phase exfoliation of graphene using ammonia as easy-to-remove additive in low-boiling organic-water co-solvent suspensions. -*submitted*

8. J. Rath, **B. Fickl**, D. Matulka, N. Isufaj, H. Kählig, C. Mangler, J. Kotakoski, A. Cherevan, S. Naghdi, A. Giesriegl, S. Schwarz, M. Stöger-Pollach, M. Sauer, A. Foelske, B. C. Bayer, D. Eder. Atomic layer deposition of conformal Ti-MIL-125-like metal organic framework ultrathin films on nanoscaled substrates towards photocatalysis. -*submitted*

Articles 1-4 are based on work in this thesis.

Acknowledgments

This work is the result of hard work and determination but could have never been accomplished without the support and encouragement of many individuals. I am deeply grateful to everyone who has accompanied me on this journey and for the guidance and motivation they provided.

First and foremost, I want to thank Assistant Prof. Dr. Bernhard Bayer-Skoff for the supervision of my PhD project. His unwavering support and great scientific ambition have been a constant source of motivation for me, and it is safe to say that this work would not have been possible without him. In the same vein, I express my sincere gratitude to Professor Dominik Eder for providing the research environment in which this work has been produced and for his continued support and guidance, which have helped me reach my scientific goals.

I want to explicitly thank my students, Filip Blazevic, Dorian Emri, Stephanie Gstöttenmayr, Samuel Heinzle and Daniel Matulka, which I had the pleasure of supervising for their bachelor projects and who have contributed directly and indirectly to this work with their dedication in the lab. My special thanks go to Erwin Rait, who, during his internship, displayed remarkable motivation towards his project. In the same spirit, I would like to highlight Daniel Matulka's exceptional capabilities as a chemist and his independence in the lab.

I want to acknowledge scientific contributions to this work from: Werner Artner (TU Wien X-Ray Center) in form of dedicated assistance when facing any practical challenge and in particular with XRD measurements; Erwin Rait (TU Wien) for the design

and implementation of the algorithm for automatic freezing event detection used in chapter 5; Alex Kirnbauer and Paul Mayrhofer (TU Wien) for the nanoindentation measurements and analysis; Florian Fahrnberger and Herbert Hutter (TU Wien) for TOF-SIMS measurements and analysis; Teresa Seifried and Hinrich Grothe (TU Wien) for providing the ice-nucleation experimental setup and assisting in ice nucleation measurements; Jakob Genser and Alois Lugstein (TU Wien) for the SF_6 -plasma functionalisation of graphene surfaces and specific Raman measurements related to these samples; Thomas Wicht and Günter Rupprechter (TU Wien) for XPS measurement and analysis of SF_6 -funcionalised graphene surfaces in chapter 5; Jani Kotakoski (University of Vienna) for the initial use of the CVD setup at the University of Vienna; Robert Schlögl, Raoul Blume, Michael Hävecker, Axel Knop-Gericke and Beatriz Roldán Cuenya (Fritz-Haber-Institut) for establishing the in-situ NAP-XPS setup, for assistance during measurements and for access to the facilities at the EMIL endstation at BESSY II synchrotron (Berlin); Virginia Pérez Dieste and Nacho Villar (ALBA) for maintenance of the in-situ NAPP endstation (CIRCE) and assistance during measurements at ALBA synchrotron (Barcelona); my collegues, Jakob Rath, Markus Hofer, Martin Nastran, Bodo Baumgartner and Daniel Matulka for assisting in the in-situ NAP-XPS measurements at the synchrotron radiation facilities in Berlin (BESSY II) and Barcelona (ALBA).

I want to acknowledge the financial support provided by the Austrian Research Promotion Agency (FFG) through the project 879844-HARD2D and the partial funding of the European Research Council (ERC) through the project 101088366-HighEntropy2D, which made this research possible. I also acknowledge the input from, and good cooperation with, the industrial partner RÜBIG GmbH & Co. KG (Dr. Christian Dipolt) through FFG HARD2D. I furthermore thank the Helmholtz-Zentrum Berlin für Materialien und Energie for the allocation of synchrotron radiation beamtime at BESSY II and likewise the ALBA synchrotron Barcelona for provision of synchrotron radiation.

I want to extend my thanks to the whole research group at TU Wien for providing a friendly and nourishing environment that made me feel welcome and provided a space for me to grow as a scientist.

On a personal note, I would like to explicitly thank Jakob Rath for his help navigating the university landscape from day one and making my time at TU Wien most enjoyable. I am very grateful for being able to call him my friend.

Above all, I want to thank my family for their support during this time, for my loving upbringing that has shaped me into who I am today and for giving me the tools to accomplish my goals and my partner, Valentina, whose compassion and unwavering belief in me have been an indispensable source of motivation and emotional support.

Contents

CHAPTER 1

INTRODUCTION

1.1 Motivation

Metals have long played a central role in human civilisation and are essential components of our electronics and infrastructure today. As a result, they are frequently subjected to harsh conditions that can degrade their properties and inhibit their intended functionality. This not only results in tremendous upkeep and replacement costs but can, in the worst case, lead to catastrophic failure resulting in damage to ecosystems and the loss of life. The need to protect metallic material surfaces from their surrounding environment, therefore, has a long history and has resulted in a variety of protective methods. These include passive strategies like paints or coatings and more active approaches, such as anti-icing-[1] or corrosion-inhibiting[2] chemical compounds or impressed current cathodic protection (ICCP).[3]

With its remarkable properties such as record high electrical conductivity,[4] mechanical stability[5] and barrier capability,[6,7] graphene has been the focus of decades of research with the aim to harness its promising capabilities. The discovery of graphene as a stable, free-standing, atomically thin membrane kickstarted the field of 2D materials, with a multitude of different two-dimensional materials being discovered and analysed. However, integrating two-dimensional materials, including graphene, into usable systems and practical devices has proven to be more challenging than anticipated. This is due to, among other reasons, non-compatible high process temperatures required for 2D

material synthesis, difficult transfer and handling requiring novel industry procedures, and difficulties in integrating these materials into existing manufacturing systems.[8]

This work contributes to integrating and applying 2D materials, specifically graphene, by investigating the fundamental environmental interaction of ice nucleation on graphene and scalable large-area synthesis of high-quality graphene on previously prohibitively challenging substrates such as iron and steel. It, therefore, examines graphene in the context of an ultimately thin functional barrier coating for different metal substrates. This thesis is structured into three distinct overarching chapters constituting three scientific works.

The first chapter details the synthesis of large-scale, high-quality monolayer graphene (MLG) on iron via scalable chemical vapour deposition (CVD). This, previously not realised, advance constitutes an important step towards incorporating graphene into corrosion barrier applications for iron-containing metals. Here, we also discuss the fundamental challenges in chemical vapour deposition of graphene on metallurgical substrates.

The second chapter uses the findings of the successful graphene growth on iron to expand the approach to three archetypal steel substrates of increasing complexity. This chapter focuses on surface characterisation via in-situ near ambient pressure X-ray photoelectron spectroscopy (NAP-XPS), enabled by synchrotron radiation facilities, during the CVD graphene growth process.

The third chapter investigates graphene as a potential passive anti-icing coating on copper. It reveals a previously unreported “freezing transparency” phenomenon and investigates graphene functionalisation as a route to control water droplet freezing temperatures.

Additionally, in the appendix, the challenges associated with the chemical vapour deposition (CVD) of graphene on complex metallurgical substrates are discussed, exemplified by graphene CVD on the shape memory alloy nitinol (NiTi).

1.2 Background on Graphene

1.2.1 Structure and Synthesis

Graphene is a single layer of carbon atoms arranged in a hexagonal lattice. As a sheet of atomic thickness, it is considered a two-dimensional (2D) material and the basic building block of many carbon allotropes, including graphite (3D), carbon nanotubes (1D) and fullerenes (0D), visualised in figure 1.1. Elemental carbon can, in general, exist in three hybridisations, namely sp^1, sp^2 and sp^3.[9,10] This hybridisation of the four valence electrons of carbon leads to the stark differences in carbon allotropes such as diamond (sp^3) and graphite (sp^2). While sp^3-hybridized carbon atoms form tetrahedrally directed covalent σ-bonds leading to a strong network and an electrically insulating material, carbon in a sp^2-hybridized state forms three covalent σ bonds, arranged trigonally within one plane, with the fourth electron forming a π orbital directed perpendicular to it, which leads to high electrical conductivity within the sheet. A sketch of the graphene lattice with its two unit-cell vectors a_1 and a_2 of the same length and the unit cell itself is shown in figure 1.2

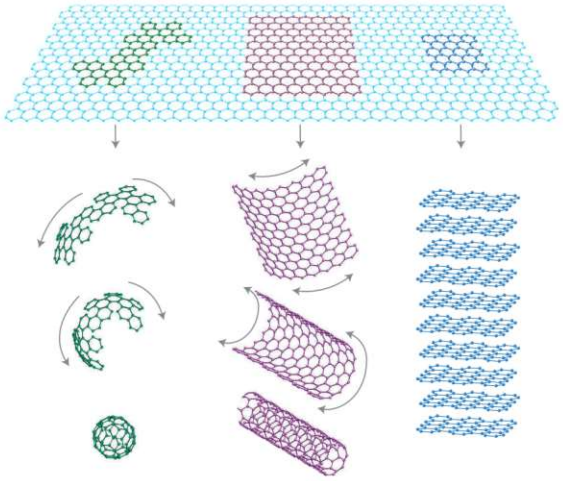

Figure 1.1: Graphic visualisation of graphene as the building block for different carbon allotropes (left: fullerene, middle: nanotube, right: graphite). (Figure adapted from Geim and Novoselov.[11])

The covalent π bonds formed between neighbouring atoms provide the weak van der Waals interaction between adjacent individual layers in the graphite structure[12] and in MLG give rise to the unique band-structure with zero band gap, that allows for ballistic transport of massless Dirac fermions over a sub-micrometre scale.[11,13,14] These quasiparticles follow a linear dispersion relation $E = \hbar k \nu_F$ around the K and K' points

of the Brillouin zone and are described as relativistic massless particles by the Dirac equation. Graphene is therefore often referred to as a semi-metal or zero-bandgap semiconductor.[13–15] This band-structure provides graphene with very high electrical and thermal conductivity (up to 5300 W/mK)[16] as well as high charge carrier concentration (n = 10^{13} cm^{-2})[11] and mobility (μ = 15000 cm^2/Vs)[13]. Graphene's crystal structure and chemical bonding configuration lead to its very high mechanical strength and elasticity (Young's modulus E = 1 TPa)[5]. This mechanical resilience is also evident in experiments investigating graphene as a membrane[6], which show the impermeable nature of single-layer graphene.[7]

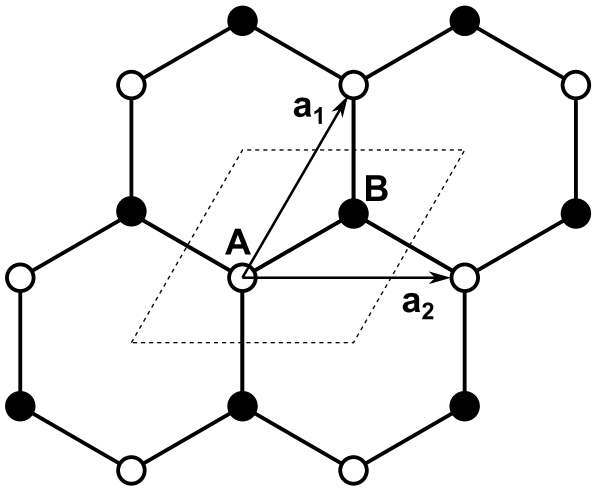

Figure 1.2: Sketch of graphene crystal lattice, where A and B denote carbon atoms of the two sub-lattices and a_1 and a_2 indicate the unit vectors. The dashed parallelogram indicates the unit cell.

Novoselov and Geim first stabilised and electrically characterised graphene in 2004.[4] It promised to revolutionise several major industries with its record-breaking properties, which are well-suited for applications in electronic devices, chemical sensing, nanocomposites and energy storage.[17] For example, the use of graphene in field-effect transistors (FET) has been a major focus of research ever since its conception, but as predicted[11] a commercial graphene microprocessor is still not viable 20 years after graphene's first synthesis. The extended time and effort required for graphene and other 2D materials to transition from laboratory research to industrial applications is, among other factors, limited by the availability of scalable synthesis routes for truly monolayer materials.

Graphene and most other 2D materials can be synthesised by two different basic approaches, which are commonly referred to as top-down or bottom-up. The top-down method takes the bulk graphite and separates the individual layers by either mechanical or chemical means. The bottom-up method takes carbonaceous precursors and assembles

the carbon into a single layer by chemical and thermal processes. For both strategies there are multiple different methods which lead to different outcomes regarding quality, crystal domain size and yield.

The most common top-down techniques for graphene synthesis are micro-mechanical cleavage and liquid phase exfoliation. Micro-mechanical cleavage (also called the scotch tape method) was used to produce monolayer graphene for the first time in 2004.[4] It uses regular scotch tape to cleave highly ordered pyrolytic graphite (HOPG) crystals with repeated manual exfoliation. By repeatedly pressing and peeling the tape from the graphite surface, individual layers of graphene are isolated and can be transferred onto silicon dioxide wafers of specific thickness for optical identification. This simple yet effective method enabled the initial discovery and investigation of graphene's remarkable properties and is applicable for all layered 2D materials e.g. 2D-transition metal dichalcogenides (TMDs).[18,19] This led to extensive fundamental research and promised advancements in various fields such as electronics, energy storage, and biomedical devices.[11,20] The scotch tape method remains a fundamental technique for producing high-quality graphene samples in research, despite advancements in other fabrication methods. However, due to its lack of scalability and its limitation to single-flake production, it is commonly not applied outside of the research context.

Another top-down technique, called liquid phase exfoliation (LPE), isolates individual layers of graphite by exploiting the phenomenon of micro-cavitation bubbles created by ultrasound in a liquid.[21,22] This method involves dispersing graphite flakes within a liquid solvent, often with the addition of surfactants or stabilising agents, and subjecting the suspension to ultrasonic waves. The intense agitation induced by the ultrasound leads to the formation and collapse of micro-cavitation bubbles within the liquid, applying shear forces onto the graphite flakes and causing them to exfoliate into thinner layers. LPE offers several advantages, including the ability to produce large quantities of graphene dispersions with controlled layer numbers and the versatility to use various solvents and additives to tailor the properties of the resulting graphene nano-sheets. This technique has the potential for the scalable production of graphene-based materials and has, therefore, received considerable research attention.[22–24] It, however, does not produce large-area, high-quality single-layer graphene but rather a suspension of few-layer nano-sheets with varying sizes. These 2D-material suspensions have a high amount of surface area and reactive edge sites and could be used in catalysis[25,26] or further processed into functional sprayable coatings[27] or printable inks.[28]

The primary bottom-up technique to effectively grow graphene is chemical vapour deposition (CVD) (discussed in more detail in section 1.2.3), specifically low-pressure CVD (LPCVD) using catalytically active metal substrates. This approach uses carbon-containing precursors that decompose into carbon radicals on the catalyst surface at elevated temperatures, facilitating self-assembly into ordered graphene layers. Multiple parameters, such as growth temperature, growth time, precursor partial pressure, gas composition, and choice of substrate, affect the growth mechanism and overall quality of the 2D material.[29] In particular, the effect of the substrate on graphene growth is important in 2D material synthesis via CVD and is discussed more thoroughly in section 1.2.4. CVD has proven to be a viable method to produce large area (meter-scale) single crystal monolayer graphene on copper (Cu),[30] reaching comparable quality to mechanically exfoliated graphene, but far exceeding it in film size and production scalability.

1.2.2 Graphene as Ultrathin Functional Coating

Graphene's mechanical and chemical stability, high conductivity, chemical inertness and barrier capability, while being completely transparent, make it an excellent candidate for a coating material with a diverse range of applications. The possibility to tune its functionality by tailoring its structure, such as doping with hetero atoms or incorporating functional groups, further expands graphene's potential as a versatile coating.[31–33] In principle, a defect-free single layer of graphene provides a significant energy barrier to prevent the penetration of atoms and molecules. Even small defects do not significantly reduce this barrier capability.[34,35] Both experimental[6,7] and computational[34,36] works have demonstrated graphene's complete impermeability to atoms and molecules larger than a single hydrogen atom. This, together with its other properties, makes it an attractive candidate for a protective corrosion coating in stationary applications such as batteries, fuel cells, implantable devices and highly corrosive environments such as desalination plants or nuclear waste containers.[37]

Graphene, as a monolayer, has been shown to decrease corrosion rates of Cu and Ni substantially,[38] and as a multilayer, even improved the corrosion resistance of stainless steels.[39,40] These experiments, however, have investigated mostly short timescales and there is significant evidence that, on longer timescales (months), graphene can accelerate and cause localised corrosion.[41,42] This is due to the fact that graphene generally has substantial defects like grain boundaries when grown via CVD. These defect sites act as starting points for local corrosion, which can be accelerated by the high conductivity of the graphene coating and subsequently lead to stress and crack formation in the

material, further enabling corrosion to take place.[43] This galvanic corrosion problem can be circumvented by using an insulating two-dimensional material, such as hexagonal boron nitride (hBN).[42] However, this solution is not optimal for energy applications, where the high electrical conductivity of graphene is of obvious practical significance. In general, the corrosion protection capability of graphene strongly decreases with the increase in defects and inhomogeneities of the film. For instance, using transferred graphene significantly reduces the protection potential compared to graphene grown directly on the substrate. This is due to induced wrinkles, adsorbed contamination and damage to the film from the transfer procedure, which decrease the interaction between the graphene and the substrate and result in pathways for corrosion. These drawbacks are linked to the use of monolayer graphene as an ultimately thin protective barrier, which is why approaches using exfoliated multilayer graphene[44] or graphene/graphene oxide nanocomposite materials[45,46] have been proposed. While this has shown good results in corrosion protection, the potential of graphene as an ultimately thin barrier is somewhat diminished when applied in a micrometer thick coating. The optimal application of monolayer graphene as a barrier layer would involve minimal alteration of the underlying metal surface while providing protection and good electrical conductivity, in particular for fuel cell or battery applications. Therefore, the need arises to produce high-quality (ideally single crystal) monolayer graphene films on a large scale, directly on application-relevant substrates such as Cu, Ni, Fe and steel.[47]

1.2.3 Chemical vapour deposition introduction

The process of chemical vapour deposition (CVD) in general uses a volatile compound in combination with other gases, which undergoes chemical reaction and results in the deposition of a non-volatile solid on a specific substrate.[48] This usually happens at high temperatures (1000 °C) and can occur in either the gas phase or at the surface of the substrate. In general, a thin solid coating is deposited via CVD.[49] The substrate surface can play a vital catalytic role in some deposition processes as is discussed in subsection 1.2.4. The CVD process is of high industrial significance in particular in the semiconductor and ceramics industry.[48,49]

The chemical reactions involved in CVD can be categorised into four principal reactions.[48] (I) Pyrolysis describes the thermal decomposition of gaseous reactants, which typically results in the production of elemental species that can subsequently react in secondary reaction steps. This can happen either spontaneously in the gas phase at high temperatures or be enabled by the catalyst substrate. In our case, the hydrocarbon precursor gas breaks apart at the metal catalyst substrate to leave behind carbon moieties that can

form graphene. (II) Reduction, often facilitated by hydrogen gas, can be used to deposit tungsten (W) or molybdenum (Mo) films by reducing the respective hexaflourides (WF_6, MoF_6).[48] In our CVD process, hydrogen is mainly used to reduce the native metal oxide layer of the metal substrates, thereby keeping the substrate catalytically active. Furthermore, the hydrogen plays a vital double role in CVD graphene growth by forming active surface-bound carbon species $(C_xH_y)_n$ required for graphene growth and through etching away loosely bound carbon, facilitating ordered growth.[50] (III) Oxidation is used to produce oxide material deposits, usually by letting oxygen gas react directly with a precursor compound in the gas phase. In our CVD process oxygen plays a detrimental role as an unwanted species present in our system. It can form surface metal oxides on our substrate, decreasing catalytic activity and directly competing with graphene growth. (IV) Compound formation can take place directly in the gas phase by reacting two precursor gases to form a solid material coating by deposition. The prerequisite for this is the sufficiently reactive gaseous precursors. This reaction path is generally used to produce carbide, nitride and boride films.[48] In our CVD process direct compound formation does not take place as we only use one carbon containing precursor gas and our main reaction takes place on the metal catalyst surface.

CVD can be categorised via its process condition into high-pressure- (above atmospheric), atmospheric pressure-, low-pressure- (below atmospheric) and ultrahigh vacuum ($<10^{-8}$ mbar) CVD, each having different use cases and industrial significance, with low-pressure CVD being an integral part of modern semiconductor manufacturing.[48] The CVD process can additionally be assisted by plasma, which enhances reactivity and allows for lower process temperatures.[48] CVD benefits form the ability to utilise a wide variety of chemical precursors and can therefore be used to produce a large variety of material coatings, including metals, ceramics, carbides, nitrides, oxides, sulphides and even polymers.[49] Importantly for this work, CVD can also be used to synthesise 2D materials[51] or other nanomaterials such as carbon nanotubes.[52]

The general working principle of CVD, broken up into general steps, is illustrated in figure 1.3.[49] The following steps involved in chemical vapour deposition (corresponding to the numbers in figure 1.3) have been adapted from Xu et al.[49] but were previously already discussed.[53,54]

1. The mass transport of gaseous reactants close to the substrate;

2. Diffusion of the reactant species towards the substrate surface through the boundary layer (boundary layer is defined as the non-flowing gas volume region in close

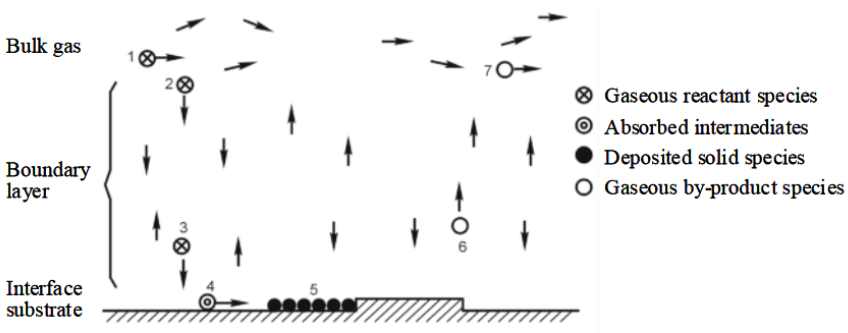

Figure 1.3: Schematic of CVD technique, showing the principle species participating in the process. (Adapted from Xu et al.[49])

proximity to the substrate surface[48]), or gas-phase chemical reaction to form intermediates;

3. Adsorption of reactant species or intermediate reactants on the substrate surface;
4. Surface diffusion/migration and/or (sometimes catalytic) chemical reaction on the surface followed by either incorporation into the developing surface coating or the formation of by-product species;
5. Desorption of by-product species from surface reactions;
6. Diffusion of the by-product species back through the boundary layer into the flowing bulk gas;
7. Transport of by-product species away from the substrate and into exhaust.

An additional step in the CVD process, not addressed in the schematic in figure 1.3, is the possible interaction of the growth atoms with the substrate material and diffusion into the substrate, bulk[55,56] which has implications for the here conducted CVD and will be further discussed in the following sections and throughout this work.

Because of the fact that the CVD process can involve multiple gaseous precursors and complicated reaction steps with a variety of intermediate species, it is considered a quite complex deposition method that needs experience and repeated test runs in order to produce the desired result.[49] Generally, the intermediate species participating in the reaction are extremely difficult to identify, making it nearly impossible in most cases, to have a complete mechanistic understanding of the whole CVD process.[49] Nevertheless, with precise control over growth parameters such as temperature, growth/exposure times, gas flows and partial pressures and correct selection of reaction gases and substrates, a wide variety of material coatings can be reliably realised.

1.2.4 Chemical vapour deposition of graphene on elemental metal catalyst substrates

CVD has evolved into the primary synthesis method for few- and monolayer graphene and 2D materials in general, due to its scalability and industrial compatibility.[57] In contrast to most classical CVD where precursors react in the gas phase prior to deposition on a substrate, CVD for 2D materials utilises the catalytic ability of the deposition substrate to break down precursors on its surface.[56,58–61] Catalytically active transition metals such as Cu, Ni, Pd, Ru, Ir or Fe have all been used to grow graphene via CVD with varying quality. For 2D material synthesis via CVD, the substrate plays an active and vital role in the growth process. The solubilities of the 2D material constituent elements, the crystal domain orientation and the catalytic activity of the substrate can substantially influence the resulting 2D material quality. For example, the solubility of carbon in copper is, at 0.008 wt%, very low, leading to an exclusively surface-mediated and self-limiting growth process of overwhelmingly monolayer graphene.[62] With the control of the crystalline orientation of the copper substrate towards a Cu(111) single crystal, graphene single crystal growth over a meter scale has been achieved.[30,63,64] Therefore, copper is the most widely used catalyst for monolayer graphene growth via CVD.

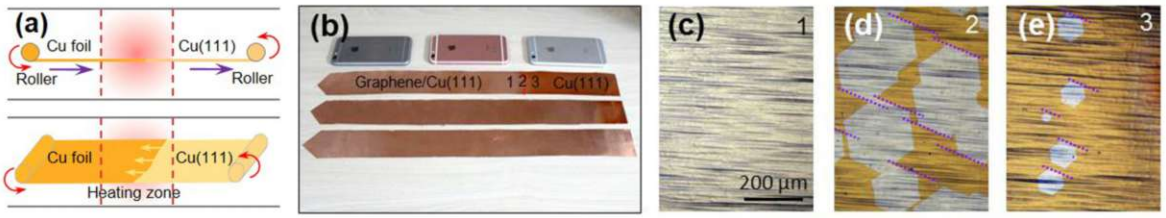

Figure 1.4: Figure to illustrate highly scalable production of large-scale single-crystal monolayer graphene on copper via CVD. (a) Schematic of experimental design for the continuous production of single-crystal Cu(111) foil with a hot temperature zone at the center of the furnace tube. (b) Cu(1 1 1) foils with graphene coverages of ~60 % (top), ~90 % (middle) and 100 % (bottom). (c-e) Optical images representative of regions marked in (b) with 1-3 respectively showing areas (c) fully covered by graphene, (d) covered by large aligned graphene islands and (e) covered by small aligned graphene islands. (Adapted from Xu et al.[30])

In comparison, nickel has a greater carbon solubility and tends to incorporate carbon in its bulk during precursor exposure at elevated temperatures. Upon cooling the substrate, the decrease in carbon solubility can cause precipitation growth, where excess carbon is forced to the surface, resulting in non-homogeneous growth with multiple layers. This effect is highly dependent on the cooling rate and can be minimised by decreasing the

growth temperature. Nevertheless, the main graphene growth mechanism on nickel is isothermal surface-mediated growth.[60] This growth characteristic implies the possibility for large-scale monolayer graphene (MLG) growth on nickel by ensuring this to be the dominant growth mode. And indeed, by controlling growth parameters such as pressure, temperature and precursor it is possible to grow high quality MLG on nickel substrates.[65,66]

The use of iron as a substrate for graphene growth via CVD would theoretically be justified by a very close match in lattice constant between ferritic iron (2.86 Å) and graphene (2.46 Å).[67] In reality, the high carbon solubility of iron and its complex phase diagram make it a challenging substrate for graphene growth. Furthermore, while Ni only forms metastable carbides, that decompose upon cooling, in iron the formation of iron carbide can compete with the graphene formation, adding to the complexity of the growth process.[68,69] The phase change from α-Fe body-centered cubic (bcc) to γ-Fe face-centered cubic (fcc) leads to a huge change in carbon solubility from 0.022 wt% to 0.8 wt% at its eutectoid at 723°C and up to 2.14 wt% at 1147°C.[67] The common understanding is that the iron takes up large amounts of carbon in its austenitic fcc phase during precursor exposure and, during cooling, precipitates this dissolved carbon to the surface to form graphene. Simultaneously the remaining carbon in the subsurface and or bulk of the iron substrate may form iron carbide (Fe_3C) under the right conditions.[70] It is important to note that phase transitions not only depend on the obvious parameters of temperature and carbon concentration but can also be profoundly affected by elemental contamination or alloying elements.

Even before the analysis of graphene by Novoselov and Geim in 2004,[4] a work investigating the phases formed in the iron carbide process likely formed a graphene-like coating on iron, by exposing it to an Ar-H_2-CH_4 gas mixture at 750 °C to 925 °C, without identifying it as graphene and contemplating the origin of the unusual Raman signature with an intense D band overtone at 2700 cm^{-1}.[71] With the stated goal of graphene synthesis, high-quality few-layer graphene (FLG) on iron, with complete coverage, was synthesised via CVD in 2011[67] using methane as a precursor and a growth temperature of 920 °C. And monolayer graphene (MLG) has been grown on Fe(110) single crystal films under UHV conditions.[72] Under scalable conditions, only partial coverage, low-quality graphene with inhomogeneous layer numbers has been achieved.[70,73–77]

High-quality monolayer graphene films on iron were also synthesised using a non-CVD approach termed "segregation method". This method uses either trace amounts of

carbon in a metal film[78], or a solid carbon feedstock beneath a thin evaporated Fe film[79]. The carbon diffuses through the film at elevated temperatures and segregates on the surface, ultimately forming graphene. This method produces good-quality graphene with precise layer control but is not applicable to bulk samples and has also only been shown to work under non-scalable conditions.

1.2.5 Chemical vapour deposition of graphene on metal-alloy substrates

Two-dimensional (2D) materials including graphene, are of key interest as ultimately thin functional coatings for modern metallurgical alloys.[20,39,47,80,81] This is because, as mentioned before, graphene offers virtual impermeability to gases, liquids and ionic species, suggesting it as an ultimately thin corrosion barrier material.[6,7,39] Graphene is also chemically inert, temperature stable and has good biocompatibility.[20,39,47,80–86] Additionally, when its properties are normalised to its atomic thinness, graphene is an exceptional electrical conductor, has high thermal conductivity and exhibits extraordinary mechanical properties,[20,39,47,80,81] incl. being the strongest crystal reported to date, while still displaying significant mechanical flexibility[20,80] and under some conditions superlubricity,[87,88] which suggests sufficient durability in metallurgical (low wear) applications.

Despite this, the actual realisation of graphene as ultrathin functional coating on metallurgical alloys has so far turned out challenging.[47,81,89–98] The dichotomy between reported record graphene properties and its, by comparison, lower performance in metallurgical testing results from the to-date still insufficient control over scalable graphene growth in metallurgical application scenarios.

Growth of 2D materials incl. graphene on metallurgical alloys remains an unsolved challenge.[40,47] It requires good interfacing and control over 2D materials' defect levels, chemical compositions, layer numbers, lateral crystal sizes, homogeneity and coverage. Homogeneous coverage over complex three-dimensional shapes, heterogeneous alloy microstructures, across polycrystalline substrate grains and over µm-surface roughness is essential, as is eventual industrial scalability. Importantly, alloy bulk microstructure and thus bulk functionality must not be degraded during 2D materials growth.[40,47,99]

As mentioned in section 1.2.4, CVD has enabled the growth of high-quality graphene and

other 2D materials films (e.g. 2D hexagonal boron nitride), but so far only on dedicated high-purity metal growth catalyst supports with simple microstructures (e.g., Cu, Ni, partly Fe[58,60,61,100–102]). Their microstructures do not have to be retained during growth, as subsequently 2D materials are often removed from the catalysts and transferred to other device stacks. A simple translation of the progress on dedicated high-purity catalysts to modern metallurgical alloys is however difficult for two key reasons.

The first reason is the required active role of the growth substrate in 2D materials CVD via surface catalytic activity.[58,60,61,100–103] Close matching of substrate properties and 2D CVD conditions (temperature profiles, precursor fluxes, pre-treatments etc.) is required for each substrate individually.[56,59] Already for the dedicated high-purity catalysts this matching has been a formidable (but now well addressed) challenge.[104] For the much more complex heterogeneous microstructures of modern metallurgical alloys such matching remains much more elusive. Even minor changes in composition and microstructure can drastically change (and often deteriorate) 2D material growth results. Generally, CVD of graphene on catalytically active metals such as Ni, Co, Fe and Cu is much more readily achievable but already becomes more difficult when additional alloying elements are added to the substrate (which is the case in practically all modern metallurgical alloys). Furthermore, the CVD of graphene on strong carbide formers like refractory Ti or Ta is more challenging, as carbide formation from the carbon influx of gaseous hydrocarbon precursor breakdown at elevated temperatures might be favoured over graphene nucleation.[91,105] Refractory substrates are also difficult to coat with graphene because the substrates readily form oxides with the residual oxygen and water in scalable CVD systems, whereby oxide formation often further impedes graphene CVD that typically requires reduced metallic state to be catalytically active for growth.[106] For these reasons, individual (re-)calibration of 2D materials CVD conditions may be necessary for every different alloy composition.

The second reason is that the microstructure of the underlying metallurgical alloy often needs to be preserved during the CVD process of 2D materials. Otherwise, the successful deposition of a 2D material such as graphene on a metallurgical alloy can lead to an overall functional degradation of the 2D material/support stack. This can occur if the underlying metallurgical substrate undergoes significant microstructural changes during the high-temperature CVD process due to diffusion of alloying elements at elevated temperatures and/or infiltration of 2D material constituents (e.g., carbon for graphene) into the catalyst, which can lead to detrimental effects on substrate properties such as mechanical strength. On the other hand, if the substrate microstruc-

ture and/or phase change during CVD graphene growth can be fully understood and controlled, the CVD process could positively influence the substrate property, e.g. by surface hardening through carburisation. This second aspect of controlling the metallurgical substrate microstructure has received little attention in 2D materials work so far.

The promise of graphene as an ultrathin corrosion barrier is particularly exciting for applications on more complex metal alloys, such as stainless steel (Fe, Cr, Ni) and shape memory alloys (Ni, Ti).

1.2.5.1 Steel

Stainless steel, for example, would be a cost-effective replacement for graphite in bipolar plates for fuel cells. In comparison to graphite, steel is mechanically more stable, increasing the lifetime and durability of the cells and therefore making them commercially viable for automotive transport vehicles.[107–109] Furthermore, stainless steel can be more easily manufactured and machined to thin plates, potentially reducing the weight, form factor and price of bipolar plates. Graphite, on the other hand, is chemically inert and has superior stability in the harsh chemical environment of a fuel cell. The challenge, therefore, is to protect the mechanically superior and cheaper to manufacture steel from the corrosive environment without impeding current collection, by preventing the formation of an protective oxide layer that is electrically insulating.[107–109] Graphene is uniquely suited for this application as it is ultrathin, conductive and mechanically stable while being a chemically inert barrier to corrosive species.[5–7] So far, however, large-scale high-quality monolayer graphene films grown directly on stainless steel are still a challenge[33,47,110–115] and for the most part yield either inhomogeneous multilayer or non-continuous monolayer coatings. Even on comparatively less complex, low-alloyed steels CVD graphene films on par with graphene grown on copper substrates have not been achieved.[90,116]

As previously discussed, the controlled growth of graphene on multi-element metallurgical substrates requires the application of CVD conditions that have been specifically designed to account for the catalytic activity, microstructure, and interaction between carbon and the substrate (e.g. diffusion). This is particularly true for iron-based substrates, which exhibit highly variable carbon solubility between their crystallographic phases and for which carbon has a significant influence their structural transitions, making it is essential to implement precise adjustments to the CVD growth parameters, including the precursor flux and cooling rate, in order to achieve high-quality graphene

growth.[70,110] The presence of oxygen in general negatively affects graphene growth[117,118] and the homogeneous growth of graphene on stainless steel is further complicated by the tendency of the most commonly present elements chromium and manganese to readily form surface oxides with residual oxygen often still present under scalable conditions.[110] These oxides are catalytically non-ideal for carbon CVD and in general hinder ordered surface carbon growth.[106]

1.2.5.2 Nitinol (NiTi) shape memory alloy

NiTi shape memory alloys (also called Nitinol) are roughly equimolar alloys consisting of nickel (Ni) and titanium (Ti) with extraordinary properties incl. a shape memory effect (SME) and superelasticity.[119,120] The SME observed in NiTi alloys involves a reversible phase transition between a low-temperature martensitic phase and a higher-temperature austenitic phase. During fabrication, while in its higher-temperature austenite phase, NiTi can be manipulated into a desired shape, which it effectively 'memorises'. Upon cooling to lower temperature the NiTi undergoes a phase transition to a martensite phase. In this state, the material can undergo deformation while retaining its ability to revert to the memorised shape upon reheating. This reversible cycling between martensitic and austenitic phases enables the SME, rendering deformation in the martensitic phase reversible. The transition temperature between the martensitic and austenitic phases can be tailored through precise control of the Ni:Ti composition and specific material treatments, typically spanning from room temperature to approximately 100 °C.[121]

Nickel titanium (NiTi) shape memory alloys are used extensively for biomedical applications, for example as the main component of self-expandable cardiovascular stents.[83,119] In general, metal implants can suffer from lack of cell adhesion, proliferation, thrombosis and metal leaching after sustained contact with flowing blood inside the body. This can lead to strong immune responses that can interfere with the device's functionality and even damage the implant.[83–85] It is, therefore, necessary to control and limit the interaction of the implant with the surrounding biological environment and improve bio-compatibility of the metal device. This can be achieved by coating the metal with a protective layer that should ideally be chemically inert, smooth, bio-compatible and have high adhesion strength.[119]

As outlined above, graphene combines biocompatibility with chemical inertness, barrier capability, conductivity and reasonable mechanical properties. For these reasons, graphene coatings on NiTi substrates have been investigated in the past. The approaches

that have been studied to date, include wet-chemistry deposited films consisting of exfoliated graphene building blocks,[82] graphene CVD-grown on sacrificial high-purity Cu substrates with subsequent mechanical transfer to NiTi[83,84] and first attempts of direct graphene CVD on NiTi.[85,86]

CVD graphene grown on sacrificial (well calibrated) Cu and transferred to a NiTi shape memory alloy has been shown to provide good corrosion protection and inhibit toxic N^{2+}-ion release.[83,84] For better substrate interaction and adhesion, the direct growth of graphene on NiTi would be preferred. So far only so called "worm like" graphene has been grown directly on NiTi at 1050 °C, with variations in layer number and overall homogeneity, shown in figure 1.5.[85] Nevertheless this coating has been shown to already enhance biological activity compared to the bare metal substrate. The work by Li et al.[85] also elucidates the growth mechanism of graphene on NiTi by elemental depth-profiling XPS. They reported a native oxide layer on the substrate and that rutile TiO_2 was persistent under their conditions up to 950 °C. At temperatures above 1000 °C, no oxide was detected, and instead, the substrate subsurface was found to be Ni-deprived, and a prominent TiC phase was measured, which they (Li et al.[85]) identified as the active phase for graphene growth. Indicating its role in surface carbon growth in contrast to the Ni dissolution-segregation graphene growth mechanism on pure Ni substrates.[65] These prior findings highlight that changes to the metallurgical substrate (incl. the NiTi here) are commonplace at the elevated temperature graphene CVD conditions, as generally eluded to above.

In the appendix, an experimental investigation specifically into the challenges of the CVD of graphene on NiTi is presented.

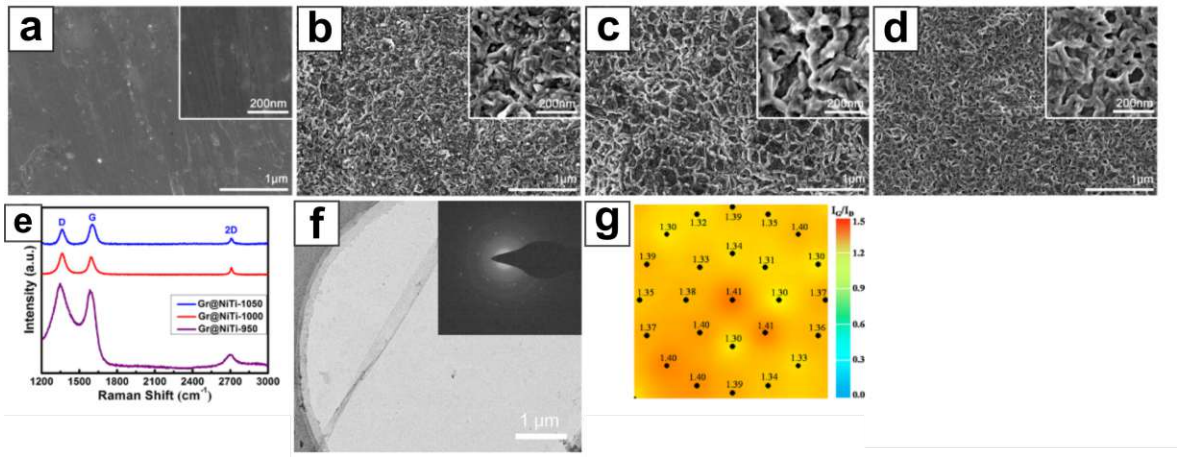

Figure 1.5: Figure illustrating state-of-the-art direct CVD graphene growth on NiTi shape memory alloy. Scanning electron microscopy (SEM) micrographs of surface morphology for (a) NiTi reference and graphene samples prepared at (b) 950 °C (c) 1000 °C and (d) 1050 °C showing "wormlike" surface structure. (e) Raman spectra of graphene samples with different growth temperatures. (f) Transmission electron microscopy (TEM) micrograph of free-standing graphene film transferred from 1050 °C sample with SAED pattern as inset, showing graphene diffraction spots. (g) Raman mapping of the complete sample surface, showing I_G/I_D for 1050 °C sample.(Adapted from Li et al.[85])

1.3 Publication notice

Parts of the introduction, in particular section 1.2.5 and 1.2.5.2 are part of publication number 3 in the publication list.

Bibliography

1. Rashid, T., Khawaja, H. A. & Edvardsen, K. Review of marine icing and anti-/de-icing systems. *Journal of Marine Engineering and Technology* **15,** 79–87. ISSN: 20568487. doi:10.1080/20464177.2016.1216734 (2016).
2. Ma, I. A. W., Ammar, S., Kumar, S. S. A., Ramesh, K. & Ramesh, S. A concise review on corrosion inhibitors: types, mechanisms and electrochemical evaluation studies. *Journal of Coatings Technology and Research* **19,** 241–268. ISSN: 1935-3804. doi:10.1007/s11998-021-00547-0 (2022).
3. *Corrosion Processes: Sensing, Monitoring, Data Analytics, Prevention/Protection, Diagnosis/Prognosis and Maintenance Strategies* (eds Vachtsevanos, G., Natarajan, K. A., Rajamani, R. & Sandborn, P.) (Springer International Publishing, Cham, 2020). ISBN: 978-3-030-32830-6. doi:10.1007/978-3-030-32831-3.
4. Novoselov, K. S. *et al.* Electric Field Effect in Atomically Thin Carbon Films. *Science* **306,** 666 LP –669. doi:10.1126/science.1102896 (2004).
5. Lee, C., Wei, X., Kysar, J. W. & Hone, J. Measurement of the Elastic Properties and Intrinsic Strength of Monolayer Graphene. *Science* **321.** Publisher: American Association for the Advancement of Science, 385–388. doi:10.1126/science.1157996 (2008).
6. Bunch, J. S. *et al.* Impermeable atomic membranes from graphene sheets. *Nano Letters* **8,** 2458–2462. ISSN: 15306984. doi:10.1021/nl801457b (2008).
7. Sun, P. Z. *et al.* Limits on gas impermeability of graphene. *Nature* **579,** 229–232. ISSN: 0028-0836. doi:10.1038/s41586-020-2070-x (2020).
8. Lemme, M. C., Akinwande, D., Huyghebaert, C. & Stampfer, C. 2D materials for future heterogeneous electronics. *Nature Communications* **13.** Number: 1 Publisher: Nature Publishing Group, 1392. ISSN: 2041-1723. doi:10.1038/s41467-022-29001-4 (2022).
9. Robertson, J. Amorphous carbon. *Advances in Physics* **35,** 317–374. ISSN: 0001-8732. doi:10.1080/00018738600101911 (1986).
10. Apaydin, D. H., Bayer, B. C., Arnault, J.-C. & Eder, D. in *Volume 3 From Magnetic to Bioactive Materials* 287–305 (De Gruyter, 2022). ISBN: 978-3-11-073347-1. doi:10.1515/9783110733471-018.

11. Geim, A. K. & Novoselov, K. S. The rise of graphene. *Nature Materials* **6.** Number: 3 Publisher: Nature Publishing Group, 183–191. ISSN: 1476-4660. doi:10.1038/nmat1849 (2007).
12. Robertson, J. Diamond-like amorphous carbon. *Materials Science and Engineering: R: Reports* **37,** 129–281. ISSN: 0927-796X. doi:10.1016/S0927-796X(02)00005-0 (2002).
13. Novoselov, K. S. *et al.* Two-dimensional gas of massless Dirac fermions in graphene. *Nature* **438.** Number: 7065 Publisher: Nature Publishing Group, 197–200. ISSN: 1476-4687. doi:10.1038/nature04233 (2005).
14. Novoselov, K. S. *et al.* Electronic properties of graphene. *physica status solidi (b)* **244.** _eprint: https://onlinelibrary.wiley.com/doi/pdf/10.1002/pssb.200776208, 4106–4111. ISSN: 1521-3951. doi:10.1002/pssb.200776208 (2007).
15. Meric, I. *et al.* Current saturation in zero-bandgap, top-gated graphene field-effect transistors. *Nature Nanotechnology* **3.** Publisher: Nature Publishing Group, 654–659. ISSN: 1748-3395. doi:10.1038/nnano.2008.268 (2008).
16. Balandin, A. A. *et al.* Superior Thermal Conductivity of Single-Layer Graphene. *Nano Letters* **8.** Publisher: American Chemical Society, 902–907. ISSN: 1530-6984. doi:10.1021/nl0731872 (2008).
17. Singh, V. *et al.* Graphene based materials: Past, present and future. *Progress in Materials Science* **56,** 1178–1271. ISSN: 0079-6425. doi:10.1016/j.pmatsci.2011.03.003 (2011).
18. Huang, Y. *et al.* Reliable Exfoliation of Large-Area High-Quality Flakes of Graphene and Other Two-Dimensional Materials. *ACS Nano* **9.** ISBN: 1936-0851, 10612–10620. ISSN: 1936086X. doi:10.1021/acsnano.5b04258. arXiv: cond-mat/0702595v1 (2015).
19. Li, H., Wu, J., Yin, Z. & Zhang, H. Preparation and Applications of Mechanically Exfoliated Single-Layer and Multilayer MoS2 and WSe2 Nanosheets. *Accounts of Chemical Research* **47.** Publisher: American Chemical Society, 1067–1075. ISSN: 0001-4842. doi:10.1021/ar4002312 (2014).
20. Novoselov, K. S. *et al.* A roadmap for graphene. *Nature* **490.** Publisher: Nature Publishing Group, 192–200. ISSN: 1476-4687. doi:10.1038/nature11458 (2012).
21. Li, Z. *et al.* Mechanisms of Liquid-Phase Exfoliation for the Production of Graphene. *ACS Nano* **14.** Publisher: American Chemical Society, 10976–10985. ISSN: 1936-0851. doi:10.1021/acsnano.0c03916 (2020).
22. Paton, K. R. *et al.* Scalable production of large quantities of defect-free few-layer graphene by shear exfoliation in liquids. *Nature Materials* **13.** Publisher: Nature Publishing Group, 624–630. ISSN: 1476-4660. doi:10.1038/nmat3944 (2014).
23. Shen, J. *et al.* Liquid Phase Exfoliation of Two-Dimensional Materials by Directly Probing and Matching Surface Tension Components. *Nano Letters* **15.** Publisher: American Chemical Society, 5449–5454. ISSN: 1530-6984. doi:10.1021/acs.nanolett.5b01842 (2015).
24. Shen, J. *et al.* Surface Tension Components Based Selection of Cosolvents for Efficient Liquid Phase Exfoliation of 2D Materials. *Small* **12.** _eprint: https://onlinelibrary.wiley.com/doi/pdf/10.1002/smll.201503834, 2741–2749. ISSN: 1613-6829. doi:10.1002/smll.201503834 (2016).

25. Rahmanian, E., Malekfar, R. & Pumera, M. Nanohybrids of Two-Dimensional Transition-Metal Dichalcogenides and Titanium Dioxide for Photocatalytic Applications. *Chemistry – A European Journal* **24,** 18–31. ISSN: 1521-3765. doi:10.1002/chem.201703434 (2018).

26. Singh, A. K., Mathew, K., Zhuang, H. L. & Hennig, R. G. Computational Screening of 2D Materials for Photocatalysis. *The Journal of Physical Chemistry Letters* **6,** 1087–1098. ISSN: 1948-7185, 1948-7185. doi:10.1021/jz502646d (2015).

27. Jaakkola, K. *et al.* Screen-printed and spray coated graphene-based RFID transponders. *2D Materials* **7.** Publisher: IOP Publishing, 015019. ISSN: 2053-1583. doi:10.1088/2053-1583/ab48d8 (2019).

28. Wang, J. *et al.* Ink-based 3D printing technologies for graphene-based materials: a review. *Advanced Composites and Hybrid Materials* **2,** 1–33. ISSN: 2522-0136. doi:10.1007/s42114-018-0067-9 (2019).

29. Shen, P.-C. *et al.* CVD Technology for 2-D Materials. *IEEE Transactions on Electron Devices* **65.** Conference Name: IEEE Transactions on Electron Devices, 4040–4052. ISSN: 1557-9646. doi:10.1109/TED.2018.2866390 (2018).

30. Xu, X. *et al.* Ultrafast epitaxial growth of metre-sized single-crystal graphene on industrial Cu foil. *Science Bulletin* **62,** 1074–1080. ISSN: 2095-9273. doi:10.1016/j.scib.2017.07.005 (2017).

31. Hu, Z. *et al.* Doping of Graphene Films: Open the way to Applications in Electronics and Optoelectronics. *Advanced Functional Materials* **32.** _eprint: https://onlinelibrary.wiley.com/doi/pdf/10.1002/adfm.202203179, 2203179. ISSN: 1616-3028. doi:10.1002/adfm.202203179 (2022).

32. Robinson, J. T. *et al.* Properties of Fluorinated Graphene Films. *Nano Letters* **10,** 3001–3005. ISSN: 1530-6984, 1530-6992. doi:10.1021/nl101437p (2010).

33. Ruammaitree, A., Phokharatkul, D., Nuntawong, N. & Wisitsoraat, A. Improvement in corrosion resistance of stainless steel foil by graphene coating using thermal chemical vapor deposition. *Surface Review and Letters* **25.** Publisher: World Scientific Publishing Co., 1840003. ISSN: 0218-625X. doi:10.1142/S0218625X18400036 (Supp01 2018).

34. Leenaerts, O., Partoens, B. & Peeters, F. M. Graphene: A perfect nanoballoon. *Applied Physics Letters* **93,** 193107. ISSN: 0003-6951. doi:10.1063/1.3021413 (2008).

35. Rodriguez, A., Schlichting, K.-P., Poulikakos, D. & Hu, M. Ab Initio Energetic Barriers of Gas Permeation across Nanoporous Graphene. *ACS Applied Materials & Interfaces* **13.** Publisher: American Chemical Society, 39701–39710. ISSN: 1944-8244. doi:10.1021/acsami.1c09229 (2021).

36. Zhao, Y. *et al.* Mass Transport Mechanism of Cu Species at the Metal/Dielectric Interfaces with a Graphene Barrier. *ACS Nano* **8.** Publisher: American Chemical Society, 12601–12611. ISSN: 1936-0851. doi:10.1021/nn5054987 (2014).

37. Singh Raman, R. K. & Tiwari, A. Graphene: The Thinnest Known Coating for Corrosion Protection. *JOM* **66,** 637–642. ISSN: 1543-1851. doi:10.1007/s11837-014-0921-3 (2014).

38. Prasai, D., Tuberquia, J. C., Harl, R. R., Jennings, G. K. & Bolotin, K. I. Graphene: Corrosion-Inhibiting Coating. *ACS Nano* **6,** 1102–1108. ISSN: 1936-0851, 1936-086X. doi:10.1021/nn203507y (2012).

39. Böhm, S. Graphene against corrosion. *Nature Nanotechnology* **9.** Publisher: Nature Publishing Group, 741–742. ISSN: 17483395. doi:10.1038/nnano.2014.220 (2014).

40. Halkjær, S. *et al.* Low-temperature synthesis of a graphene-based, corrosion-inhibiting coating on an industrial grade alloy. *Corrosion Science* **152,** 1–9. ISSN: 0010-938X. doi:10.1016/j.corsci.2019.01.029 (2019).

41. Schriver, M. *et al.* Graphene as a long-term metal oxidation barrier: Worse than nothing. *ACS Nano* **7,** 5763–5768. ISSN: 19360851. doi:10.1021/nn4014356 (2013).

42. Zhou, F., Li, Z., Shenoy, G. J., Li, L. & Liu, H. Enhanced Room-Temperature Corrosion of Copper in the Presence of Graphene. *ACS Nano* **7,** 6939–6947. ISSN: 1936-0851, 1936-086X. doi:10.1021/nn402150t (2013).

43. Dennis, R. V., Fleer, N. A., Davidson, R. D. & Banerjee, S. in *Graphene Technology: From Laboratory to Fabrication* (eds Nazarpour, S. & Waite, S. R.) 155–176 (Wiley-VCH Verlag GmbH & Co. KGaA, Weinheim, Germany, 2016). ISBN: 978-3-527-33833-7. doi:10.1002/9783527687541.ch6.

44. Kirkland, N. T., Schiller, T., Medhekar, N. & Birbilis, N. Exploring graphene as a corrosion protection barrier. *Corrosion Science* **56,** 1–4. ISSN: 0010-938X. doi:10.1016/j.corsci.2011.12.003 (2012).

45. Cui, Y., Kundalwal, S. & Kumar, S. Gas barrier performance of graphene/polymer nanocomposites. *Carbon* **98,** 313–333. ISSN: 00086223. doi:10.1016/j.carbon.2015.11.018 (2016).

46. Paul, D. R. & Robeson, L. M. Polymer nanotechnology: Nanocomposites. *Polymer* **49,** 3187–3204. ISSN: 0032-3861. doi:10.1016/j.polymer.2008.04.017 (2008).

47. Camilli, L., Yu, F., Cassidy, A., Hornekær, L. & Bøggild, P. Challenges for continuous graphene as a corrosion barrier. *2D Materials* **6.** ISSN: 20531583. doi:10.1088/2053-1583/ab04d4 (2019).

48. Ohring, M. *Materials Science of Thin Films: Depositon and Structure* 2nd edition. 816 pp. ISBN: 978-0-12-524975-1 (Academic Press, San Diego, CA, 2001).

49. in. *Chemical Vapour Deposition: An Integrated Engineering Design for Advanced Materials* (eds Xu, Y. & Yan, X.-T.) 1–28 (Springer, London, 2010). ISBN: 978-1-84882-894-0. doi:10.1007/978-1-84882-894-0_1.

50. Vlassiouk, I. *et al.* Role of Hydrogen in Chemical Vapor Deposition Growth of Large Single-Crystal Graphene. *ACS Nano* **5.** Publisher: American Chemical Society, 6069–6076. ISSN: 1936-0851. doi:10.1021/nn201978y (2011).

51. Tang, L., Tan, J., Nong, H., Liu, B. & Cheng, H.-M. Chemical Vapor Deposition Growth of Two-Dimensional Compound Materials: Controllability, Material Quality, and Growth Mechanism. *Accounts of Materials Research* **2.** Publisher: American Chemical Society, 36–47. doi:10.1021/accountsmr.0c00063 (2021).

52. Cassell, A. M., Raymakers, J. A., Kong, J. & Dai, H. Large Scale CVD Synthesis of Single-Walled Carbon Nanotubes. *The Journal of Physical Chemistry B* **103.** Publisher: American Chemical Society, 6484–6492. ISSN: 1520-6106. doi:10.1021/jp990957s (1999).

53. Faktor, M. M., Garrett, I. & Cullen, G. W. Growth of Crystals from the Vapour. *Physics Today* **28,** 52–54. ISSN: 0031-9228. doi:10.1063/1.3069245 (1975).

54. Spear, K. E. Principles and applications of chemical vapor deposition (CVD). *Pure and Applied Chemistry* **54.** Publisher: De Gruyter, 1297–1311. ISSN: 1365-3075. doi:10.1351/pac198254071297 (1982).

55. Caneva, S. *et al.* Controlling Catalyst Bulk Reservoir Effects for Monolayer Hexagonal Boron Nitride CVD. *Nano Letters* **16,** 1250–1261. ISSN: 1530-6984. doi:10.1021/acs.nanolett.5b04586 (2016).

56. Cabrero-Vilatela, A., Weatherup, R. S., Braeuninger-Weimer, P., Caneva, S. & Hofmann, S. Towards a general growth model for graphene CVD on transition metal catalysts. *Nanoscale* **8.** Publisher: The Royal Society of Chemistry, 2149–2158. ISSN: 2040-3372. doi:10.1039/C5NR06873H (2016).

57. Choi, S. H. *et al.* Large-scale synthesis of graphene and other 2D materials towards industrialization. *Nature Communications* **13.** Publisher: Nature Publishing Group, 1484. ISSN: 2041-1723. doi:10.1038/s41467-022-29182-y (2022).

58. Weatherup, R. S. *et al.* In situ characterization of alloy catalysts for Low-temperature graphene growth. *Nano Letters* **11,** 4154–4160. ISSN: 15306984. doi:10.1021/nl202036y (2011).

59. Weatherup, R. S., Dlubak, B. & Hofmann, S. Kinetic control of catalytic CVD for high-quality graphene at low temperatures. *ACS Nano* **6,** 9996–10003. ISSN: 19360851. doi:10.1021/nn303674g (2012).

60. Weatherup, R. S. *et al.* On the Mechanisms of Ni-Catalysed Graphene Chemical Vapour Deposition. *ChemPhysChem* **13,** 2544–2549. ISSN: 1439-7641. doi:10.1002/cphc.201101020 (2012).

61. Kidambi, P. R. *et al.* Observing graphene grow: Catalyst-graphene interactions during scalable graphene growth on polycrystalline copper. *Nano Letters* **13,** 4769–4778. ISSN: 15306984. doi:10.1021/nl4023572 (2013).

62. Mattevi, C., Kim, H. & Chhowalla, M. A review of chemical vapour deposition of graphene on copper. *J. Mater. Chem.* **21,** 3324–3334. ISSN: 0959-9428, 1364-5501. doi:10.1039/C0JM02126A (2011).

63. Deng, B. *et al.* Wrinkle-Free Single-Crystal Graphene Wafer Grown on Strain-Engineered Substrates. *ACS Nano* **11.** Publisher: American Chemical Society, 12337–12345. ISSN: 1936-0851. doi:10.1021/acsnano.7b06196 (2017).

64. Deng, B. *et al.* Scalable and ultrafast epitaxial growth of single-crystal graphene wafers for electrically tunable liquid-crystal microlens arrays. *Science Bulletin* **64.** Publisher: Elsevier B.V., 659–668. ISSN: 20959281. doi:10.1016/j.scib.2019.04.030 (2019).

65. Gong, Y. *et al.* Layer-Controlled and Wafer-Scale Synthesis of Uniform and High-Quality Graphene Films on a Polycrystalline Nickel Catalyst. *Advanced Functional Materials* **22,** 3153–3159. ISSN: 1616-3028. doi:10.1002/adfm.201200388 (2012).

66. Huang, L. *et al.* Synthesis of high-quality graphene films on nickel foils by rapid thermal chemical vapor deposition. *Carbon* **50,** 551–556. ISSN: 0008-6223. doi:10.1016/j.carbon.2011.09.012 (2012).

67. Xue, Y. *et al.* Synthesis of large-area, few-layer graphene on iron foil by chemical vapor deposition. *Nano Research* **4,** 1208–1214. ISSN: 19980000. doi:10.1007/s12274-011-0171-4 (2011).

68. Wu, Y., Wang, S. & Komvopoulos, K. A review of graphene synthesis by indirect and direct deposition methods. *Journal of Materials Research* **35,** 76–89. ISSN: 0884-2914, 2044-5326. doi:10.1557/jmr.2019.377 (2020).

69. Derbyshire, F., Presland, A. & Trimm, D. Graphite formation by the dissolution—precipitation of carbon in cobalt, nickel and iron. *Carbon* **13,** 111–113. ISSN: 00086223. doi:10.1016/0008-6223(75)90267-5 (1975).

70. You, Y. *et al.* A Controlled Carburization Process to Obtain Graphene–Fe3C–Fe Composites. *Advanced Materials Interfaces* **5,** 1–7. ISSN: 21967350. doi:10.1002/admi.201800599 (2018).

71. Park, E., Ostrovski, O., Zhang, J., Thomson, S. & Howe, R. Characterization of phases formed in the iron carbide process by X-ray diffraction, mossbauer, X-ray photoelectron spectroscopy, and raman spectroscopy analyses. *Metallurgical and Materials Transactions B* **32,** 839–845. ISSN: 1543-1916. doi:10.1007/s11663-001-0071-1 (2001).

72. Vinogradov, N. A. *et al.* Formation and structure of graphene waves on Fe(110). *Physical Review Letters* **109,** 1–5. ISSN: 00319007. doi:10.1103/PhysRevLett.109.026101 (2012).

73. An, H., Lee, W. J. & Jung, J. Graphene synthesis on Fe foil using thermal CVD. *Current Applied Physics* **11.** Publisher: Elsevier B.V, S81–S85. ISSN: 15671739. doi:10.1016/j.cap.2011.03.077 (2011).

74. Tripathi, K., Gyawali, G. & Lee, S. W. Graphene Coating via Chemical Vapor Deposition for Improving Friction and Wear of Gray Cast Iron at Interfaces. *ACS Applied Materials and Interfaces* **9,** 32336–32351. ISSN: 19448252. doi:10.1021/acsami.7b07922 (2017).

75. Lavin-Lopez, M. P., Fernandez-Diaz, M., Sanchez-Silva, L., Valverde, J. L. & Romero, A. Improving the growth of monolayer CVD-graphene over polycrystalline iron sheets. *New Journal of Chemistry* **41.** Publisher: Royal Society of Chemistry, 5066–5074. ISSN: 13699261. doi:10.1039/c7nj00281e (2017).

76. Khan, S. *et al.* Low-Temperature Synthesis of Graphene and Fabrication of Top-Gated Field Effect Transistors without Using Transfer Processes. doi:10.1143/APEX.3.025102 (2010).

77. Kondo, D. *et al.* Selective synthesis of carbon nanotubes and multi-layer graphene by controlling catalyst thickness. *Chemical Physics Letters* **514,** 294–300. ISSN: 0009-2614. doi:10.1016/j.cplett.2011.08.042 (2011).

78. Liu, N. *et al.* Universal Segregation Growth Approach to Wafer-Size Graphene from Non-Noble Metals. *Nano Letters* **11.** Publisher: American Chemical Society, 297–303. ISSN: 1530-6984. doi:10.1021/nl103962a (2011).

79. Anguita, J. V., Pozegic, T. R., Ahmad, M. & Silva, S. R. P. Layer-by-Layer Growth of Graphene Sheets over Selected Areas for Semiconductor Device Applications. *ACS Applied Nano Materials* **4,** 5211–5219. ISSN: 25740970. doi:10.1021/acsanm.1c00620 (2021).

80. Ferrari, A. C. *et al.* Science and technology roadmap for graphene, related two-dimensional crystals, and hybrid systems. *Nanoscale* **7.** Publisher: The Royal Society of Chemistry, 4598–4810. ISSN: 2040-3372. doi:10.1039/C4NR01600A (2015).

81. Cui, G. *et al.* A comprehensive review on graphene-based anti-corrosive coatings. *Chemical Engineering Journal* **373.** Publisher: Elsevier, 104–121. ISSN: 13858947. doi:10.1016/j.cej.2019.05.034 (2019).

82. Zhang, K. *et al.* Electrophoretic deposition of graphene oxide on NiTi alloy for corrosion prevention. *Vacuum* **161,** 276–282. ISSN: 0042-207X. doi:10.1016/j.vacuum.2018.12.032 (2019).

83. Podila, R., Moore, T., Alexis, F. & Rao, A. M. Graphene coatings for enhanced hemo-compatibility of nitinol stents. *RSC Advances* **3,** 1660–1665. ISSN: 20462069. doi:10.1039/c2ra23073a (2013).

84. Zhang, L. *et al.* Graphene enhanced anti-corrosion and biocompatibility of NiTi alloy. *NanoImpact* **7,** 7–14. ISSN: 2452-0748. doi:10.1016/j.impact.2016.10.003 (2017).

85. Li, J. *et al.* CVD growth of graphene on NiTi alloy for enhanced biological activity. *ACS Applied Materials and Interfaces* **7,** 19876–19881. ISSN: 19448252. doi:10.1021/acsami.5b06639 (2015).

86. Zou, J., Wang, X., Zhang, P. & Du, X. Ultrafast flame coating of carbon and chemical vapor deposition of graphene on NiTi alloy to enhance its corrosion resistance. *Diamond and Related Materials* **128,** 109231. ISSN: 0925-9635. doi:10.1016/j.diamond.2022.109231 (2022).

87. Berman, D., Erdemir, A. & Sumant, A. V. Few layer graphene to reduce wear and friction on sliding steel surfaces. *Carbon* **54,** 454–459. ISSN: 0008-6223. doi:10.1016/j.carbon.2012.11.061 (2013).

88. Berman, D., Erdemir, A. & Sumant, A. V. Approaches for Achieving Superlubricity in Two-Dimensional Materials. *ACS Nano* **12.** Publisher: American Chemical Society, 2122–2137. ISSN: 1936-0851. doi:10.1021/acsnano.7b09046 (2018).

89. Dumée, L. F. *et al.* Growth of nano-textured graphene coatings across highly porous stainless steel supports towards corrosion resistant coatings. *Carbon* **87,** 395–408. ISSN: 00086223. doi:10.1016/j.carbon.2015.02.042 (C 2015).

90. Zhu, M. *et al.* Low-Temperature in Situ Growth of Graphene on Metallic Substrates and Its Application in Anticorrosion. *ACS Applied Materials & Interfaces* **8,** 502–510. ISSN: 1944-8244. doi:10.1021/acsami.5b09453 (2016).

91. Nazarova, M. *et al.* Growth of graphene on tantalum and its protective properties. *Carbon* **139.** Publisher: Elsevier Ltd, 29–34. ISSN: 00086223. doi:10.1016/j.carbon.2018.06.027 (2018).

92. Chang, C.-H. *et al.* Novel anticorrosion coatings prepared from polyaniline/graphene composites. *Carbon* **50,** 5044–5051. ISSN: 0008-6223. doi:10.1016/j.carbon.2012.06.043 (2012).

93. Aneja, K. S., Bohm, S., Khanna, A. S. & Bohm, H. L. M. Graphene based anticorrosive coatings for Cr(VI) replacement. *Nanoscale* **7.** Publisher: The Royal Society of Chemistry, 17879–17888. ISSN: 2040-3372. doi:10.1039/C5NR04702A (2015).

94. Tong, Y., Bohm, S. & Song, M. The capability of graphene on improving the electrical conductivity and anti-corrosion properties of Polyurethane coatings. *Applied Surface Science. 7th International Conference on Advanced Nanomaterials, 2nd International Conference on Graphene Technology, 1st International Conference on Spintronics Materials* **424,** 72–81. ISSN: 0169-4332. doi:10.1016/j.apsusc.2017.02.081 (2017).

95. Krishnan, M. A. *et al.* Graphene-based anticorrosive coatings for copper. *RSC Advances* **8.** Publisher: The Royal Society of Chemistry, 499–507. ISSN: 2046-2069. doi:10.1039/C7RA10167H (2017).

96. Raine, T. P. *et al.* Graphene/Polyamide Laminates for Supercritical CO2 and H2S Barrier Applications: An Approach toward Permeation Shutdown. *Advanced Materials Interfaces* **5,** 1800304. ISSN: 2196-7350. doi:10.1002/admi.201800304 (2018).

97. Yu, F. *et al.* Complete long-term corrosion protection with chemical vapor deposited graphene. *Carbon* **132,** 78–84. ISSN: 0008-6223. doi:10.1016/j.carbon.2018.02.035 (2018).

98. Singhbabu, Y. N., Sivakumar, B., Choudhary, S. K., Das, S. & Sahu, R. K. Corrosion-protective reduced graphene oxide coated cold rolled steel prepared using industrial setup: A study of protocol feasibility for commercial production. *Surface and Coatings Technology* **349,** 119–132. ISSN: 0257-8972. doi:10.1016/j.surfcoat.2018.05.046 (2018).

99. Dearnley, P. A. *Introduction to Surface Engineering* ISBN: 978-0-521-40168-5. doi:10.1017/9781139031509 (Cambridge University Press, Cambridge, 2017).

100. Kidambi, P. R. *et al.* In situ observations during chemical vapor deposition of hexagonal boron nitride on polycrystalline copper. *Chemistry of Materials* **26,** 6380–6392. ISSN: 15205002. doi:10.1021/cm502603n (2014).

101. Bayer, B. C. *et al.* Introducing Overlapping Grain Boundaries in Chemical Vapor Deposited Hexagonal Boron Nitride Monolayer Films. *ACS Nano* **11,** 4521–4527. ISSN: 1936086X. doi:10.1021/acsnano.6b08315 (2017).

102. Bayer, B. C. *et al.* In Situ Observations of Phase Transitions in Metastable Nickel (Carbide)/Carbon Nanocomposites. *Journal of Physical Chemistry C* **120,** 22571–22584. ISSN: 19327455. doi:10.1021/acs.jpcc.6b01555 (2016).

103. Caneva, S. *et al.* Nucleation control for large, single crystalline domains of monolayer hexagonal boron nitride via Si-doped Fe catalysts. *Nano Letters* **15,** 1867–1875. ISSN: 15306992. doi:10.1021/nl5046632 (2015).

104. Lin, L., Deng, B., Sun, J., Peng, H. & Liu, Z. Bridging the Gap between Reality and Ideal in Chemical Vapor Deposition Growth of Graphene. *Chemical Reviews* **118,** 9281–9343. ISSN: 15206890. doi:10.1021/acs.chemrev.8b00325 (2018).

105. Fan, X. *et al.* Chemical vapor deposition of graphene on refractory metals: The attempt of growth at much higher temperature. *Synthetic Metals* **247,** 233–239. ISSN: 0379-6779. doi:10.1016/j.synthmet.2018.12.016 (2019).

106. Kidambi, P. R. *et al.* Hafnia nanoparticles – a model system for graphene growth on a dielectric. *physica status solidi (RRL) – Rapid Research Letters* **5.** _eprint: https://onlinelibrary.wiley.com/doi/pdf/10.1002/pssr.201100155, 341–343. ISSN: 1862-6270. doi:10.1002/pssr.201100155 (2011).

107. Tawfik, H., Hung, Y. & Mahajan, D. Metal bipolar plates for PEM fuel cell—A review. *Journal of Power Sources* **163,** 755–767. ISSN: 03787753. doi:10.1016/j.jpowsour.2006.09.088 (2007).

108. Xu, Z., Qiu, D., Yi, P., Peng, L. & Lai, X. Towards mass applications: A review on the challenges and developments in metallic bipolar plates for PEMFC. *Progress in Natural Science: Materials International* **30,** 815–824. ISSN: 10020071. doi:10.1016/j.pnsc.2020.10.015 (2020).

109. Wu, S. *et al.* A review of modified metal bipolar plates for proton exchange membrane fuel cells. *International Journal of Hydrogen Energy* **46,** 8672–8701. ISSN: 0360-3199. doi:10.1016/j.ijhydene.2020.12.074 (2021).

110. John, R., Ashokreddy, A., Vijayan, C. & Pradeep, T. Single-and few-layer graphene growth on stainless steel substrates by direct thermal chemical vapor deposition. *Nanotechnology* **22.** ISSN: 09574484. doi:10.1088/0957-4484/22/16/165701 (2011).

111. Gullapalli, H., Mohana Reddy, A. L., Kilpatrick, S., Dubey, M. & Ajayan, P. M. Graphene growth via carburization of stainless steel and application in energy storage. *Small* **7,** 1697–1700. ISSN: 16136810. doi:10.1002/smll.201100111 (2011).

112. Pu, N. W. *et al.* Graphene grown on stainless steel as a high-performance and ecofriendly anti-corrosion coating for polymer electrolyte membrane fuel cell bipolar plates. *Journal of Power Sources* **282.** Publisher: Elsevier B.V, 248–256. ISSN: 03787753. doi:10.1016/j.jpowsour.2015.02.055 (2015).

113. Stoot, A. C., Camilli, L., Spiegelhauer, S.-A., Yu, F. & Bøggild, P. Multilayer graphene for long-term corrosion protection of stainless steel bipolar plates for polymer electrolyte membrane fuel cell. *Journal of Power Sources* **293,** 846–851. ISSN: 0378-7753. doi:10.1016/j.jpowsour.2015.06.009 (2015).

114. Chung, C.-Y. *et al.* Carbon film-coated 304 stainless steel as PEMFC bipolar plate. *Journal of Power Sources* **176,** 276–281. ISSN: 0378-7753. doi:10.1016/j.jpowsour.2007.10.022 (2008).

115. Yuan, G. D. *et al.* Graphene sheets via microwave chemical vapor deposition. *Chemical Physics Letters* **467,** 361–364. ISSN: 0009-2614. doi:10.1016/j.cplett.2008.11.059 (2009).

116. Qureshi, T. *et al.* Graphene-based anti-corrosive coating on steel for reinforced concrete infrastructure applications: Challenges and potential. *Construction and Building Materials* **351,** 128947. ISSN: 0950-0618. doi:10.1016/j.conbuildmat.2022.128947 (2022).

117. Burton, O. J. *et al.* The Role and Control of Residual Bulk Oxygen in the Catalytic Growth of 2D Materials. *The Journal of Physical Chemistry C* **123,** 16257–16267. ISSN: 1932-7447, 1932-7455. doi:10.1021/acs.jpcc.9b03808 (2019).

118. Amontree, J. *et al.* Reproducible graphene synthesis by oxygen-free chemical vapour deposition. *Nature.* Publisher: Nature Publishing Group, 1–7. ISSN: 1476-4687. doi:10.1038/s41586-024-07454-5 (2024).

119. Duerig, T., Pelton, A. & Stöckel, D. An overview of nitinol medical applications. *Materials Science and Engineering: A* **273-275,** 149–160. ISSN: 0921-5093. doi:10.1016/S0921-5093(99)00294-4 (1999).

120. Bayer, B. C., Khan, A. F., Mehmood, M. & Barber, Z. H. Effect of substrate on processing of multi-gun sputter deposited, near-stoichiometric Ni2MnGa thin films. *Thin Solid Films* **518,** 2659–2664. ISSN: 0040-6090. doi:10.1016/j.tsf.2009.08.030 (2010).

121. Sanjabi, S., Sadrnezhaad, S. K., Yates, K. A. & Barber, Z. H. Growth and characterization of TixNi1−x shape memory thin films using simultaneous sputter deposition from separate elemental targets. *Thin Solid Films* **491,** 190–196. ISSN: 0040-6090. doi:10.1016/j.tsf.2005.06.004 (2005).

CHAPTER 2

Experimental Methods

2.1 Substrates

CVD was done on metal substrates, namely 100 µm thick (Alfa Aesar Puratonic® 99.5 %) polycrystalline iron foil; 500 µm "low-carbon" steel (DN 1.0338, H+S Präzisionsfolien GmbH); 500 µm "high-carbon" steel (DN 1.0330, Fix Metall GmbH); 500 µm "high-alloy" stainless steel (DN 1.4404, H+S Präzisionsfolien GmbH); 127 µm thick NiTi (Alfa Aesar, Nitinol foil, 45514, flat annealed) foils and 25 µm copper foils (Alfa Aesar Puratonic® 99.999 %).

Detailed information on steel compositions is provided in the methods section in chapter 4.

2.2 Chemical Vapour Deposition

We employ a custom-built hot-wall CVD system consisting of a quartz-tube (GVB, EN08NB) in split-tube furnace (Carbolite Gero Split tube furnace - HZS 12/600) which can be pumped by a rotary vane pump (Vacuubrand RZ 2.5) and small turbo molecular pump (VARIAN, Turbo-V 70LP) combination to a base pressure of ~1×10^{-3} mbar. The setup allows for the turbomolecular pump to be completely bypassed, thereby running the system using only the rotary pump. Process gases argon (Ar) (Messer 5.0, 99.999 % purity), hydrogen (H_2) (Messer 2.1, 99.1 % purity) and methane (C_2H_4)

(Messer 2.5, 99.5 % purity) are fed via a manual flow-controllers, while process gases acetylene (C_2H_2) (Messer 2.6, 99.6 % purity) and a second source of hydrogen (H_2) (Messer 2.1, 99.1 % purity) can be fed via the modular gas control unit via electronic mass flow controllers (Bronkhorst EL-FLOW select). This modular unit can be easily separated from the main system in order to use it for other experimental setups, e.g. in-situ XRD. A technical sketch of the CVD system can be seen in figure 2.1 and an image of the laboratory setup can be seen in figure 2.2.

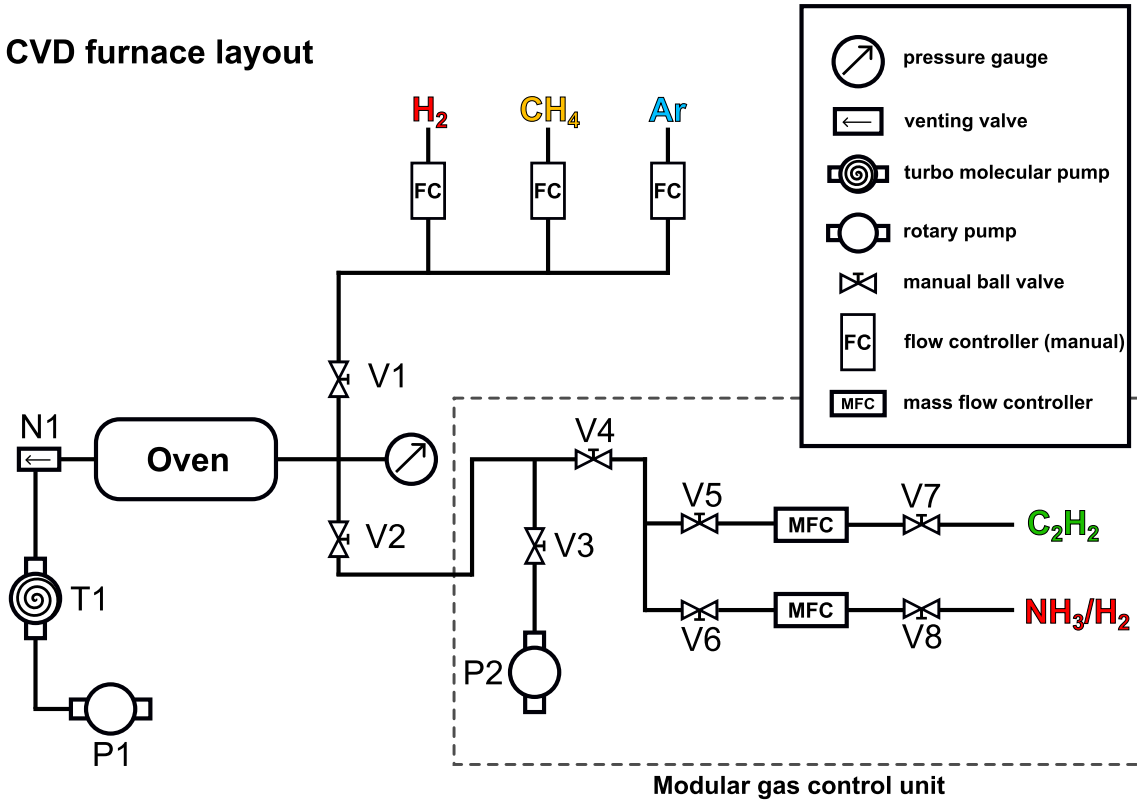

Figure 2.1: Technical schematic of CVD setup with gas and vacuum control overview. The reaction zone in the furnace can be fed with either H_2, CH_4 or Ar through manual flow meters which are connected via a ball valve (V1) to the furnace inlet, where the pressure gauge is attached. A secondary fully portable modular gas control unit is connected through the valve V2 and consists of two digital mass flow controllers for H_2 and C_2H_2 gas. Additionally the unit has a rotary pump (P2) for evacuating the gas lines separate from the main system. The main system possesses both a small turbomolecular pump (T1) and a rotary pre-vacuum pump (P1). The system can however be run by completely bypassing the turbomolecular pump as well.

In general, catalytic metal substrate foils are inserted into the quartz glass tube and positioned in the caenter of the oven hot zone. The tube is then evacuated either with the turbomolecular (VARIAN, Turbo-V 70LP) and rotary (Vacuubrand RZ 2.5) pump combination for the 100 µm thick polycrystalline iron foil, the 500 µm "low-carbon"

steel, the 500 µm "high-carbon" steel, the "high-alloy" stainless steel or the 127 µm thick NiTi foils, or solely by the rotary pump for the 25 µm copper foils. After evacuation, the system can be purged by Ar gas multiple times as needed. The substrates are heated in a reductive atmosphere, either pure H_2 or a H_2/Ar mixture, to temperatures between 500 °C and 970 °C. In general, an annealing step at elevated temperatures is employed prior to the carbon precursor exposure, with the objective of reducing surface oxides, decreasing the surface roughness and increasing the grain size of the substrate crystal domains. For copper substrates, a flow of ~100 sccm of precursor CH_4 gas was added to the Ar/H_2 mixture (2000 sccm/200 sccm) resulting in a pressure increase from 3.5 mbar background pressure to ~5.7 mbar during graphene growth. The typical growth time for graphene on copper was 30 min, after which the precursor flow was interrupted and the substrates were left to cool naturally in Ar/H_2 atmosphere after opening the split tube furnace. For metal substrates other than copper, including Fe/steels, the background atmosphere during the entire CVD process was 1 mbar of pure H_2 (~250 sccm), while 0.1 to 10 sccm of C_2H_2 was used as a precursor gas during growth. Growth times of 30 min were also standard for these metal substrates. Additional external cooling with a fan was employed for somewhat faster cooling.

More detailed CVD process parameters are described for the individual experiments in each chapter.

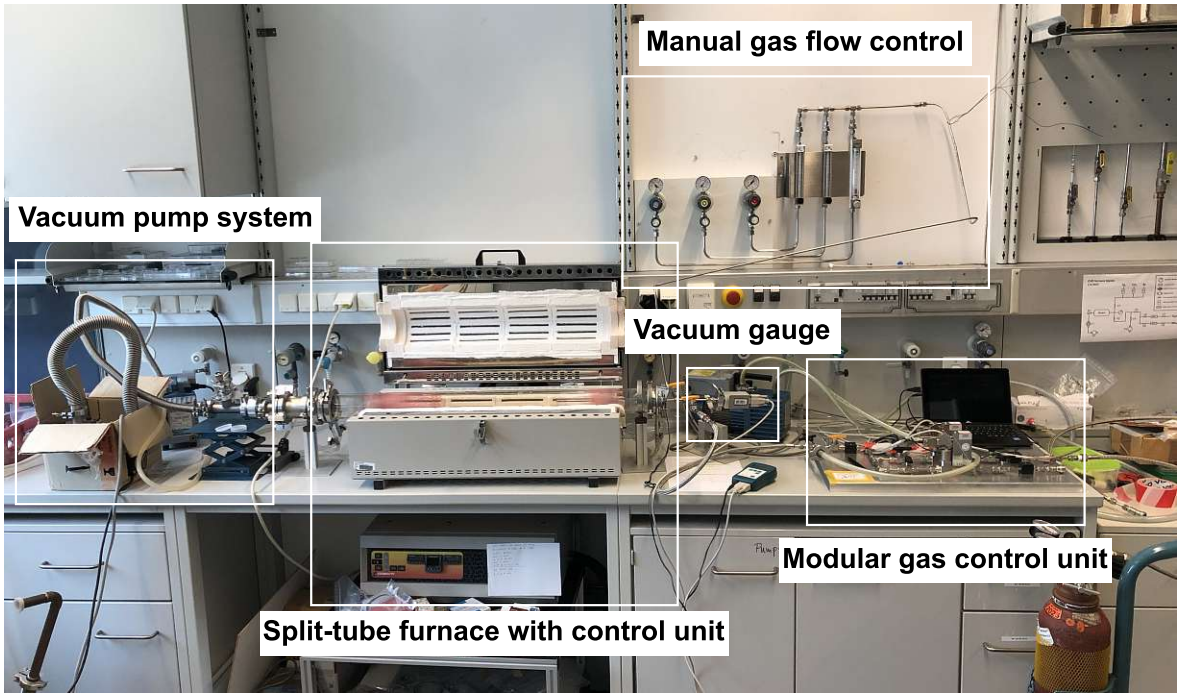

Figure 2.2: Image of the CVD lab setup used in this work. Important sections are indicated. A technical sketch of the system is shown in Figure 2.1

2.3 Raman Spectroscopy

Raman spectroscopy is a powerful material characterisation technique probing the molecular vibrational states of a material based on the principle of inelastic photon scattering. When a material is irradiated with monochromatic light from a laser, the majority of photons are scattered elastically via Rayleigh scattering. In this case, no energy is absorbed by the material, and the scattered photon has the same frequency as the incident light. A small fraction of the incoming photons can scatter inelastically, which is called Raman scattering. When this occurs the molecule (or crystal) relaxes to a different vibrational level after excitation by the photon and in the process emits a photon of different frequency than the incident light.[122] It is possible that the inelastically scattered photon can have a higher frequency than the incident light, called anti-Stokes scattering, and a lower frequency, called Stokes scattering. The probability for Stokes scattering is, however, much higher leading to the red-shifted signal, which decreased in frequency, having much higher intensity. These signals are the main source of information in most cases.[122] In Figure 2.3 a visualisation of vibrational energy transitions for Raman and Rayleigh scattering is shown.

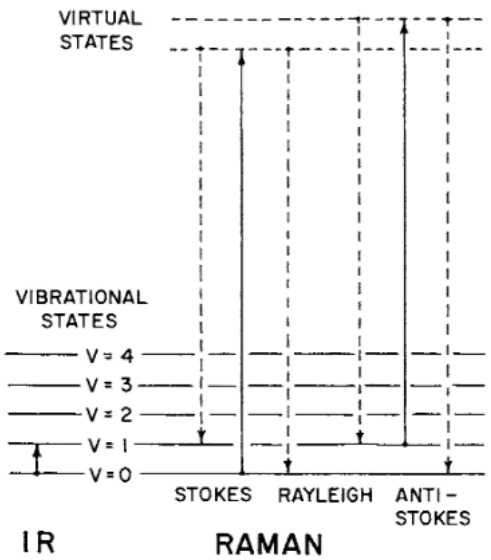

Figure 2.3: Sketch showing energy states involved in infrared and Raman spectroscopy. Adapted from *The Handbook of Infrared and Raman Characteristic Frequencies of Organic Molecules*[122]

It should be noted, that Raman spectroscopy and infrared (IR) spectroscopy, in which the sample is irradiated by a broad-band source of light in the infrared region, are related because they are both vibrational spectroscopy techniques using light excitation. In

general, a vibrational mode is considered IR-active if there is a change in the molecular dipole moment during the vibration. Conversely, a vibrational mode is Raman-active if there is a change in polarizability during the vibration. Qualitatively, antisymmetric vibrational modes and vibrations associated with polar groups are more likely to show significant IR absorption, whereas symmetric vibrational modes typically exhibit strong Raman signals.[122]

Raman spectroscopy is uniquely suited for the characterization of carbon materials, including graphene. It can distinguish between different carbon allotropes such as graphite, diamond, graphene, carbon nanotubes and amorphous carbon.[123] In particular, for graphene it can give precise information about layer number[124] (especially monolayer identification), defect density[125] and even doping levels,[126] making it a fast, reliable and non-destructive method for graphene characterization. In Figure 2.4, the Raman features labelled D, G and 2D, which are very significant for carbon material analysis, are shown. For graphene, in particular, the intensity ratio I_{2D}/I_G can indicate layer number (monolayer confirmation) and the D peak, associated with the defect density, is a measure of the structural quality of the graphene.

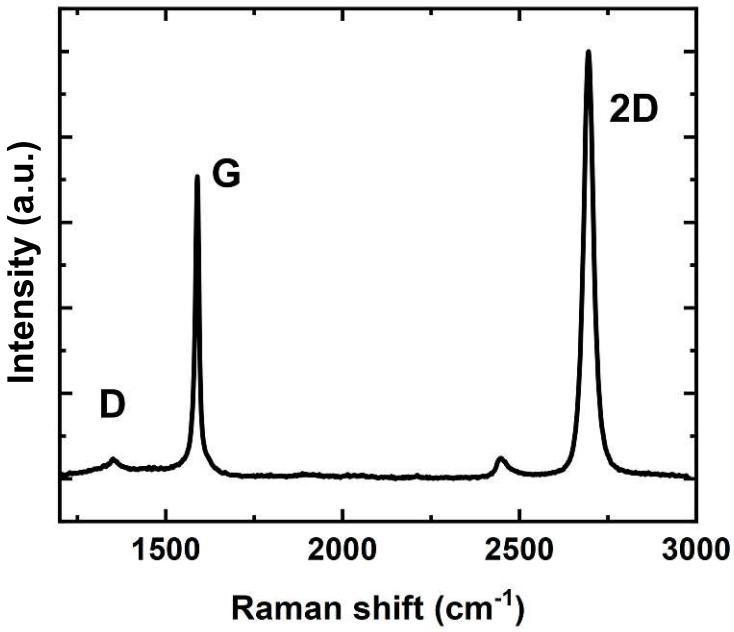

Figure 2.4: Raman spectrum of graphene transferred onto Si wafer substrate. Characteristic D (~1350 cm^{-1}), G (~1580 cm^{-1}) and 2D (~2700 cm^{-1}) peaks used for carbon material, in paricular graphene, analysis.

If not otherwise stated, all Raman spectroscopy shown in this work was measured using a WITec alpha 300 RSA+ correlative microscope with a laser wavelength of 532 nm as

standard and 488 nm for copper samples. Laser power used was either 5 mW or 10 mW depending on sample stability. Objective lenses used were a 20x and a 100x lens for imaging and scattered light collection. In general Raman spectra were collected with the 100x objective and an integration time of 1 s and 20 accumulations resulting in a good signal to noise ratio.

2.4 X-ray Diffraction (XRD)

X-ray diffraction can provide detailed information on the crystallographic state of a material, including crystallinity, crystallite size, texture and strain. It uses X-ray radiation to irradiate the sample and measures the angles and intensities of the diffracted beam. In this work it is used to provide crystallographic information and phase identification of our growth substrates. Using the in-situ capabilities of our measurement setup we can track substrate phase changes during CVD graphene growth under process conditions.

Ex-situ XRD measurements were conducted with a PANalytical X´Pert Pro multi-purpose diffractometer (MPD), with a standard rotating stage and chromium (Cr) anode as X-ray source with a wavelength of 2.26 Å. Presented Cr anode ex-situ XRD patterns were recalculated and scaled to match the in-situ XRD Cu anode datasets for comparison (see following).

In-situ XRD patterns were recorded on a PANalytical X´Pert Pro multi-purpose diffractometer (MPD) in Bragg Brentano geometry, with an environmental heating chamber (Anton Paar HTK 1200N), supporting resistive heating that can indirectly heat samples via a heating wire to up to ~1200 °C and features atmospheric control through gas and vacuum regulation. Samples were placed on a ceramic sample holder, and the temperature was monitored via an RhPt thermocouple. The anode material used as X-ray source was copper (Cu) for the in situ XRD, emitting Cu K α_1 and Cu Kα_2 radiation (ratio 2:1) with a wavelength of 1.5406 Å. The 2ϑ range was set between 15 and 100 degrees and a scan rate of 4° min^{-1} was applied. H_2 and C_2H_2 were fed via MFCs (Bronkhorst EL-flow select), with the before mentioned modular gas control unit. Pumping employed a combined small turbomolecular pump/rotary value pump stage (turbomolecular: Oerlikon leybold vacuum turbovac T50, rotary: Vacuubrand "chemistry hybrid pump" RC6).

2.5 In-situ X-ray Photoelectron Spectroscopy (XPS)

In-situ near ambient pressure X-ray photoelectron spectroscopy (NAP XPS) allows following the surface chemical evolution of our growth reaction under realistic process conditions in terms of temperature, gases and gas pressures. The bridging of the typically only UHV-compatible technique XPS with NAP capabilities is enabled via a nozzle system and differential pumping stage between the reaction chamber (~mbar range) and XPS analyzer (UHV conditions).

In-situ NAP XPS was conducted at two distinct synchrotron facilities. Namely, the CAT laboratory branches of the EMIL soft beamline, UE48/PGM, located at the synchrotron radiation facility BESSY II (Berlin)[127] and the CIRCE-NAPP branch of BL24 at the ALBA synchrotron (Barcelona).[128]

For the EMIL beamline, the focus points of both beamlines meet in a dedicated NAP-XPS analysis system based on a SPECS Phoibos 150 analyser, which covers the kinetic energy range up to 7 keV. The UHV system is described in detail elsewhere.[129,130] All XP spectra were recorded in normal photoemission geometry with a probing area of ~ 60 µm x 120 µm corresponding to the profile of the incident x-ray beam. The overall spectral resolution of the NAP-XPS system is about 0.4 – 0.5 eV at 10 eV pass energy. In order to get an overview of the sample, survey spectra were recorded using $\hbar\nu$ = 1250 eV photon energy. Fe 2p, O 1s and C 1s core levels were measured with $\hbar\nu$ = 1250 eV, 1050 eV and 800 eV, respectively.

For the CIRCE beamline near ambient pressure XPS (NAPXPS) was performed at the CIRCE-NAPP branch of BL24 at the synchrotron ALBA (Barcelone). The endstation is equipped with a Phoibos NAP150 electron analyzer from SPECS, positioned at the Magic Angle[131]. The available energy range at CIRCE is 90-2000 eV and the beam spot size is 100x20 (HxV) µm^2, although the vertical dimension is projected due to the almost horizontal position of the sample (grazing beam incidence). The overall energy resolution in experiment conditions (pass energy 10 eV, exit slit 20 µm) was better than 0.3 eV. Survey spectra were recorded using $\hbar\nu$ = 1060 eV photon energy. Fe 2p, O 1s and C 1s core levels were measured with $\hbar\nu$ = 1060 eV, 1060 eV and 515 eV, respectively.

The binding energy (BE) was calibrated using the valence band onset of metallic Fe with a pronounced Fermi edge with an accuracy of around 0.05 eV. Details on XPS data fitting process and parameters are given in individual chapters.

Bibliography

122. *The Handbook of infrared and raman characteristic frequencies of organic molecules* (ed Lin-Vien, D.) (Academic Press, Boston, 1991). 503 pp. ISBN: 978-0-12-451160-6.

123. Ferrari, A. C. & Robertson, J. Interpretation of Raman spectra of disordered and amorphous carbon. *Physical Review B* **61.** Publisher: American Physical Society, 14095–14107. doi:10.1103/PhysRevB.61.14095 (2000).

124. Graf, D. *et al.* Spatially Resolved Raman Spectroscopy of Single- and Few-Layer Graphene. *Nano Letters* **7.** Publisher: American Chemical Society, 238–242. ISSN: 1530-6984. doi:10.1021/nl061702a (2007).

125. Ferrari, A. C. & Robertson, J. Resonant Raman spectroscopy of disordered, amorphous, and diamondlike carbon. *Physical Review B* **64.** Publisher: American Physical Society, 075414. doi:10.1103/PhysRevB.64.075414 (2001).

126. Das, A. *et al.* Monitoring dopants by Raman scattering in an electrochemically top-gated graphene transistor. *Nature Nanotechnology* **3.** Publisher: Nature Publishing Group, 210–215. ISSN: 1748-3395. doi:10.1038/nnano.2008.67 (2008).

127. Hendel, S. *et al. The EMIL project at BESSY II: Beamline design and performance* in. Proceedings of the 12th international conference on synchrotron radiation instrumentation (New York, NY USA, 2016), 030038. doi:10.1063/1.4952861.

128. Pérez-Dieste, V. *et al.* Near Ambient Pressure XPS at ALBA. *Journal of Physics: Conference Series* **425,** 072023. ISSN: 1742-6596. doi:10.1088/1742-6596/425/7/072023 (2013).

129. Bluhm, H. *et al.* Methanol Oxidation on a Copper Catalyst Investigated Using in Situ X-ray Photoelectron Spectroscopy. *The Journal of Physical Chemistry B* **108,** 14340–14347. ISSN: 1520-6106, 1520-5207. doi:10.1021/jp040080j (2004).

130. Knop-Gericke, A. *et al.* in *Advances in Catalysis* 213–272 (Academic Press, 2009). doi:10.1016/S0360-0564(08)00004-7.

131. Werner, W. S. M. Magic angle for surface roughness for intensity ratios in AES/XPS. *Surface and Interface Analysis* **23.** _eprint: https://onlinelibrary.wiley.com/doi/pdf/ 696–704. ISSN: 1096-9918. doi:10.1002/sia.740231008 (1995).

CHAPTER 3

Realizing Scalable Chemical Vapour Deposition of Monolayer Graphene Films on Iron with Concurrent Surface Hardening by in situ Observations

3.1 Introduction

Two-dimensional (2D) materials, incl. graphene and 2D hexagonal boron nitride, have been heralded as ultimately thin functional corrosion barrier coatings for modern metallurgical alloys, incl. steels.[39,47] This is because 2D materials can highly selectively impede the transport of matter but enable the transport of energy/charge between their substrate and their environment over ultimately small thickness scales of just one or a few atoms. For instance, graphene on steel could (due to graphene's record impermeability to corrosive species[6,7]) impede corrosive diffusional processes between the steel and its environment while (due to its high conductivity[132,133]) still enabling highly efficient charge transfer between the steel and its environment to allow for, e.g., efficient current collector/electrode functionality with ultimately minimal coating thickness. Such complementary barrier functionality is much harder to achieve with conventional, typically much thicker (>100 nm) barrier coatings.[38] Likewise graphene coatings may offer additional functionality such as controlled wetting, anti-icing or biocompatibility.[83–85,134] Thus, substantial work has gone into coating metallurgical alloys and in particular steels with graphene as ultimately thin, functional barriers.[39,47]

The target for such coatings is to produce graphene films on steels with complete coverage, controlled layer numbers and good interfacing to the steel substrate.[39,47] To date however only structurally imperfect graphene coatings with incomplete coverage, high defect levels, low control over layer numbers and incomplete interfacing to substrate have been obtained on steels, be it from top-down liquid phase exfoliation[92–98] or bottom-up chemical vapour deposition (CVD).[89–91,110,111,135–137] Importantly, even on pure iron (Fe), the parent phase for all steels, to date no monolayered graphene films with complete coverage have been reported, let alone under scalable conditions.[67,70–76,78,79,138,139] This lack of graphene growth on even simple, pure Fe is thereby a clear hindrance to further advancing graphene growth on more complex, multi-element, multi-phased steels.

Towards filling this gap, this chapter shows the scalable CVD of monolayered graphene films on Fe substrates. Importantly, the CVD conditions applied here are scalable and compatible with current gas phase surface hardening/carburisation processes used in the metallurgical industry. Consequently, it is also demonstrated that the graphene CVD process also leads to concurrent surface hardening of the Fe substrates via carbon uptake into the Fe sub-surface and bulk. To achieve this goal of monolayer graphene film CVD on Fe, we here also elucidate the mechanisms of graphene growth on Fe using complementary in situ X-ray diffractometry (XRD) and in situ near ambient pressure (NAP) X-ray photoelectron spectroscopy (XPS) during our scalable CVD conditions to understand the complex interplay of the Fe's surface, sub-surface and bulk with the gaseous hydrocarbon CVD precursors and residual trace gases under kinetically-controlled CVD process conditions. In particular, we find that the controlled growth of high-quality monolayer graphene on iron has been challenging not only because of the non-trivial iron-carbon (Fe-C) phase diagram but also because of the inhibition of graphene growth due to persistent Fe surface oxidation. We investigate and overcome these challenges through our in situ characterisation-guided CVD process development. Our work thereby forms a holistic framework for the process development of controlled and scalable high-quality monolayer graphene CVD on Fe-type substrates, including the introduction of concurrent surface hardening, which we expect also to lay the basis for subsequent future expansion of graphene CVD coatings on persistently challenging steel substrates.

As discussed in the introductory chapter 1, graphene CVD is a bottom-up approach in which gaseous precursors (for graphene primarily hydrocarbons) are flown at elevated temperatures (~400 °C to ~1000 °C) over the desired growth support, leading to precursor breakdown and then (under the right process conditions) graphene growth.[56,140,141]

As prior work incl. ours has shown,[58,60,61] unlike conventional CVD of classical µm-thick coatings where the substrate is comparatively "inert", in graphene CVD the growth substrate has a highly active catalytic role via surface catalytic activity and also bulk solubilities/diffusivities.[56,59] In particular, substantial uptake of carbon, graphene's constituent element, into the growth substrate's bulk can occur during graphene CVD. This complicates graphene growth kinetics and requires close matching of CVD conditions (temperature profiles, precursor fluxes, etc.) with the growth substrate. In the past, graphene CVD has been optimised for dedicated, often sacrificial high-purity Cu and Ni metal growth catalyst supports[58,60,61,101,102] to fully covering layer-number-controlled, high-quality graphene films. In comparison, graphene CVD on Fe has been significantly lacking behind.[67,70–76,78,79,138,139]

The first factor that sets Fe apart from other catalyst substrates is the more complex, multi-phased Fe-C phase diagram (Figure 3.1). As we have shown prior for Ni and Cu catalyst substrates based on in situ investigations, graphene CVD follows a bulk-mediated surface growth mechanism.[58,60,61] This means that graphene CVD is governed both by surface processes (gaseous precursor breakdown and reorganisation of surface species into graphene nuclei/domains) and bulk-mediation in which precursor supersaturation by diffusion on the surface, into the subsurface and, depending on kinetics, also into the bulk of the support must be reached before graphene nucleation/growth can occur.[56,58–61] Then, growth can proceed isothermally on the surface and/or via precipitation from the bulk upon cooling.[58,60,61] Importantly, for a given catalyst support with given C solubility, the exact pathways of graphene CVD within the interplay of surface processes and bulk mediation can be kinetically controlled.[56,59] The key, hereby, is controlling the balance between incoming precursor flux, flux to the graphene's growth front and what flux is diffusing into the catalyst support bulk. In principle, isothermal surface growth typically leads to better control over 2D materials layer numbers, quality and coverage, while precipitation upon cooling typically leads to undefined growth with inhomogeneous layer numbers and coverage and poorer crystalline quality when using gaseous precursors and standard CVD methods.[55,101]

Compared to prior work on Ni and Cu catalyst supports, which we showed to remain single-phased during the entire graphene CVD process,[58,60,61] we find in this work that the here investigated Fe catalyst substrate can undergo substantial, temperature- and process-stage dependent phase transitions, e.g. body-centred-cubic (bcc) to face-centred-cubic (fcc) Fe during carbon feeding with strong increases to C solubility for $>727\,^{\circ}C$ after transition.[67,142,143] Such high, temperature-dependent solubility often

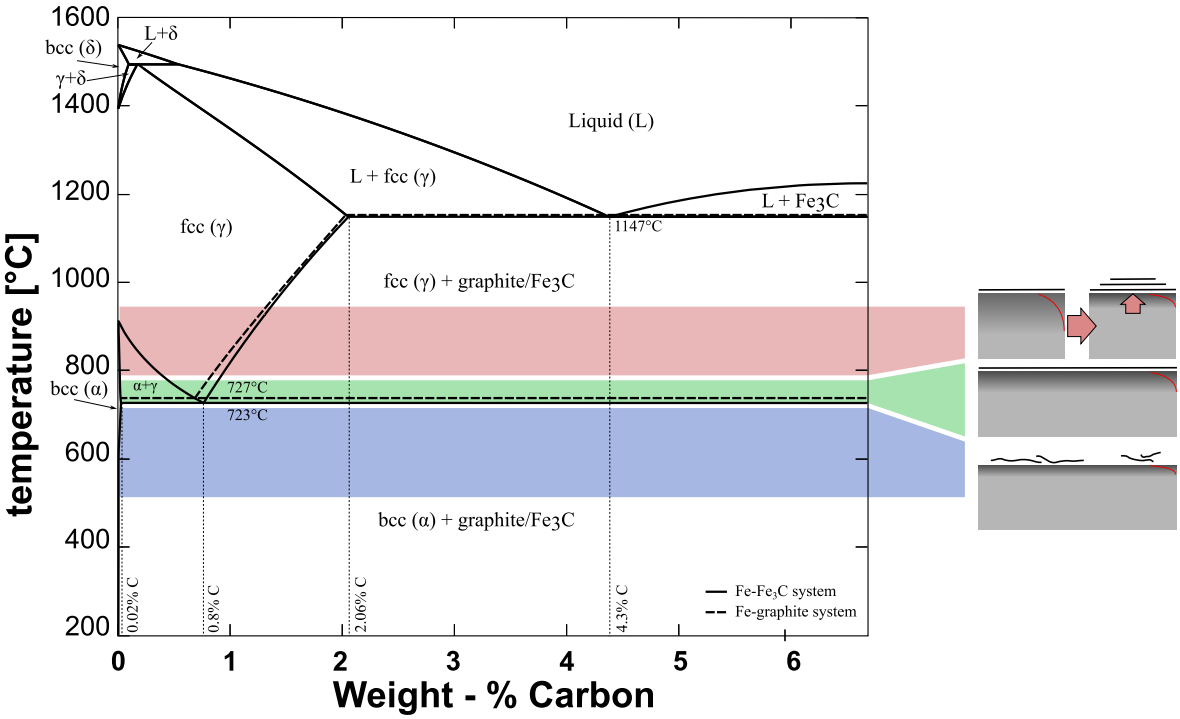

Figure 3.1: Schematic illustration of the Fe-C phase diagram for both Fe-graphite (dashed) and (metastable) Fe-Fe3C systems (plotted with OpenCalphad[144] and modified), with a schematic illustration of the main findings of this study regarding the interplay of CVD conditions and graphene growth results superimposed (see Discussion section).

favours precipitation from bulk 2D growth and thus typically yields 2D films of low quality when Fe-based supports are used.[101,103] As we demonstrate in this report, the key to overcoming this limitation is the identification of kinetic conditions for CVD in terms of temperatures, precursor concentrations and diffusion fluxes that nevertheless facilitate predominantly isothermal growth on Fe.

A second aspect that distinguishes Fe catalysts from widely used Ni and Cu graphene growth catalyst supports is Fe's propensity to readily form persistent surface oxides during Fe storage in ambient conditions before CVD and also from residual oxidising species (trace oxygen and water) in situ during CVD. Surface oxides typically completely suppress Fe catalytic ability for graphene CVD, or at best, lead to only defective graphene.[145] Therefore, a reduction step with reductive gases, e.g. annealing in H_2, is typically employed before hydrocarbon exposure in graphene CVD and a reductive gas is also typically added during the hydrocarbon exposure to suppress in situ oxidation. In comparison to Ni and Cu support, we show here, however, that typical reduction conditions with H_2 are insufficient for Fe reduction under scalable CVD conditions but that also carbothermal reduction of Fe-oxides from hydrocarbon exposure is a critical element of monolayer graphene CVD on Fe. This highlights that

not only the kinetics for graphene growth (as eluded to above) but also the kinetics for reduction of persistent Fe-oxides must be controlled for graphene CVD development on Fe.

A third aspect that is of particular usefulness for Fe is that the carbon uptake into the sub-surface and bulk during graphene CVD (that we here also evidence using in situ XRD and XPS) is reminiscent of industrially widely applied carburisation hardening (case hardening) for Fe/steels.[146] Exploring this aspect, we finally also demonstrate that under our optimised graphene CVD growth conditions, the remaining significant carbon uptake into the Fe bulk also leads to concurrent surface hardening of the Fe substrates. Thus, from a metallurgical application perspective, a beneficial interplay of concurrent graphene CVD and surface hardening is demonstrated here.

3.2 Methods

Graphene CVD. The CVD setup is described in detail in section 2.2. For a typical CVD run, samples undergo annealing in ~1 mbar reductive H_2 atmosphere (~250 sccm, Messer 2.1, 99.1% purity) at the respective growth temperature (500 °C to 800 °C) for 30 min (heating rate ~100 °C/min). Subsequently, 0.1 to 10 sccm of the carbon precursor acetylene (C_2H_2 , Messer 2.6, 99.6% purity) is added for another 30 min. The samples are afterwards left to cool naturally, or with the help of an external fan, in ~1 mbar H_2 with the split-tube furnace heaters opened around the quartz tube. The natural cooling rate is ~35 °C/min to ~300 °C, then ~15 min to room temperature, measured with the internal thermocouple of the oven. H_2 flow is controlled by a manual flow meter (Vögtlin Instruments GmbH, Q-Flow series) while C_2H_2 flow is controlled by a digital mass flow controller (MFC, Bronkhorst EL-flow select). We use 100 µm thick (Alfa Aesar Puratonic® 99.995%) polycrystalline iron foils as catalytic growth substrate.

Ex situ Characterisation. Samples are characterised ex-situ via optical microscopy and Raman spectroscopy (WITec alpha 300 RSA+) after CVD. Laser wavelength 532 nm, laser power 10 mW, spot size ~2 µm. Ex situ XRD measurements were conducted with a PANalytical X'Pert Pro multi-purpose diffractometer (MPD) with a standard rotating stage and chromium (Cr) anode as an X-ray source with a wavelength of 2.26 Å. Presented Cr anode ex-situ XRD patterns were scaled to make them comparable to the in situ XRD Cu anode datasets (see below). While most characterisation investigated the graphene growth results directly on their Fe growth substrates, for selected samples graphene film transfer[147] was done using a polymethylmethacrylate/ethyl acetate

mixture for drop casting a sacrificial polymer layer on top the graphene/Fe foil sample, followed by a bubbling transfer procedure,[148] before transferring the film onto a SiO_2(90 nm)/Si substrate and dissolving the PMMA layer in acetone.

For the bubbling transfer, the PMMA-coated graphene/Fe foil is dipped into 0.5 molar K_2SO_4 together with a glassy carbon electrode. A voltage of about 4-5 V is applied, with the glassy carbon electrode acting as the anode and the graphene/Fe foil acting as the cathode. Hydrogen bubbles are formed between the iron foil and the PMMA-supported graphene, separating the graphene from the substrate. Transferred graphene is characterised by Raman spectroscopy[149] and optical contrast analysis following a previously reported method.[150] Graphene coverage was calculated using simple visual measurements (thresholding of optical microscopy image) of graphene films on Fe and a transferred graphene film on a SiO_2(90 nm)/Si substrate. Coverage is potentially underestimated for the transferred films due to possible damage to the film during transfer.

In situ XRD. A detailed description of the in-situ XRD setup used in this chapter can be found in section 2.4

In situ XPS. In-situ NAP XPS experiments were performed at the CAT laboratory branches of the EMIL soft beamline, UE48/PGM, located at the synchrotron radiation facility BESSY II (Berlin).[127] Detailed experimental setup can be found in section 2.5.

Peak fitting was done in CasaXPS software[151] and the peak shapes in table 3.1 are given with the software command abbreviations. GL(30) denoting a Gaussian/Lorentzian product with 30 % Lorentzian contribution. LF denotes an asymmetric Lorentzian lineshape with a tail-dampening parameter.[152,153] FWHM of sp^2 peak was constrained to FWHM of adventitious carbon peak, measured initially on bare Fe and C-O component was constrained to follow sp^2 component FWHM. Fe-C components were also constrained to same the FWHM based on the FWHM of the peak at 283.2 eV. General peak shapes were based on work from Gengerbach et al..[154]

Peak designation	Peak position	Peak shape	FWHM
Fe-C	283.2 eV ± 0.1 eV	GL(30)	0.48 eV
Fe-C	283.7 eV ± 0.1 eV	GL(30)	0.48 eV
Sp^2	284.5 eV ± 0.1 eV	LF(0.65,1.1,700,180,3)	0.45 eV
Sp^3	284.8 eV ± 0.1 eV	GL(30)	0.69 eV
C-O	286 eV ± 0.1 eV	GL(30)	0.69 eV

Table 3.1: Peak fit Parameters for C1s spectrum shown in figure 3.10.

3.3 Results

3.3.1 Rationally designed CVD conditions

To ensure fine control over carbon flux, we base our CVD recipe on C_2H_2 as the hydrocarbon source. The investigated process parameters are initially based on prior by us developed CVD conditions for Ni catalyst supports.[58,60] C_2H_2 has the advantage of dissociating readily and being active for graphene growth already at lower temperatures from ~450 °C.[58] Thus C_2H_2 can be employed at low and well-controllable fluxes for graphene CVD. We here employ the C_2H_2 in a simple custom-built hot-wall quartz tube furnace with mass-flow-controlled C_2H_2 in-flux under medium-pressure CVD conditions obtained by a simple pump setup (base pressure 3×10^{-3} mbar). Detailed CVD process is described in the methods section 3.2. We emphasise that such CVD conditions are directly compatible with common carburisation hardening conditions in industrial surface hardening processes[146] and our CVD conditions are thus intrinsically industrially scalable. We deliberately chose the comparatively high thickness of the 100 µm Fe foils to also account for bulk effects that have been shown to play an important role for Ni catalysts.[56,59]

3.3.2 Optimisation of Graphene CVD Results

We first describe a survey of CVD parameter space to illustrate our optimised growth results before providing experimental (in situ) insights into the corresponding growth mechanisms further below. Figure 3.2 shows optical microscopy images (left) and corresponding, spot-localised Raman spectra (right, spot localisation indicated by coloured spectra/spots) of growth results on the Fe supports from the above describe CVD conditions for intermediate C_2H_2 flux of 1 sccm as a function of growth temperature from 500 °C to 800 °C (and referenced against as received Fe foil). For the as-received Fe foil, we find in optical microscopy and Raman[155,156] (green trace) that the foils have formed surface Fe-oxides from storage in ambient air.

After 500 °C CVD we find the Fe foil to be inhomogeneously covered by nanocrystalline graphite (red trace: intensity ratio D/G >2 and very low 2D intensity[123,157]) and amorphous carbon (blue trace: merged D and G, no 2D[158]) regions. Under these nanocrystalline graphene and amorphous carbon regions, no signs of remaining Fe-oxide are detected in Raman, implying a localised reduction of the Fe-oxides during the CVD process. The graphitisation level of the carbon deposits at 500 °C growth temperature

indicates insufficient thermal activation for healing defects in the growing carbon film.[159] With increasing temperature to 600 °C, we accordingly find an improvement in graphitisation levels: We grow inhomogeneous multilayer graphene films at 600 °C without (blue and red traces: intensity ratio D/G ~0.3; 2D/G ~0.7)[149] and with remaining Fe-oxides (green trace). When further increasing the growth temperature to 700 °C, we find further improvements in graphitisation, indicated by a further reduction in D/G ratio to <0.2.[149] Additionally, we now see an inhomogeneous mixture of multilayer graphene (blue trace) as well as monolayer graphene regions (red trace: 2D/G ~1.5).[149] Notably, however, persistent Fe-oxides are still detected (green trace).

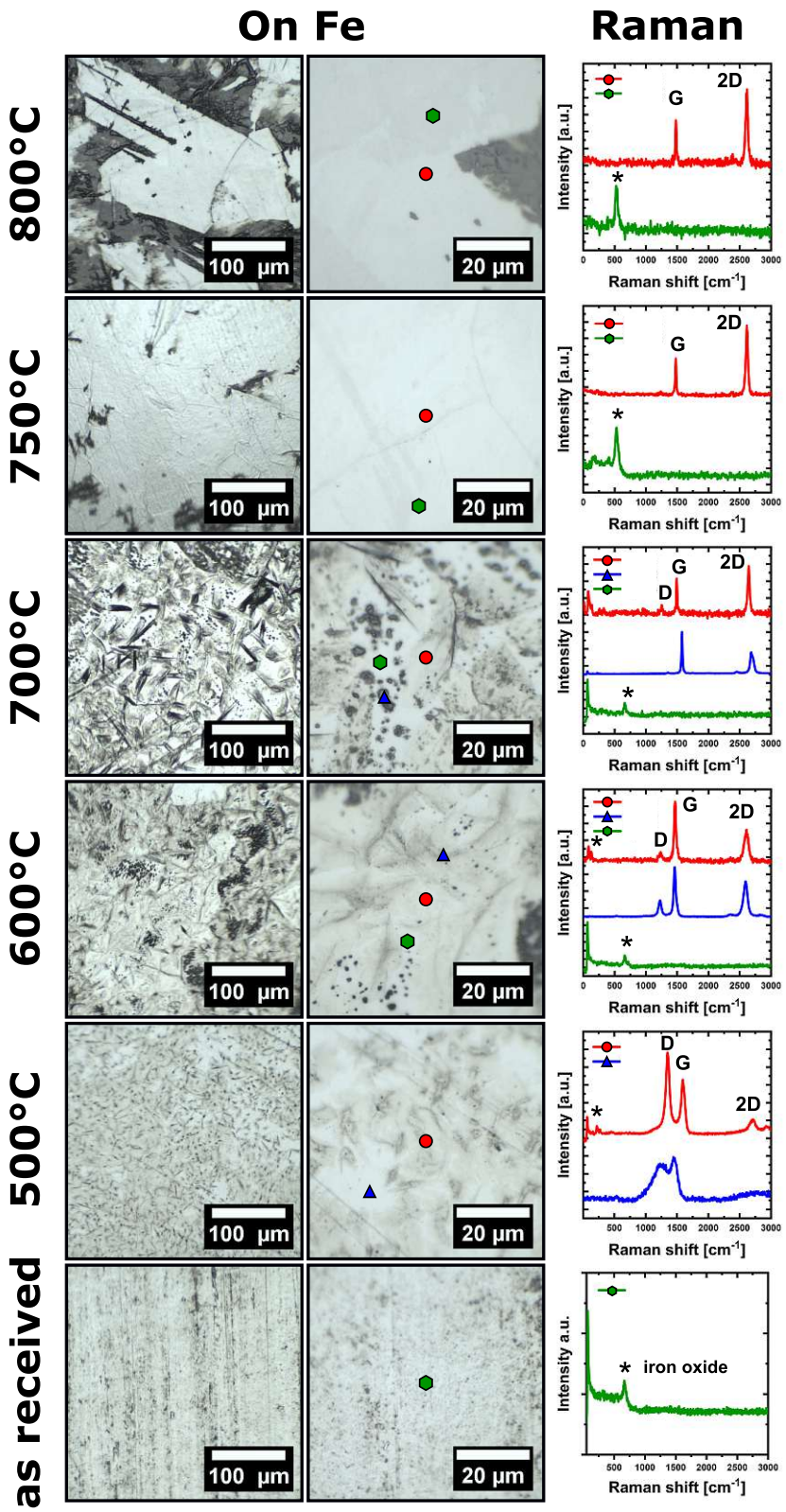

Figure 3.2: Optical micrographs (left and middle panel columns) at different magnifications and spot localised Raman spectra (right panel column, spot localisation indicated by colour-coded spectra/spots) of as received 100 µm Fe foils and growth results on Fe after CVD with 1 sccm C_2H_2 at temperatures from 500 °C to 800 °C. Carbon-related D, G and 2D Raman peaks[149] are labelled, and iron oxide-related peaks[155,156] are indicated with "*" in the Raman spectra.

Further increasing the growth temperature to 750 °C, we find clear improvements in homogeneity, importantly towards predominantly monolayer graphene growth of high-quality (red trace: D/G <0.05; 2D/G ~2).[149] Quantitatively, we estimate monolayer graphene sample coverage to ~70% (based on optical micrographs and Raman analysis of transferred films, see methods section 3.2). Remaining non-monolayer-graphene areas are comprised of isolated multilayer graphene islands to ~10% sample coverage (dark spots in leftmost optical micrograph) and remaining Fe-oxide regions (~20%), which are however void of graphene or carbon coverage (green trace). Thereby, monolayer and multilayer graphene regions combined cover ~80% of the iron substrate.

We further confirm our monolayer assignment of these graphene films (and exclude formation of turbostratic graphite) via a standard polymer-assisted transfer[147] of the films from their Fe support onto 90 nm SiO_2-coated Si wafers and further Raman and optical microscopy data in Figures 3.3 and 3.4. Interestingly, when further increasing the CVD temperature to 800 °C, we do not observe further improvements in controlled graphene coverage but instead obtain comparatively much more inhomogeneous carbon films with only a small fraction of monolayer graphene coverage (red trace) but large fractions of multilayer graphene growth (dark patches in leftmost image) as well as bare remaining Fe-oxide regions (green trace). Notably however growth at 800 °C retains similarly high graphitic quality[149] (D/G <0.05) as for 750 °C. This indicates that for 800 °C, graphitisation is expectedly good but other growth mechanistic factors are preventing predominant monolayer graphene film growth.

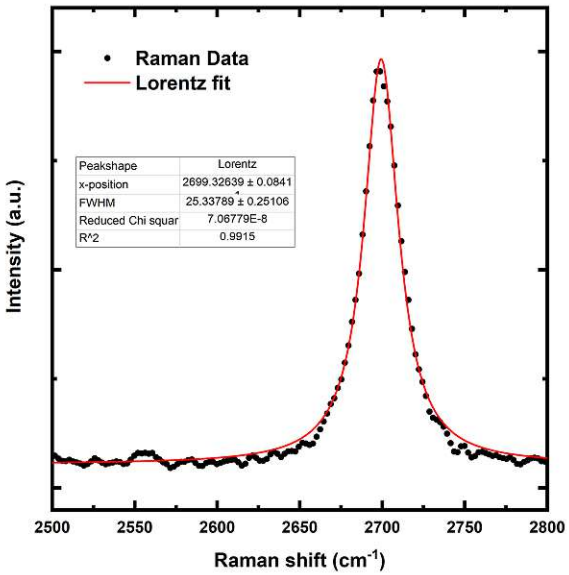

Figure 3.3: Raman 2D peak of monolayer graphene film transferred from iron substrate onto SiO_2 wafer and fit with single Lorentzian (FWHM = 25.3).[149]

Taking the so far best monolayer graphene results from CVD at 750 °C at 1 sccm C_2H_2 from Figure 3.2 as an optimised reference point, we then compare the effect of C_2H_2 flux in Figure 3.5. We however find that growth at lower C_2H_2 flux of ~0.1 sccm leads to only monolayer island growth with large areas of the substrate left covered in Fe-oxide. This indicates insufficient carbon flux. Conversely, growth at increased 10

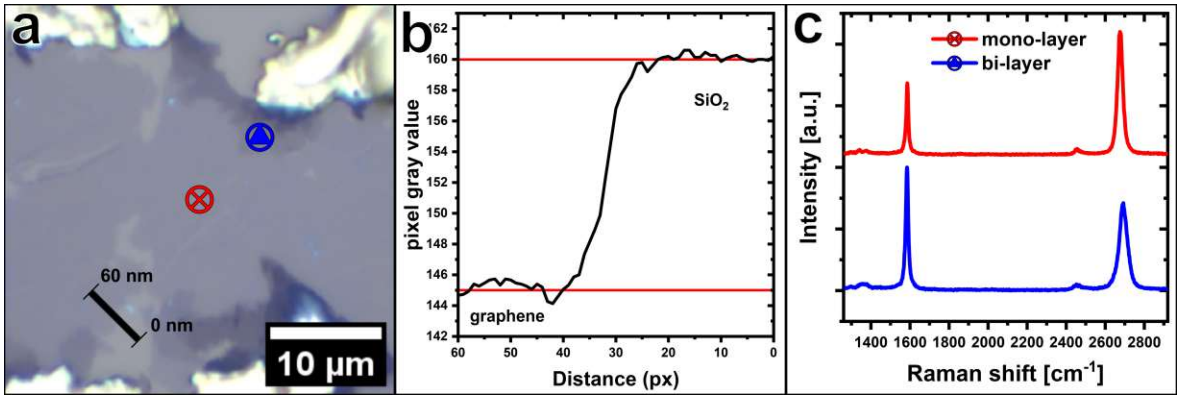

Figure 3.4: (a) Optical micrograph of CVD graphene from 750 °C/1 sccm C_2H_2 run from figure 3.2 after polymer-assisted graphene transfer to 90 nm SiO_2-covered Si wafer. (b) Corresponding optical microscope pixel grey values averaged along the indicated black line in (a). (c) Corresponding point-localised Raman spectra with locations in (a) indicated by colour and symbol.

sccm C_2H_2 flux leads to a relative increase in large-area multilayer graphitic growth, thus implying that 10 sccm C_2H_2 represents a too-high carbon flux for predominant monolayer growth. This suggests that overall, at 750 °C, the 1 sccm C_2H_2 flow rate, under the screened conditions, optimises the balance of incoming precursor carbon, carbon to the graphene's growth front and carbon diffusing into the catalyst support bulk, leading to the best monolayer graphene growth results.[56]

Overall, the here optimised results at 750 °C in Figure 3.2 go beyond prior literature on graphene CVD on Fe in terms of quality and monolayer coverage, particularly under scalable CVD conditions.[67,70–76,78,79,138,139]

3.3.3 Investigation of Growth Mechanisms

After having established an optimised graphene CVD protocol on Fe, we now turn to elucidating the underlying mechanisms, including in-situ investigations. We first investigate the key importance of, as we find, carbothermal surface Fe-oxide reduction during CVD growth before investigating the Fe-C phase and surface chemistry evolution in/on the Fe catalyst support foils during our optimised CVD conditions by complementary in situ XRD and in situ NAP XPS.

Importance of Carbothermal Reduction of Fe-oxides.
Our data in Figure 3.2 indicates that the presence of persistent surface Fe-oxides, which we detect as a minority surface coverage under practically all CVD conditions tested, is a remaining unfavourable factor in our graphene growth on Fe. Such Fe-oxides are

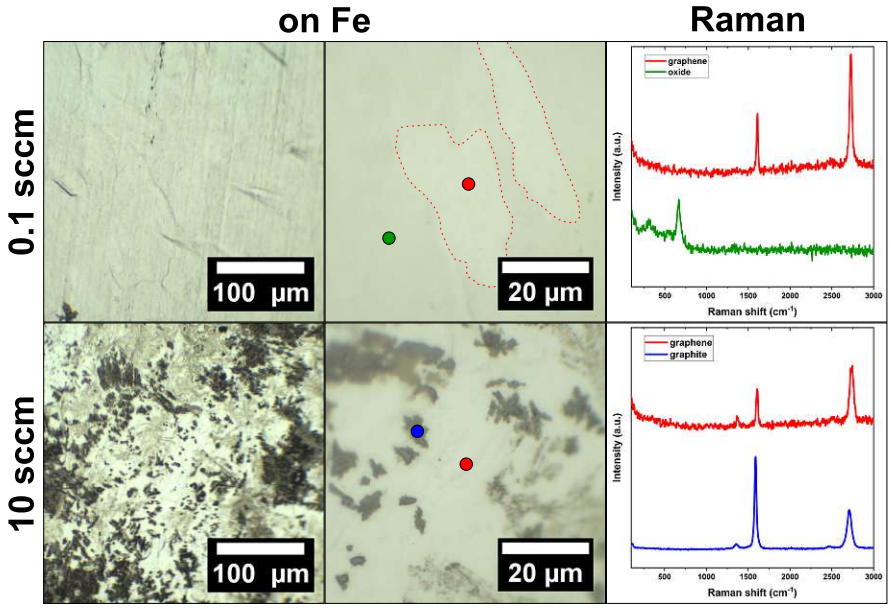

Figure 3.5: Optical micrographs (left and middle panels) at different magnifications and point localised Raman spectra (right panels) for 0.1 sccm (upper panels) and 10 sccm (lower panels) of C_2H_2 precursor flow at 750 °C CVD temperature. Dashed red outlines indicate high-quality monolayer graphene islands in upper middle panel. The upper right panel shows Raman spectra of monolayer graphene regions (red) and iron oxide regions (green). The lower right panel shows Raman spectra of graphitic multilayer regions (blue) and monolayer graphene regions (red).

detrimental to graphene growth because, generally, oxides are known to be much less suited to catalyse high-quality graphene during CVD.[106,160] Surface Fe-oxides can either form from ambient air during Fe catalyst support storage prior to CVD incl. subsequent Fe-oxide crystallisation during the high-temperature CVD process and/or from in situ oxidation of the Fe catalyst support from residual trace gases such as O_2 or water during the CVD process.[161] To counter both processes and reduce such Fe-surface oxides most CVD recipes, including ours, use a dedicated reductive pre-treatment step and/or a reductive ad-gas (both roles filled here by 1 mbar H_2) being present throughout the entire CVD process. Additionally, carbothermal reduction of the Fe-oxides from the hydrocarbon source (here C_2H_2) also may occur. This is, however, commonly not explicitly considered. Compared to other established graphene catalysts, Fe-oxides are known to be more stable and intrinsically harder to reduce than in comparison under their respective CVD conditions readily reducible Ni-oxides[58,60] and Cu-oxides.[61]

To therefore disentangle Fe-oxide formation and reduction processes under our CVD conditions, we conduct cross-check experiments: In Figure 3.6, we present optical microscopy and Raman spectroscopy results for 100 µm Fe foils that underwent the CVD process at 750 °C but without C_2H_2 addition i.e. samples only underwent an-

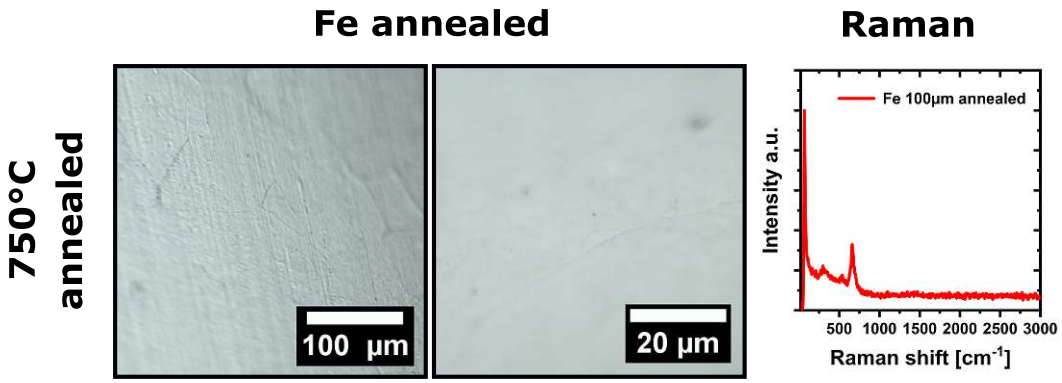

Figure 3.6: Left and middle panel show optical micrographs of H_2 annealed (750 °C) Fe samples at different magnification respectively. The right panel shows point localised Raman spectrum and iron-oxide signal (green trace), representative of the entire sample surface.

nealing in H_2. For these samples, we find no graphene growth (as expected due to no C_2H_2 exposure); however, despite the reducing H_2 conditions, the presence of a surface Fe-oxide over the entire Fe foil surface is detected. Together with the observed presence of an initial surface Fe-oxide in our as-received foils (Figure 3.2), this implies that under our conditions (and in our CVD furnace) the H_2 alone is not sufficient for initially present Fe-oxide reduction and suggests that the C_2H_2 under our process conditions has not only the role of graphene growth precursor but also of a carbothermal reduction agent, since only with C_2H_2 introduction, depicted in figure 3.2, the majority of the Fe has been reduced (as indirectly evidenced by the observed carbon growth). Our results in figure 3.2 however show that good graphene films can be achieved already by simple and well scalable vacuum conditions (~10^{-3} mbar base pressure) also for Fe.

Fe-C Phase Dynamics during CVD by in situ XRD.

After having ex-situ investigated the importance of enabling surface Fe-oxide reduction, including carbothermal reduction, we now investigate the Fe-C phase dynamics during graphene CVD on Fe catalyst supports. Figure 3.7 shows ex-situ XRD patterns of the Fe supports before and after CVD processing corresponding to Figure 3.2. As-received foils are at room-temperature of phase-pure metallic body-centered-cubic (bcc) Fe (α-Fe) structure in accordance with the phase diagram (Figure 3.1). No Fe-oxides are detected in XRD, implying that the Fe-oxides present in the Raman spectra (Figure 3.2) are only minor surface oxides. After CVD and subsequent cooling to room temperature, we find for all growth temperatures the majority phase to be bcc-Fe but a minority Fe-carbide phase has been formed additionally during CVD (Note the square-root scaled intensity scale in Figure 3.7 that strongly emphasises this minority Fe_3C phase. Rietveld refinement puts a maximum phase contribution of Fe_3C to ~12 %.). A graphite-related peak

is detected as a function of growth temperature in accordance with the presence and roughly the amount of multilayer graphene compared to Figure 3.2. The observation of a Fe-carbide signal in Figure 3.7 implies that during the CVD process, the Fe catalyst support is subjected to an influx of carbon into the catalyst bulk, resulting in the observed formation of an additional Fe_3C phase.

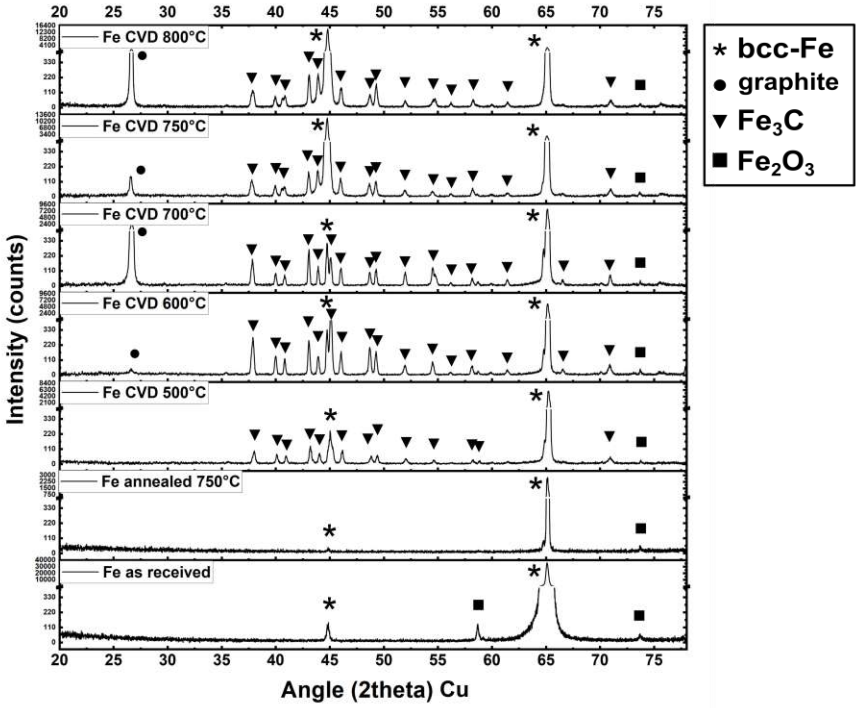

Figure 3.7: Ex-situ XRD patterns of Fe catalysts supports after CVD conditions corresponding to Figure 3.2, as received Fe foil and after only H_2 treatment ("annealed at 750 °C"). Salient phases identified are indicated. (International Centre for Diffraction Data (ICDD), PDF-5+ database, powder diffraction file entry: bcc-Fe 04-015-8438; Carbon/graphite 04-016-0554; Fe_3C 04-007-0422) Note that the intensity scale is square-root scaled and has interruptions for better visualisation of minor Fe_3C phase signal. Diffractograms measured with Cr X-ray anode then scaled to Cu radiation for easy comparison with Cu in-situ data.

To reveal the phase evolution of the Fe catalyst support during each CVD process step, we therefore turn in Figure 3.8 to process-step-resolved in situ XRD measurements during our optimised CVD conditions at ~750 °C . Here, we find that the initial bcc Fe retains its bcc Fe structure during the H_2 annealing step at 750 °C, but during the subsequent C_2H_2 exposure at 750 °C undergoes a phase transition towards face-centered-cubic Fe (γ-Fe) phase. This is direct evidence for the carbon influx into the catalyst bulk during the C_2H_2 exposure because according to the phase diagram (Figure 3.1), with increasing carbon concentration in the Fe, a phase transition from bcc to fcc Fe occurs for growth temperatures above the eutectoid temperature of ~723 °C.

Concurrently, we observe the emergence of a graphite peak during C_2H_2 exposure, giving direct evidence of isothermal graphene growth via our in situ XRD experiments. The observation of fcc Fe as the predominant phase during graphene CVD reaffirms that ex-situ XRD measurements such as in Figure 3.7 can not necessarily capture the relevant phase evolution (as no fcc Fe has been detected in Figure 3.7 at all) but that in situ experiments are necessary for Fe.[142,143] After CVD and after cooling to room temperature, we observe that the Fe has fully reverted to bcc Fe (again in agreement with the phase diagram in Figure 3.1). During our in situ XRD measurements, no indication for substantial Fe_3C formation during the CVD process was observed. We note, however, that our in-situ XRD runs in Figure 3.8 employed a Cu anode, which for Fe samples results in higher background due to fluorescence, while our ex situ XRD data in Figure 3.7 was measured with a Cr anode that allows for higher sensitivity.[162]

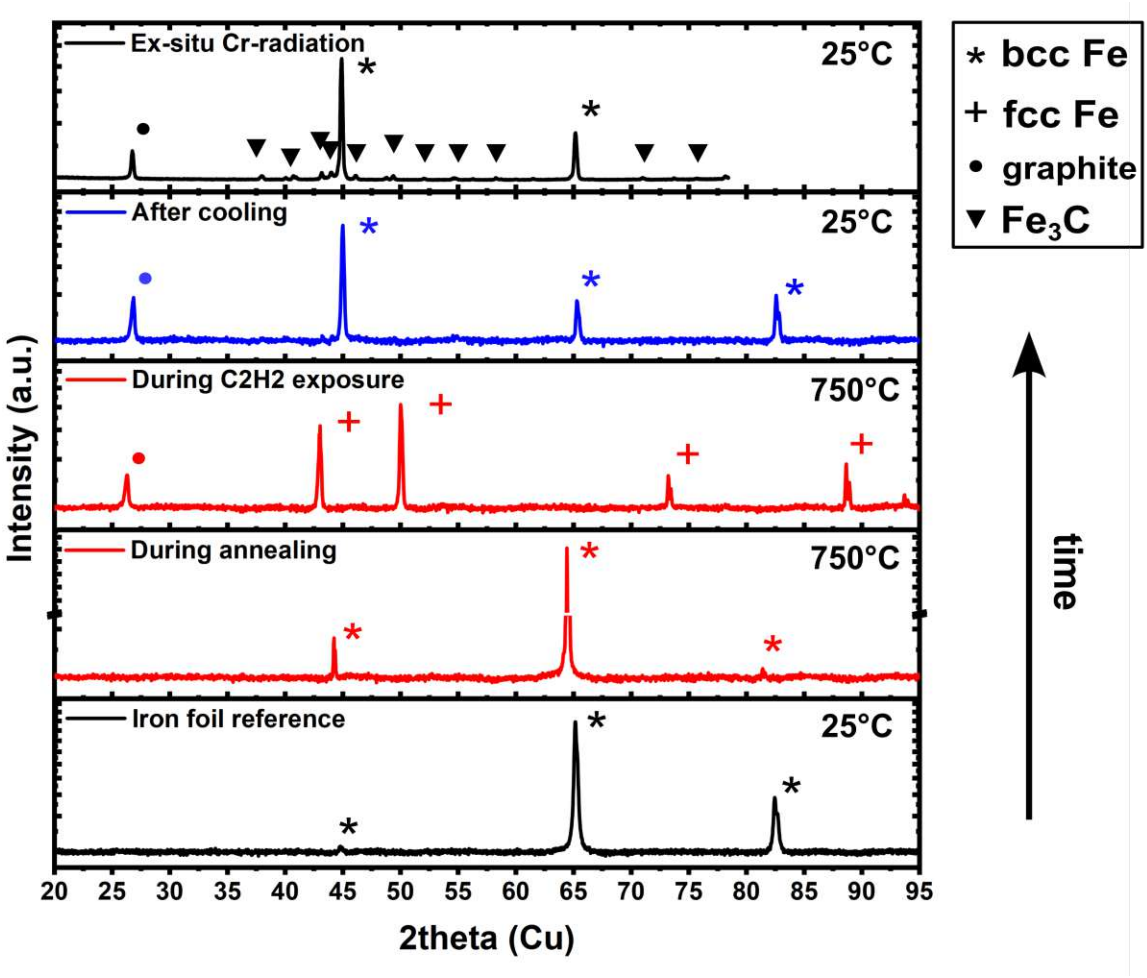

Figure 3.8: Process-step resolved in situ XRD patterns of the Fe catalyst support during CVD at ~750 °C. Process step conditions (from bottom to top) are indicated. Salient phases identified are indicated. (International Centre for Diffraction Data (ICDD), PDF-5+ database, powder diffraction file entry: bcc-Fe-ambient 04-015-8438; bcc-Fe-non-ambient 040-17-5839; fcc-Fe-non-ambient 04-003-1443; Carbon/graphite 04-016-0554; Fe_3C 04-007-0422) The in situ XRD patterns were measured with a Cu anode, resulting in higher background signal for Fe,[162] while the uppermost pattern was measured ex-situ after CVD with a Cr anode thus also detecting a minority Fe_3C phase that was below the sensitivity of the in situ Cu anode measurements (Cr anode pattern recalculated to 2-Theta angles comparable to Cu anode dataset). Note that the intensity scale is square root and has intensity scale interruption(s) for better visualisation of minority phase signals.

Conversely, when ex-situ remeasuring our in situ sample from Figure 3.8 with a Cr anode after CVD, we accordingly measure a minor Fe_3C signal (Top pattern in Figure 3.8. Note square root intensity scale in Figure 3.8, Rietveld refinement puts Fe_3C to the upper limit of ~12 %, fully consistent with the ex-situ growth in Figure 3.7), which could have formed either during C_2H_2 exposure or cooling. Combined, our in situ XRD data at optimised CVD conditions, therefore, indicates that fcc Fe is the majority phase in the Fe foils during growth and that a minority Fe_3C phase could possibly also

be present during growth. In either case, the above XRD data has confirmed carbon uptake into Fe as an important factor during growth (which results in the bcc to fcc Fe transition and Fe_3C formation) and that graphene growth occurs (at least partially) isothermally. However, the time resolution of our in situ XRD measurements is not sufficient to disentangle the dynamics of isothermal graphene growth and answer if growth via precipitation of prior dissolved carbon during cooling also contributes to graphene growth. We turn to in situ NAP XPS with better time resolution to answer these questions.

Surface evolution during CVD by in situ NAP XPS.

We employ in situ NAP XPS to study the surface evolution of carbon and Fe and their interactions throughout the graphene growth process at the same nominal condition as in our optimised growth from Figure 3.2. Notably, while we investigate the bulk of the Fe sample volume in our XRD measurements in Figure 3.8 (and at only tens of minutes time resolution), with the XPS measurements, we probe the uppermost few nm in the sample surface and sub-surface and at a time resolution of seconds.[102]

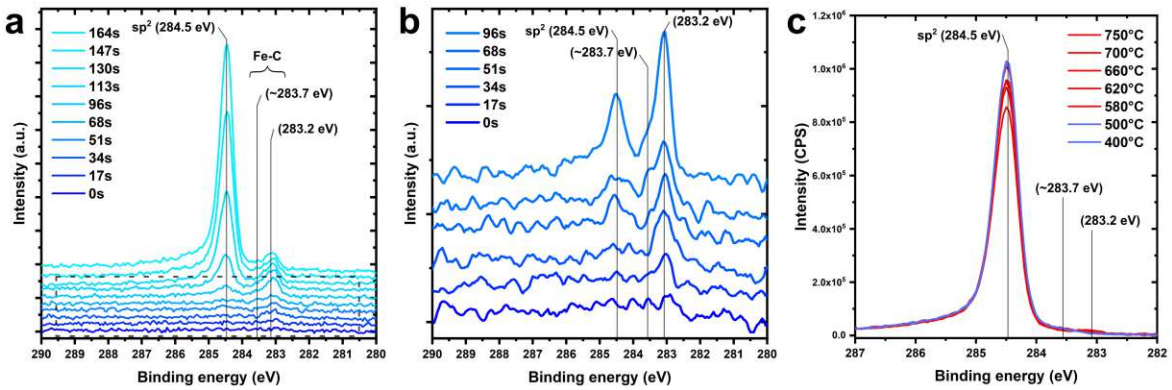

Figure 3.9: (a) C1s time-resolved in situ NAP XPS spectra during C_2H_2 exposure at 750 °C. Salient C1s components are indicated. (b) Zoom-in of marked region (dashed) in panel (a). (c) C1s time-resolved after C_2H_2 shut off during cooling in H_2 from 750 °C.

Figure 3.9(a,b) shows time-resolved C1s spectral evolution during C_2H_2 exposure step at 750 °C. The Fe sample is initially fully clean from adventitious carbon (removed during the H_2 pre-treatment) as evidenced by the flat C1s spectrum at 0 s in Figure 3.9(a,b). Upon C_2H_2 exposure, we first observe the emergence of a peak at 283.2 eV, starting at ~17 s. We ascribe this 283.2 eV peak to carbon bonded at iron surface sites based on previous work using Ni substrates.[60,163] This component also has an asymmetric shoulder towards higher binding energies at 283.7 eV (see in particular Figure 3.9b), which becomes more visible with time. This shoulder can be ascribed to

an additional C1s component at 283.7 eV, which we attribute to carbon dissolved in Fe, again based on prior work.[60,163] Both 283.2 eV component and 283.7 eV shoulder are thereby direct signs of carbon influx into the Fe, in excellent accordance with the XRD data above. We label both 283.2 eV and 283.7 eV components, therefore, as "Fe-C". Notably, both Fe-C components (283.2 eV, 283.7 eV) precede the first emergence of the C1s component of sp^2 graphene at 284.5 eV which emerges only after an incubation time after C_2H_2 introduction of ~51 s at 750 °C. Thereby, the Fe-C 283.2 eV and 283.7 eV components indicate the necessary carbon influx into the Fe subsurface before graphene nucleation can occur. After the first emergence of the sp^2 graphene at 284.5 eV signal at ~51 s, the graphene sp^2 signal overtakes the dissolved carbon components in intensity after ~113 s and then continues to rise with increasing C_2H_2 exposure time. This is further direct evidence of isothermal graphene growth on the Fe. In Figure 3.10, we show a detailed C1s component fit of a representative C1s XPS spectrum.

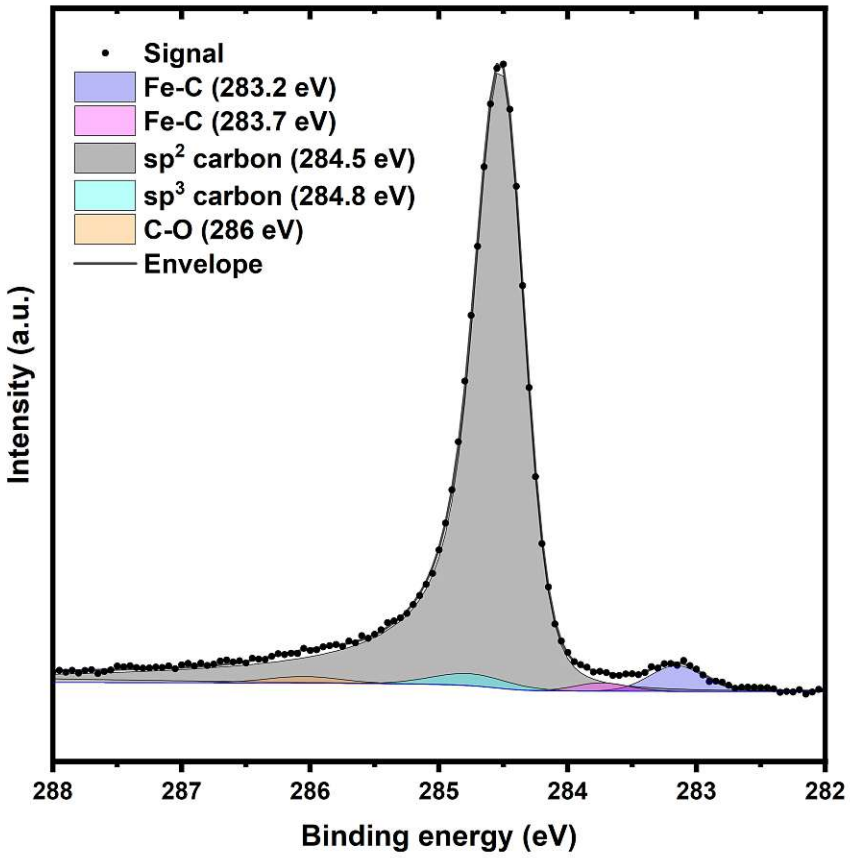

Figure 3.10: C1s spectrum during C_2H_2 exposure at ~750 °C with peak components fit to experimental data, taken from the evolution in Figure 3.9a. Detailed information on XPS peak fit parameters can be found in the methods section 3.2

To resolve if carbon precipitation upon cooling also contributes to graphene growth from Fe under our optimised conditions, we also follow the C1s evolution after C_2H_2

shut off during the cooling step (~50 °C/min in H_2) in a time-resolved fashion in Figure 3.9c. We find only a small increase of graphene C1s signal at 284.5 eV during cooling (by ~18 %), showing that under our growth conditions, additional graphene formation by precipitation of prior dissolved carbon from Fe upon temperature cooling is limited. This links excellently with the observed only minor multilayer graphene coverage in Figure 3.2 at optimised monolayer graphene growth conditions at 750 °C.

The in situ NAP XPS data thereby indicates that the growth kinetics for our 750 °C growth on Fe are well controlled towards almost exclusive isothermal graphene growth with minimal additional graphene growth by precipitation upon cooling. In line with the XRD data, this shows a significant carbon uptake into the Fe sub-surface (XPS) and bulk (XRD, TOF-SIMS) for these kinetic conditions as part of the graphene growth process. However, this carbon reservoir has minimal influence on graphene growth via precipitation upon cooling.

A corollary result of this finding is that when the iron (Fe) "reservoir" for carbon uptake into the Fe is increased, with otherwise similar carbon feeding flux, the growth kinetics should change toward a much higher contribution of precipitation upon cooling growth. We test this hypothesis by measuring in situ NAP XPS during higher temperature exposure at 800 °C. Based on the phase diagram at 800 °C (Figure 3.1), we would expect a significantly higher carbon solubility in Fe and thus a much larger free "reservoir" for carbon in the Fe at the higher temperature. This should, for instance, directly translate to a longer filling period of this "reservoir" and, thus, a longer carbon uptake period before graphene nucleation.

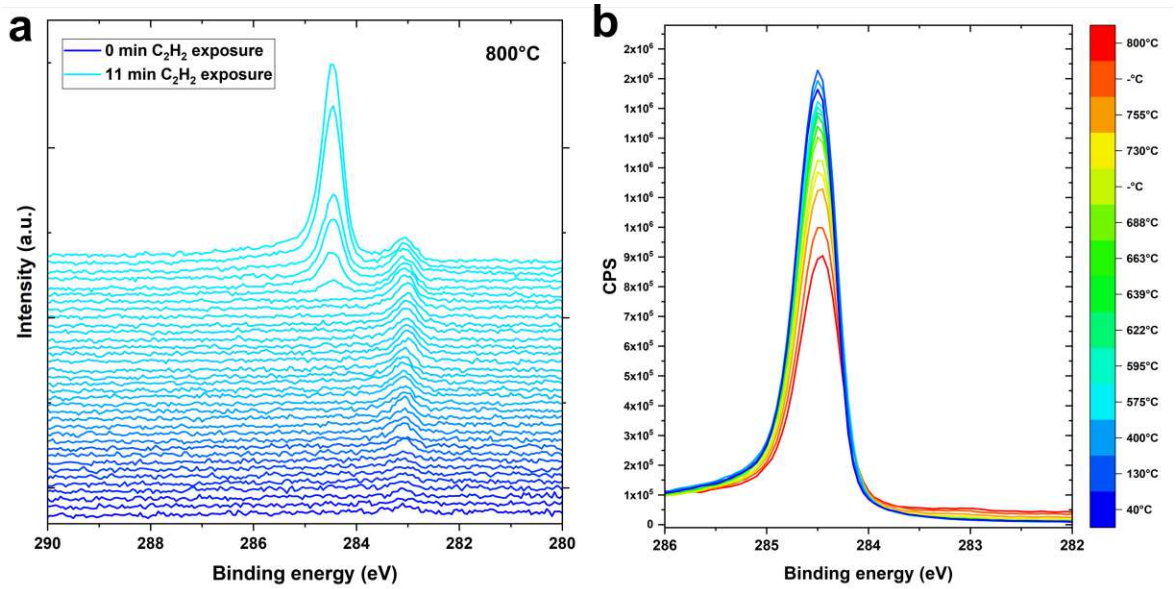

Figure 3.11: (a) Time-resolved in-situ XPS C1s spectra during C_2H_2 exposure at 800 °C showing an incubation of 10 minutes from hydrocarbon exposure start to start of isothermal surface carbon growth. Time increases from 0 s to 11 min of exposure from bottom to top. (b) C1s time-resolved spectra during substrate cooling in H_2 atmosphere from 800 °C after C_2H_2 shut off shows significant surface carbon intensity increase over time, reaching a plateau at around 400 °C.

Following this line of argument, we indeed find that the 800 °C growth temperature leads to a much-increased incubation period of ~10 min (i.e. ~10-times longer compared to only ~51 s at 750 °C) during which only the Fe-C components (283.2 eV, 283.7 eV) are visible before the graphene sp^2 signal at 284.5 eV appears and graphene isothermally grows. This is shown in the in-situ C1s data during C_2H_2 exposure at 800 °C in Figure 3.11a. Consistently, upon cooling from 800 °C after C_2H_2 exposure, a much more significant rise of the graphene C1s signal (284.5 eV) by 64 %) is evidenced (compared to only 18 % at 750 °C), confirming a much larger contribution of precipitation upon cooling to overall graphene growth at 800 °C (shown in Figure 3.11b). This is in excellent agreement with the increased multilayer fraction for growth results for 800 °C temperature compared to optimised 750 °C also in the ex-situ data in Figure 3.2.

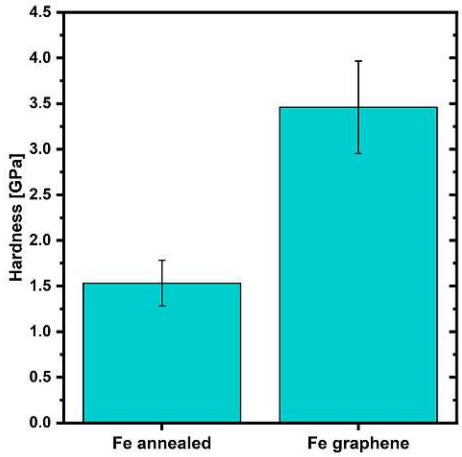

Figure 3.12: Hardness values from nanoidentation experiments for a graphene/Fe sample after optimised graphene CVD at 750 °C (1 sccm C_2H_2, Figure 3.2) against an only H_2 -annealed Fe reference sample (i.e. without C_2H_2 exposure), elucidating a surface hardening effect concurrent to graphene growth under our optimised CVD conditions.

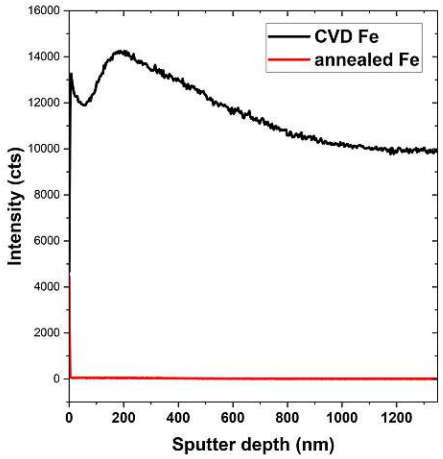

Figure 3.13: TOF-SIMS carbon anion C^- depth profile of H_2 annealed (without C_2H_2) reference Fe foil (red trace) and Fe foil after optimised CVD (black trace). The H_2 annealed Fe sample shows no significant carbon content. The CVD iron foil shows a large carbon signal and a slight decrease prior to levelling out, indicating a carbon-saturated substrate.

Concurrent Surface Hardening during Graphene CVD. After having established the key role of carbon influx into the Fe subsurface and bulk during the graphene CVD process via our (in situ) observations above, we consequently also probe the technological implication of this carbon influx. In particular, the here clearly observed carbon uptake into Fe is highly reminiscent of industrially widely applied carburisation hardening (case hardening) processes for Fe/steels.[146] Comparing a Fe sample that underwent optimised graphene CVD at 750 °C with a sample that underwent similar H_2 annealing at 750 °C but without the C_2H_2 exposure step (i.e. no graphene growth), we show in Figure 3.13 using depth-profiling of the carbon signal via time-of-flight secondary-ion-mass-spectrometry (TOF SIMS) that significant carbon uptake into the Fe bulk from the C_2H_2 exposure is evidenced (at least to ~1 µm depth) compared to a practically carbon-free only H_2 annealed Fe reference sample. This ex-situ data is thereby in excellent agreement with the (in situ) XRD and XPS data above. Consequently, we test which effect on Fe surface hardness this carbon uptake has: Employing nanoindentation measurements in Figure 3.12, we obtain hardness values for a graphene/Fe sample after optimised graphene CVD at 750 °C against a H_2-annealed Fe reference sample. The data in Figure 3.12 clearly shows a drastic increase in hardness by ~200 % that results from the carbon influx during graphene CVD. We thereby establish that surface hardening occurs concurrently with the graphene CVD process.

3.4 Discussion

This work provides a general framework for optimising graphene CVD on Fe. We illustrate our findings as schematic sketches to the Fe-C phase diagram in Figure 3.1.

Our data implies that at growth temperatures well below the Fe-C eutectoid (~723 °C), graphene growth on Fe is restricted by insufficient energy to nucleate and sustain high-quality graphene growth (but not by too large carbon uptake into the Fe bulk), explaining the graphene growth of low structural quality in Figure 3.2 below 750 °C. At ~750 °C we find that near the 723 °C eutectoid a kinetic balance between well crystallised isothermal graphene growth with only minimal additional carbon precipitation upon cooling can be achieved, resulting in our optimised conditions for high quality graphene growth with unprecedented monolayer coverage on Fe. For higher temperatures (≥800 °C), while structural graphene quality may further improve from the additional thermal energy, the drastically increasing carbon uptake into the Fe support during graphene CVD results, however, in a hard-to-control and increasing fraction of multilayer graphene growth from precipitation upon cooling. Thus, the higher growth temperatures (≥800 °C) again lead to worsened control over monolayer graphene coverage. Generally, finding a kinetic balance for graphene growth on Fe is critical for recipe development. We expect the above rationale to be applicable as a general guideline for the Fe-C system, albeit particular conditions will need adjustments for, e.g., sample sizes (i.e. more/less Fe volume to prefill during incubation time before graphene nucleation), hydrocarbon type (with C_2H_2 being fairly reactive) and desired growth times. We expect the general rationale also to hold for steels, although the effect of the multiple add-elements in modern steels will require further consideration individually, which is investigated in chapter 4.

Another general finding pertaining to Fe is the here-reported importance of controlling persistent Fe-surface oxides that can inhibit graphene growth and are harder to remove than in typical Ni- or Cu-based graphene recipes (which we can use without signs of persistent oxides on Ni or Cu in our CVD system[147])(see chapter 5 and appendix A.1). We show however that, in conjunction with the implicated carbothermal reduction observed during hydrocarbon exposure, the simple and scalable vacuum conditions employed in this study are sufficient to account for the heightened propensity of Fe-oxide formation relative to other typical graphene growth substrates.

Finally, we demonstrate that the carbon uptake during graphene CVD is not only

relevant for a more complete mechanistic understanding of graphene CVD on Fe but also has, via the here introduced concurrent surface hardening during graphene CVD, technologically beneficial implications. In particular we demonstrate the potential of development for combined graphene growth and surface hardening processes for metallurgical materials, which is an aspect that remained little addressed in the literature.

3.5 Conclusions

In summary, we have developed a CVD process for the growth of graphene on iron substrates that can produce high-quality monolayer graphene films with monolayer coverage of ~70 % and total graphene coverage of ~80 % under scalable CVD conditions. This represents a significant improvement of monolayer graphene CVD on Fe and is a prerequisite for growing graphene on more complex multi-element iron alloys such as steels. To obtain direct insights into the underlying growth mechanisms, we have followed the entire graphene CVD process on Fe using complementary in situ techniques to probe bulk crystallographic (in situ XRD) and surface chemical (in situ NAP XPS) evolution during CVD. Using this approach, we identified that specifically (i) carbothermal reduction of persistent Fe-oxides and (ii) kinetic balancing of carbon uptake into the Fe during CVD near the Fe-C eutectoid are critical for high-quality monolayer graphene CVD. Furthermore, we demonstrated that the carbon diffusion into the Fe is not only interesting from a growth mechanistic point of view but akin to industrial surface hardening processes (carburisation/case hardening) and, as such, can be beneficially utilised for establishing concurrent graphene CVD and surface hardening processes, as we also demonstrated in this work.

3.6 Publication Notice

This chapter has been submitted for publication and is listed as number 1 in the publication list.

Bibliography

6. Bunch, J. S. *et al.* Impermeable atomic membranes from graphene sheets. *Nano Letters* **8,** 2458–2462. ISSN: 15306984. doi:10.1021/nl801457b (2008).

7. Sun, P. Z. *et al.* Limits on gas impermeability of graphene. *Nature* **579,** 229–232. ISSN: 0028-0836. doi:10.1038/s41586-020-2070-x (2020).

38. Prasai, D., Tuberquia, J. C., Harl, R. R., Jennings, G. K. & Bolotin, K. I. Graphene: Corrosion-Inhibiting Coating. *ACS Nano* **6,** 1102–1108. ISSN: 1936-0851, 1936-086X. doi:10.1021/nn203507y (2012).

39. Böhm, S. Graphene against corrosion. *Nature Nanotechnology* **9.** Publisher: Nature Publishing Group, 741–742. ISSN: 17483395. doi:10.1038/nnano.2014.220 (2014).

47. Camilli, L., Yu, F., Cassidy, A., Hornekær, L. & Bøggild, P. Challenges for continuous graphene as a corrosion barrier. *2D Materials* **6.** ISSN: 20531583. doi:10.1088/2053-1583/ab04d4 (2019).

55. Caneva, S. *et al.* Controlling Catalyst Bulk Reservoir Effects for Monolayer Hexagonal Boron Nitride CVD. *Nano Letters* **16,** 1250–1261. ISSN: 1530-6984. doi:10.1021/acs.nanolett.5b04586 (2016).

56. Cabrero-Vilatela, A., Weatherup, R. S., Braeuninger-Weimer, P., Caneva, S. & Hofmann, S. Towards a general growth model for graphene CVD on transition metal catalysts. *Nanoscale* **8.** Publisher: The Royal Society of Chemistry, 2149–2158. ISSN: 2040-3372. doi:10.1039/C5NR06873H (2016).

58. Weatherup, R. S. *et al.* In situ characterization of alloy catalysts for Low-temperature graphene growth. *Nano Letters* **11,** 4154–4160. ISSN: 15306984. doi:10.1021/nl202036y (2011).

59. Weatherup, R. S., Dlubak, B. & Hofmann, S. Kinetic control of catalytic CVD for high-quality graphene at low temperatures. *ACS Nano* **6,** 9996–10003. ISSN: 19360851. doi:10.1021/nn303674g (2012).

60. Weatherup, R. S. *et al.* On the Mechanisms of Ni-Catalysed Graphene Chemical Vapour Deposition. *ChemPhysChem* **13,** 2544–2549. ISSN: 1439-7641. doi:10.1002/cphc.201101020 (2012).

61. Kidambi, P. R. *et al.* Observing graphene grow: Catalyst-graphene interactions during scalable graphene growth on polycrystalline copper. *Nano Letters* **13,** 4769–4778. ISSN: 15306984. doi:10.1021/nl4023572 (2013).

67. Xue, Y. *et al.* Synthesis of large-area, few-layer graphene on iron foil by chemical vapor deposition. *Nano Research* **4,** 1208–1214. ISSN: 19980000. doi:10.1007/s12274-011-0171-4 (2011).

70. You, Y. *et al.* A Controlled Carburization Process to Obtain Graphene–Fe3C–Fe Composites. *Advanced Materials Interfaces* **5,** 1–7. ISSN: 21967350. doi:10.1002/admi.201800599 (2018).

71. Park, E., Ostrovski, O., Zhang, J., Thomson, S. & Howe, R. Characterization of phases formed in the iron carbide process by X-ray diffraction, mossbauer, X-ray photoelectron spectroscopy, and raman spectroscopy analyses. *Metallurgical and Materials Transactions B* **32,** 839–845. ISSN: 1543-1916. doi:10.1007/s11663-001-0071-1 (2001).

72. Vinogradov, N. A. *et al.* Formation and structure of graphene waves on Fe(110). *Physical Review Letters* **109,** 1–5. ISSN: 00319007. doi:10.1103/PhysRevLett.109.026101 (2012).

73. An, H., Lee, W. J. & Jung, J. Graphene synthesis on Fe foil using thermal CVD. *Current Applied Physics* **11.** Publisher: Elsevier B.V, S81–S85. ISSN: 15671739. doi:10.1016/j.cap.2011.03.077 (2011).

74. Tripathi, K., Gyawali, G. & Lee, S. W. Graphene Coating via Chemical Vapor Deposition for Improving Friction and Wear of Gray Cast Iron at Interfaces. *ACS Applied Materials and Interfaces* **9,** 32336–32351. ISSN: 19448252. doi:10.1021/acsami.7b07922 (2017).

75. Lavin-Lopez, M. P., Fernandez-Diaz, M., Sanchez-Silva, L., Valverde, J. L. & Romero, A. Improving the growth of monolayer CVD-graphene over polycrystalline iron sheets. *New Journal of Chemistry* **41.** Publisher: Royal Society of Chemistry, 5066–5074. ISSN: 13699261. doi:10.1039/c7nj00281e (2017).

76. Khan, S. *et al.* Low-Temperature Synthesis of Graphene and Fabrication of Top-Gated Field Effect Transistors without Using Transfer Processes. doi:10.1143/APEX.3.025102 (2010).

78. Liu, N. *et al.* Universal Segregation Growth Approach to Wafer-Size Graphene from Non-Noble Metals. *Nano Letters* **11.** Publisher: American Chemical Society, 297–303. ISSN: 1530-6984. doi:10.1021/nl103962a (2011).

79. Anguita, J. V., Pozegic, T. R., Ahmad, M. & Silva, S. R. P. Layer-by-Layer Growth of Graphene Sheets over Selected Areas for Semiconductor Device Applications. *ACS Applied Nano Materials* **4,** 5211–5219. ISSN: 25740970. doi:10.1021/acsanm.1c00620 (2021).

83. Podila, R., Moore, T., Alexis, F. & Rao, A. M. Graphene coatings for enhanced hemo-compatibility of nitinol stents. *RSC Advances* **3,** 1660–1665. ISSN: 20462069. doi:10.1039/c2ra23073a (2013).

84. Zhang, L. *et al.* Graphene enhanced anti-corrosion and biocompatibility of NiTi alloy. *NanoImpact* **7,** 7–14. ISSN: 2452-0748. doi:10.1016/j.impact.2016.10.003 (2017).

85. Li, J. *et al.* CVD growth of graphene on NiTi alloy for enhanced biological activity. *ACS Applied Materials and Interfaces* **7,** 19876–19881. ISSN: 19448252. doi:10.1021/acsami.5b06639 (2015).

89. Dumée, L. F. *et al.* Growth of nano-textured graphene coatings across highly porous stainless steel supports towards corrosion resistant coatings. *Carbon* **87,** 395–408. ISSN: 00086223. doi:10.1016/j.carbon.2015.02.042 (C 2015).

90. Zhu, M. *et al.* Low-Temperature in Situ Growth of Graphene on Metallic Substrates and Its Application in Anticorrosion. *ACS Applied Materials & Interfaces* **8,** 502–510. ISSN: 1944-8244. doi:10.1021/acsami.5b09453 (2016).

91. Nazarova, M. *et al.* Growth of graphene on tantalum and its protective properties. *Carbon* **139.** Publisher: Elsevier Ltd, 29–34. ISSN: 00086223. doi:10.1016/j.carbon.2018.06.027 (2018).

92. Chang, C.-H. *et al.* Novel anticorrosion coatings prepared from polyaniline/graphene composites. *Carbon* **50,** 5044–5051. ISSN: 0008-6223. doi:10.1016/j.carbon.2012.06.043 (2012).

93. Aneja, K. S., Bohm, S., Khanna, A. S. & Bohm, H. L. M. Graphene based anticorrosive coatings for Cr(VI) replacement. *Nanoscale* **7.** Publisher: The Royal Society of Chemistry, 17879–17888. ISSN: 2040-3372. doi:10.1039/C5NR04702A (2015).

94. Tong, Y., Bohm, S. & Song, M. The capability of graphene on improving the electrical conductivity and anti-corrosion properties of Polyurethane coatings. *Applied Surface Science. 7th International Conference on Advanced Nanomaterials, 2nd International Conference on Graphene Technology, 1st International Conference on Spintronics Materials* **424,** 72–81. ISSN: 0169-4332. doi:10.1016/j.apsusc.2017.02.081 (2017).

95. Krishnan, M. A. *et al.* Graphene-based anticorrosive coatings for copper. *RSC Advances* **8.** Publisher: The Royal Society of Chemistry, 499–507. ISSN: 2046-2069. doi:10.1039/C7RA10167H (2017).

96. Raine, T. P. *et al.* Graphene/Polyamide Laminates for Supercritical CO2 and H2S Barrier Applications: An Approach toward Permeation Shutdown. *Advanced Materials Interfaces* **5,** 1800304. ISSN: 2196-7350. doi:10.1002/admi.201800304 (2018).

97. Yu, F. *et al.* Complete long-term corrosion protection with chemical vapor deposited graphene. *Carbon* **132,** 78–84. ISSN: 0008-6223. doi:10.1016/j.carbon.2018.02.035 (2018).

98. Singhbabu, Y. N., Sivakumar, B., Choudhary, S. K., Das, S. & Sahu, R. K. Corrosion-protective reduced graphene oxide coated cold rolled steel prepared using industrial setup: A study of protocol feasibility for commercial production. *Surface and Coatings Technology* **349,** 119–132. ISSN: 0257-8972. doi:10.1016/j.surfcoat.2018.05.046 (2018).

101. Bayer, B. C. *et al.* Introducing Overlapping Grain Boundaries in Chemical Vapor Deposited Hexagonal Boron Nitride Monolayer Films. *ACS Nano* **11,** 4521–4527. ISSN: 1936086X. doi:10.1021/acsnano.6b08315 (2017).

102. Bayer, B. C. *et al.* In Situ Observations of Phase Transitions in Metastable Nickel (Carbide)/Carbon Nanocomposites. *Journal of Physical Chemistry C* **120,** 22571–22584. ISSN: 19327455. doi:10.1021/acs.jpcc.6b01555 (2016).

103. Caneva, S. *et al.* Nucleation control for large, single crystalline domains of monolayer hexagonal boron nitride via Si-doped Fe catalysts. *Nano Letters* **15,** 1867–1875. ISSN: 15306992. doi:10.1021/nl5046632 (2015).

106. Kidambi, P. R. *et al.* Hafnia nanoparticles – a model system for graphene growth on a dielectric. *physica status solidi (RRL) – Rapid Research Letters* **5.** _eprint: https://onlinelibrary.wiley.com/doi/pdf/10.1002/pssr.201100155, 341–343. ISSN: 1862-6270. doi:10.1002/pssr.201100155 (2011).

110. John, R., Ashokreddy, A., Vijayan, C. & Pradeep, T. Single-and few-layer graphene growth on stainless steel substrates by direct thermal chemical vapor deposition. *Nanotechnology* **22.** ISSN: 09574484. doi:10.1088/0957-4484/22/16/165701 (2011).

111. Gullapalli, H., Mohana Reddy, A. L., Kilpatrick, S., Dubey, M. & Ajayan, P. M. Graphene growth via carburization of stainless steel and application in energy storage. *Small* **7,** 1697–1700. ISSN: 16136810. doi:10.1002/smll.201100111 (2011).

123. Ferrari, A. C. & Robertson, J. Interpretation of Raman spectra of disordered and amorphous carbon. *Physical Review B* **61.** Publisher: American Physical Society, 14095–14107. doi:10.1103/PhysRevB.61.14095 (2000).

127. Hendel, S. *et al. The EMIL project at BESSY II: Beamline design and performance* in. Proceedings of the 12th international conference on synchrotron radiation instrumentation (New York, NY USA, 2016), 030038. doi:10.1063/1.4952861.

132. Lim, S., Park, H., Yamamoto, G., Lee, C. & Suk, J. W. Measurements of the Electrical Conductivity of Monolayer Graphene Flakes Using Conductive Atomic Force Microscopy. *Nanomaterials* **11.** Number: 10 Publisher: Multidisciplinary Digital Publishing Institute, 2575. ISSN: 2079-4991. doi:10.3390/nano11102575 (2021).

133. Chen, F., Xia, J., Ferry, D. K. & Tao, N. Dielectric Screening Enhanced Performance in Graphene FET. *Nano Letters* **9,** 2571–2574. ISSN: 1530-6984, 1530-6992. doi:10.1021/nl900725u (2009).

134. Fickl, B. *et al. Controllable Freezing Transparency for Water Ice on Scalable Graphene Films on Copper* 2024. doi:10.48550/arXiv.2403.15629. arXiv: 2403.15629[cond-mat].

135. Yamada, T., Kim, J., Ishihara, M. & Hasegawa, M. Low-temperature graphene synthesis using microwave plasma CVD. *Journal of Physics D: Applied Physics* **46.** Publisher: IOP Publishing, 063001. ISSN: 0022-3727. doi:10.1088/0022-3727/46/6/063001 (2013).

136. Memon, N. K., Kear, B. H. & Tse, S. D. Transition between graphene-film and carbon-nanotube growth on Nickel alloys in open-atmosphere flame synthesis. *Chemical Physics Letters* **570.** Publisher: Elsevier B.V., 90–94. ISSN: 00092614. doi:10.1016/j.cplett.2013.03.046 (2013).

137. Romani, E. C. *et al.* Graphene Grown by Chemical Vapour Deposition on Steel Substrates: Friction Behaviour. *Tribology Letters* **65.** Publisher: Springer US. ISSN: 15732711. doi:10.1007/s11249-017-0879-8 (2017).

138. Chen, L. *et al.* Growth of Uniform Monolayer Graphene Using Iron-Group Metals via the Formation of an Antiperovskite Layer. *Chemistry of Materials* **27.** Publisher: American Chemical Society, 8230–8236. ISSN: 15205002. doi:10.1021/acs.chemmater.5b02788 (2015).

139. Zheng, R. *et al.* Low-temperature growth of graphene on iron substrate by molecular beam epitaxy. *Thin Solid Films* **627,** 39–43. ISSN: 0040-6090. doi:10.1016/j.tsf.2017.02.057 (2017).

140. Li, X. *et al.* Large-area synthesis of high-quality and uniform graphene films on copper foils. *Science* **324,** 1312–1314. ISSN: 00368075. doi:10.1126/science.1171245. arXiv: 0905.1712 (2009).

141. Yu, Q. *et al.* Graphene segregated on Ni surfaces and transferred to insulators. *Applied Physics Letters* **93,** 113103. ISSN: 0003-6951, 1077-3118. doi:10.1063/1.2982585 (2008).

142. Wirth, C. T. *et al.* The phase of iron catalyst nanoparticles during carbon nanotube growth. *Chemistry of Materials* **24,** 4633–4640. ISSN: 08974756. doi:10.1021/cm301402g (2012).

143. Bayer, B. C. *et al.* Nitrogen controlled iron catalyst phase during carbon nanotube growth. *Applied Physics Letters* **105.** ISSN: 00036951. doi:10.1063/1.4897950 (2014).

144. Lukas, H. L., Fries, S. G. & Sundman, B. Computational thermodynamics: the CALPHAD method. OCLC: ocm85829278 (2007).

145. Hofmann, S. *et al.* State of Transition Metal Catalysts During Carbon Nanotube Growth. *The Journal of Physical Chemistry C* **113.** Publisher: American Chemical Society, 1648–1656. ISSN: 1932-7447. doi:10.1021/jp808560p (2009).

146. Schneider, M. J. & Chatterjee, M. S. Introduction to Surface Hardening of Steels. doi:10.31399/asm.hb.v04a.a0005771 (2013).

147. Fuchs, D. *et al.* Electrochemical Behavior of Graphene in a Deep Eutectic Solvent. *ACS applied materials & interfaces* **12,** 40937–40948. ISSN: 1944-8252. doi:10.1021/acsami.0c11467 (2020).

148. Gao, L. *et al.* Repeated growth and bubbling transfer of graphene with millimetre-size single-crystal grains using platinum. *Nature Communications* **3,** 699. ISSN: 2041-1723. doi:10.1038/ncomms1702 (2012).

149. Ferrari, A. C. Raman spectroscopy of graphene and graphite: Disorder, electron-phonon coupling, doping and nonadiabatic effects. *Solid State Communications* **143,** 47–57. ISSN: 00381098. doi:10.1016/j.ssc.2007.03.052 (2007).

150. Blake, P. *et al.* Making graphene visible. *Applied Physics Letters.* ISBN: 0003-6951. ISSN: 00036951. doi:10.1063/1.2768624. arXiv: 0705.0259 (2007).

151. *CasaXPS* version 2.3.19PR1.0. 1999.

152. Fairely, N. CasaXPS Manual 2.3. 15. *Casa Software Ltd,* 1–177 (2009).

153. *CasaXPS Manual-LA_Lineshape* http://www.casaxps.com/help_manual/manual_updates/LA_Lineshape.pdf.

154. Gengenbach, T. R., Major, G. H., Linford, M. R. & Easton, C. D. Practical guides for x-ray photoelectron spectroscopy (XPS): Interpreting the carbon 1s spectrum. *Journal of Vacuum Science & Technology A* **39.** Publisher: American Vacuum Society, 013204. ISSN: 0734-2101. doi:10.1116/6.0000682 (2021).

155. Chamritski, I. & Burns, G. Infrared- and Raman-Active Phonons of Magnetite, Maghemite, and Hematite: A Computer Simulation and Spectroscopic Study. *The Journal of Physical Chemistry B* **109.** Publisher: American Chemical Society, 4965–4968. ISSN: 1520-6106. doi:10.1021/jp048748h (2005).

156. Wang, A., Kuebler, K. E., Jolliff, B. L. & Haskin, L. A. Raman spectroscopy of Fe-Ti-Cr-oxides, case study: Martian meteorite EETA79001. *American Mineralogist* **89,** 665–680. ISSN: 0003004X. doi:10.2138/am-2004-5-601 (2004).

157. Ferrari, A. C. & Robertson, J. Raman spectroscopy of amorphous, nanostructured, diamond-like carbon, and nanodiamond. *Philosophical Transactions of the Royal Society A: Mathematical, Physical and Engineering Sciences* **362.** Publisher: Royal Society, 2477–2512. ISSN: 1364503X. doi:10.1098/rsta.2004.1452 (2004).

158. Dennison, J. & Holtz, M. Raman spectroscopy of carbon materials. *Spectroscopy (Santa Monica)* **11,** 38–46 (1996).

159. Weatherup, R. S. *et al.* Introducing carbon diffusion barriers for uniform, high-quality graphene growth from solid sources. *Nano Letters* **13,** 4624–4631. ISSN: 15306984. doi:10.1021/nl401601x (2013).

160. Bayer, B. C. *et al.* Co-Catalytic Solid-State Reduction Applied to Carbon Nanotube Growth. *The Journal of Physical Chemistry C* **116.** Publisher: American Chemical Society, 1107–1113. ISSN: 1932-7447. doi:10.1021/jp210137u (2012).

161. Bayer, B. C. *et al.* Support−Catalyst−Gas Interactions during Carbon Nanotube Growth on Metallic Ta Films. *The Journal of Physical Chemistry C* **115.** Publisher: American Chemical Society, 4359–4369. ISSN: 1932-7447. doi:10.1021/jp102986f (2011).

162. Mos, Y. M., Vermeulen, A. C., Buisman, C. J. N. & Weijma, J. X-Ray Diffraction of Iron Containing Samples: The Importance of a Suitable Configuration. *Geomicrobiology Journal.* Publisher: Taylor & Francis. ISSN: 0149-0451 (2018).

163. Bleu, Y. *et al.* Dynamics of carbon diffusion and segregation through nickel catalyst, investigated by in-situ XPS, during the growth of nitrogen-doped graphene. *Carbon* **155,** 410–420. ISSN: 0008-6223. doi:10.1016/j.carbon.2019.08.084 (2019).

CHAPTER 4

In-situ near ambient pressure XPS of graphene CVD process on industrially relevant steel substrates

4.1 Introduction

The protection of steel surfaces from environmental degradation is a crucial concern across various industries, including also recently in sustainable energy storage and conversion applications. For example, as mentioned in section 1.2.5, stainless steel, known for its mechanical stability and durability, is a promising candidate for replacing conventional graphite bipolar plates in fuel cells or to be used as inexpensive current collectors in batteries.[107–109] In such applications, where steel components would be exposed to harsh (corrosive) operating conditions, the need for effective corrosion protection is particularly important while however also requiring efficient electron transport in/out of the steel. Stainless steel has the ability to form a corrosion-protective oxide layer under oxidative conditions within, e.g., a fuel cell. However, this layer can unintentionally hinder its performance and efficiency by impeding electron transfer across the electrode interface.[107] Even though a decade of research has been conducted on this topic and coatings have been devised that improve corrosion resistance and have smaller interfacial contact resistance, the main challenge to produce a cost-effective and commercially viable metal bipolar plate still remains.[108,109]

As elaborated, the remarkable combination of mechanical strength, electrical conductivity and barrier capability of graphene, offers an intriguing solution to this challenge. As an ultra-thin, electrically conductive material, graphene has the potential to act as a protective coating for stainless steel bipolar plates, mitigating the adverse effects of oxide formation while maintaining their current-collection capability.

The most prominent synthesis route for the scalable production of high-quality graphene films on metals is chemical vapour deposition (CVD). While CVD growth of monolayer graphene on high purity, sacrificial metal catalyst substrates such as copper and nickel is possible on a wafer scale,[57] even graphene grown on iron, the parent phase of all steels, has so far been of only limited structural quality, limited control over layer numbers and/or coverage[70,73,75,164] or under non-scalable conditions.[72] This is explained by iron's high carbon solubility, it's tendency to form oxides and carbides and the generally complex Fe-C phase diagram, leading to phase changes and possible phase separations during the CVD process, which is was discussed in more detail in section 1.

In particular, iron and steel substrates are known to yield significant amounts of multilayer graphene through the secondary growth mechanism of carbon precipitation during substrate cooling.[137,165]

In chapter 3, large-scale predominantly monolayered, high-quality graphene films on pure iron substrates were shown to be achievable with a scalable low-pressure CVD approach using acetylene (C_2H_2) gas as a precursor. In particular, it was shown, using complementary in-situ characterisation during the scalable CVD conditions by in-situ near ambient pressure X-ray photoelectron spectroscopy (NAP XPS) and in situ X-ray diffractometry (XRD), what kinetic conditions in terms of hydrocarbon precursor feeding rates and temperatures are necessary for monolayered graphene film growth on Fe. Key to the optimised growth was a delicate balance of C_2H_2 flux at 750 °C near the eutectoid temperature in the Fe-C system. Under these kinetic conditions, enough thermal energy was provided for high-quality graphene formation, but the carbon uptake into the Fe bulk after phase transformation to higher carbon solubility fcc phase, and therefore also the precipitation during cooling, was limited.

In this study, we employed our in situ approach to tackle the even more complex task of graphene CVD on steels. In particular, we selected three distinct steel grades of industrial significance and increasing complexity for our graphene CVD in situ studies. The primary material is a mild low carbon (~0.08 weight-%), low-alloy steel (DN

1.0338) used mainly for cold forming, as a closely related system to the pure iron Fe substrate we used in the previous chapter. However, the low-alloy steel is significantly less expensive than the high-purity Fe substrates previously utilised. We continued our investigation with an archetypical medium-alloyed construction steel ("DC01" DN 1.0330) with higher carbon content (≤0.12 weight-%) and one alloying element (<0.6 weight-% Mn). Finally, we explored the growth of graphene on a complex high-alloy CrNiMo high-alloy stainless steel (DN 1.4404) as the most complex steel substrate. For all steel types, we followed the surface chemical evolution of the growing carbon layers and the steel substrates for the entire graphene growth process using in-situ NAP XPS under CVD conditions.

We demonstrate that graphene growth on inexpensive mild low-carbon steel is of comparable quality to that observed in our previous work on the more expensive, pure Fe. In contrast, a simple translation of the optimised CVD process on Fe to the medium-alloyed construction steel with higher carbon content and additional alloy element content is not possible. We find that the inherently high carbon content in the steel interferes with graphene growth, leading to only partial or disordered carbon growth under our CVD conditions. To combat this detrimental effect, we devise a two-step growth procedure including dynamic cleaning of excess surface carbon based on our in-situ insights. With this adapted process we achieve few-layered graphene of good structural quality on the medium-alloy steel. For the high-alloy stainless steel, our in-situ study reveals that inhibition of graphene growth by persistent (Cr-)oxides can be overcome by better vacuum conditions, whereby we achieve growth improvements to a continuous nanocrystalline graphite film on the highly alloyed stainless steel based on our in-situ insights. Combined, our in-situ derived findings establish a mechanistic framework for developing graphene CVD on steels.

4.2 Methods

Steel samples Three steel samples of different compositions were investigated (detailed compositions shown in table 4.1). The detailed descriptions of the samples as well as the lab-CVD and in-situ XPS setup and procedures can be found in the general methods section in chapter 2.

In-situ NAP XPS procedure. General annealing and exposure process is analogous to procedure in capter 3, unless otherwise specified. The oxygen cleaning procedure was

Steel grade	% C	% Si	% Mn	% S	% P	% Mo	% N	% Ni	% Cr
DN1.0338	0.08	0.09	0.32	0.01	0.01	–	–	0.02	0.02
DN1.0330	0.12	–	0.6	0.045	0.045	–	–	–	–
DN1.4404	0.02	0.5	1.35	0.002	0.036	2.05	0.03	10.10	16.64

Table 4.1: Steel compositions of the three steel samples given in maximum wt% of alloying elements. (–) denotes elements that are not specified by the producer. This, however, does not guarantee that the steel does not contain these elements.

done after the initial reduction in ~1 mbar H_2. O_2 gas was leaked into the evacuated chamber at a pressure of ~5 x 10^{-6} mbar at a temperature of ~600 °C. Afterwards, the sample was re-annealed in H_2 at ~700 °C before C_2H_2 exposure at ~750 °C.

4.3 Results and Discussion

4.3.1 Unalloyed Low-alloyed low-carbon steel DN 1.0338

We regard this low-alloyed low-carbon steel (DN 1.0338, steel composition in section 4.2 Table 4.1) with low carbon content (<0.08 weight-%) as the first next step in increasing complexity from the pure iron Fe substrate from our prior work towards graphene growth CVD on multi-elemental complex steel substrates. Optical micrograph and Raman spectrum of as received surface in Figure 4.1 show that the low-alloyed steel surface is initially free of significant carbon deposits as evidenced by a flat Raman signal. Visually rolling striations from cold rolling are apparent on the as-received steel surface, which is common for metal foils.

Therefore, we employ the same rationally designed CVD conditions as for pure Fe substrates, based on C_2H_2 as our hydrocarbon precursor gas. We employ these CVD conditions both ex-situ in a lab-based furnace system ("ex-situ") and in situ during NAP XPS measurements ("in-situ"). Temperatures and gas feeding in the in-situ experiments are kept as close as technically possible to the ex-situ conditions. The only key exception between ex-situ conditions and in-situ conditions is a much better base pressure of ~10^{-8} mbar in in-situ conditions compared to only ~10^{-3} mbar in ex-situ conditions.

The CVD process runs at medium feeding gas pressure (~1 mbar) and a temperature of 750 °C in a custom-built hot-wall split tube furnace with a simple pump setup (base pressure ~1 x 10^{-3} mbar), detailed in chapter 2. The samples first undergo an annealing step in a reductive hydrogen H_2 environment (~1 mbar, typically 30 min) prior to hydrocarbon exposure, preparing the steels for graphene growth by reducing native

metal surface oxides from handling and storage in ambient air and increasing crystallite size. The H_2 is also retained as a background gas in order to maintain a reductive atmosphere and improve graphene growth in the following growth step when C_2H_2 is introduced. After growth with C_2H_2 of typically ~30 min, the C_2H_2 is shut off and the sample is left to cool naturally in ~1 mbar H_2 .

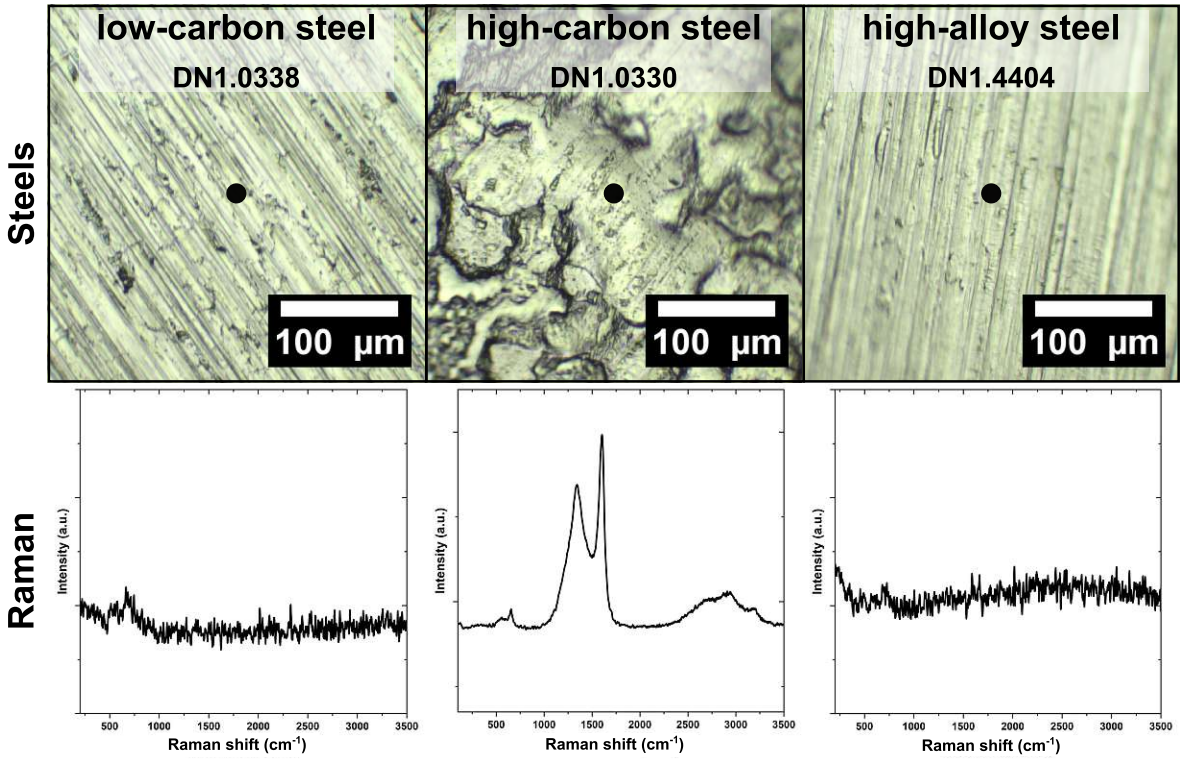

Figure 4.1: Optical micrographs (upper panels) and corresponding point localized Raman spectra (lower panels) of the as received steel sample surfaces. The top panel shows the low-carbon (DN 1.0338) steel with the Raman spectrum indicating small amounts of surface oxides. The middle panel shows the high-carbon (DN 10330) steel with the Raman indicating surface oxidation and a significant amount of graphitic disordered surface carbon. The lower panel shows the high-alloyed (DN 1.4404) stainless steel with the Raman spectrum indicating minimal surface oxidation.

In Figure 4.2 optical microscopy images of the steel substrate surface after ex situ CVD processing are shown together with point localised Raman spectra. We find the Fe surface to be covered by a mix of defect-free mono-layer graphene regions and few-layer graphene regions with higher defect density. In Figure 4.3 optical microscopy images of the steel substrate surface after in-situ CVD processing in the NAP XPS are shown together with a point localised Raman spectrum, this time with predominantly monolayer growth of low defect graphene ($I_D/I_G = 0.3$), accompanied by minority multilayer graphitic regions.

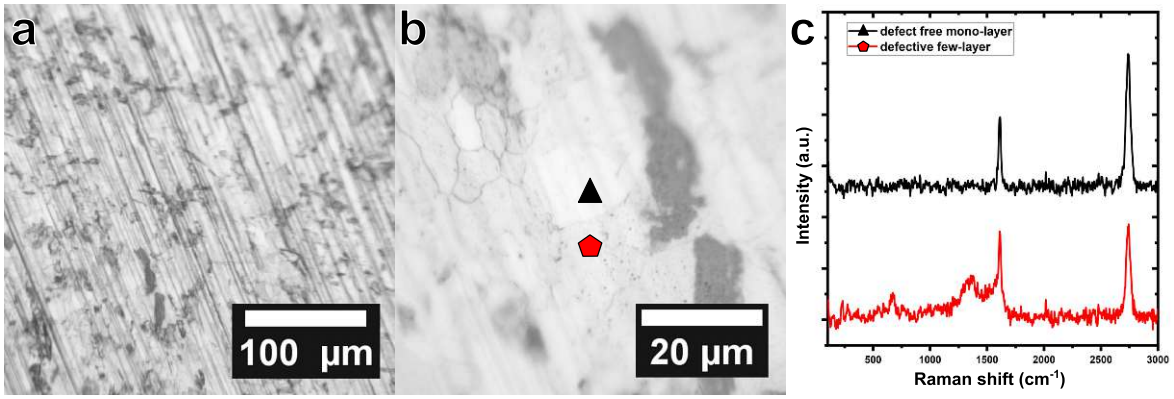

Figure 4.2: (a) Optical micrograph of steel surface after ex-situ CVD process (20x magnification). (b) Optical micrograph of steel surface after ex-situ CVD process (100x magnification) with marked locations of point localized Raman spectra displayed in panel c. (c) Point localized Raman spectra of indicated locations in panel b of high-quality graphene areas and defective few-layer regions.

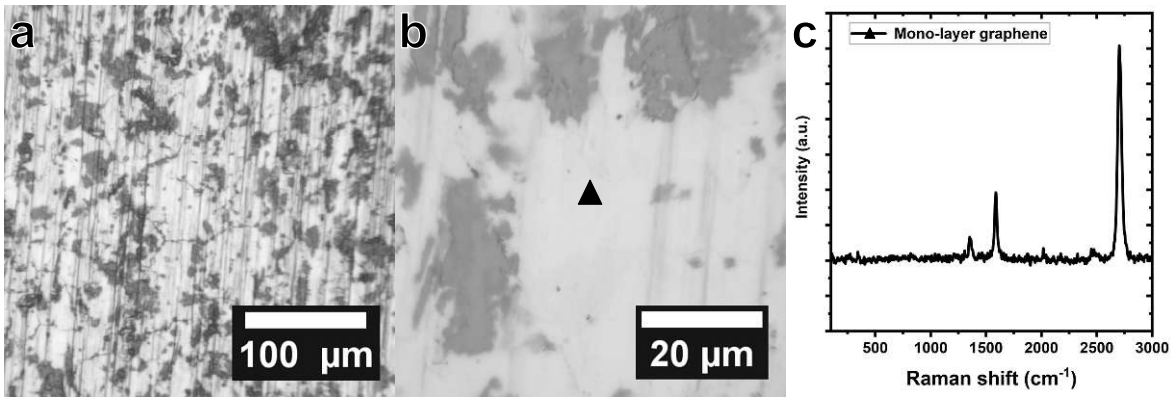

Figure 4.3: (a) Optical micrograph of steel surface after in situ XPS CVD process (20x magnification). (b) Optical micrograph of steel surface after in situ XPS CVD process (100x magnification) with marked locations of point localized Raman spectrum displayed in panel c. (c) Point localized Raman spectrum of indicated location in panel b of mono-layer graphene area.

The coverage and quality of the graphene growth on the low-alloyed steel is comparable to the growth that we have previously achieved on pure Fe substrates. This demonstrates that our scalable CVD conditions are applicable not only on ultra-pure metals but also allow for low-cost metal substrates with inherent impurities in the form of inexpensive low-alloy steel. We emphasise that the transferability of a CVD recipe between an expensive high purity metal substrate and a cheaper lower purity substrate is often not so straightforward, as e.g. show for prior results on Cu where graphene growth quality decreased with decreasing Cu substrate purity.[166]

We now proceed to analyse the in-situ NAP XPS data recorded during the in-situ graphene CVD on the low-alloyed steel. As shown in Figure 4.4, the as-loaded steel

sample shows surface carbon contamination (285.1 eV), which based on the binding energy we ascribe to mostly adsorbed adventitious hydrocarbons from sample storage and handling in air. This carbon signal is reduced by a factor of 94 % to a minimal C1s signal during annealing in H_2 at elevated temperature (~750 °C), and its position shifts to around 284.6 eV, indicating the graphitisation of the minimal remaining surface-/intrinsic carbon on the surface of the substrate. We note that in comparison, the pure Fe substrate did show a completely flat baseline after H_2 pre-treatment (shown in Figure 3.9), indicating that the minimal persistent C1s signal on the low-alloy steel may be directly connected to the 0.08 weight-% carbon in the steel.

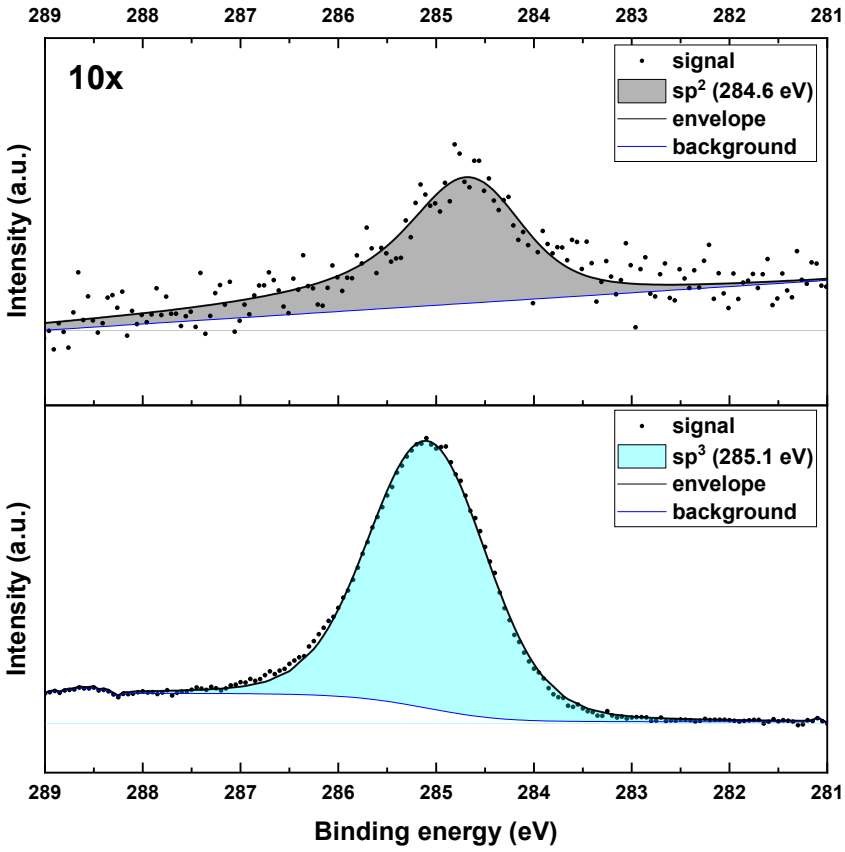

Figure 4.4: The lower panel shows the C1s signal of the as-loaded low-alloyed DIN 1.0338 steel fitted with a single component representing sp^3 surface carbon. The upper panel shows the C1s signal after annealing in hydrogen at ~750°C. The signal is shifted towards lower binding energy (284.6 eV) and best fitted with an asymmetric peak related to sp^2 hybridised carbon. The intensity scale in the upper panel is scaled up by a factor of 10, indicating that most of the initially present carbon was removed from the surface during the H_2 annealing.

As the steel is exposed to C_2H_2 gas, a distinct Fe-C component (283.2 eV) emerges that is ascribed to carbon bonded at iron surface sites.[60,163] As shown in the inset to Figure 4.5, this Fe-C component increases in intensity for about 5 min before remaining

constant for another 3 minutes. In Figure 4.6 the initial 4 scans after exposure are component fit to show the emergence of the Fe-C component in detail.

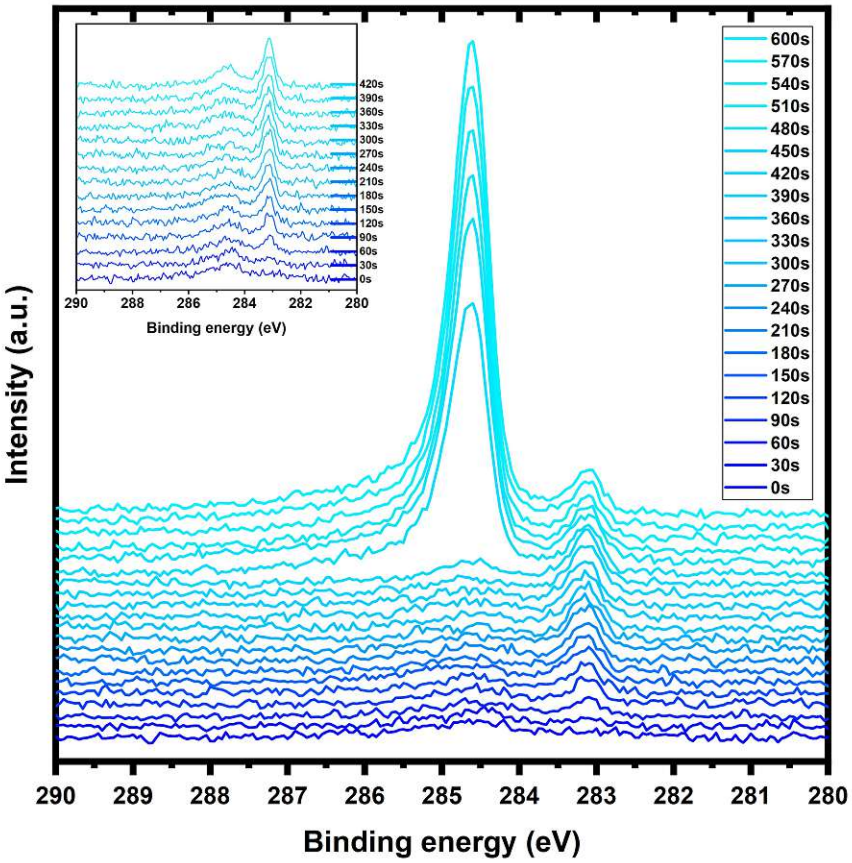

Figure 4.5: Time-resolved XPS C1s signal during in situ C_2H_2 exposure start showing emerging signal from Fe-C bonds (283.2eV) and rise of sp^2 graphene (284.7eV) after 420 seconds of exposure. The insert shows the first 7 minutes of exposure for better visibility of the Fe-C component evolution.

Subsequently, Figure 4.5 shows that rapid isothermal surface graphene growth starts with the surge of the graphene sp^2 C1s component at 284.6 eV component after 8 min of precursor exposure. This underscores our understanding that there is a period of carbon diffusion on the surface and into the subsurface of the steel before the necessary carbon saturation for isothermal surface graphene growth is reached. Upon C_2H_2 shut-off and leaving to cool in H_2 we also follow the C1s evolution in Figure 4.7 and observe further carbon precipitation from the steel (26 %), matching with multilayer regions in the optical image in Figure 4.3. This indicates that under our conditions precipitation of carbon from the steel is kinetically limited. The overall behaviour of this C1s evolution on the low-alloyed is thereby very similar to the graphene growth observed in chapter 3 for pure Fe.

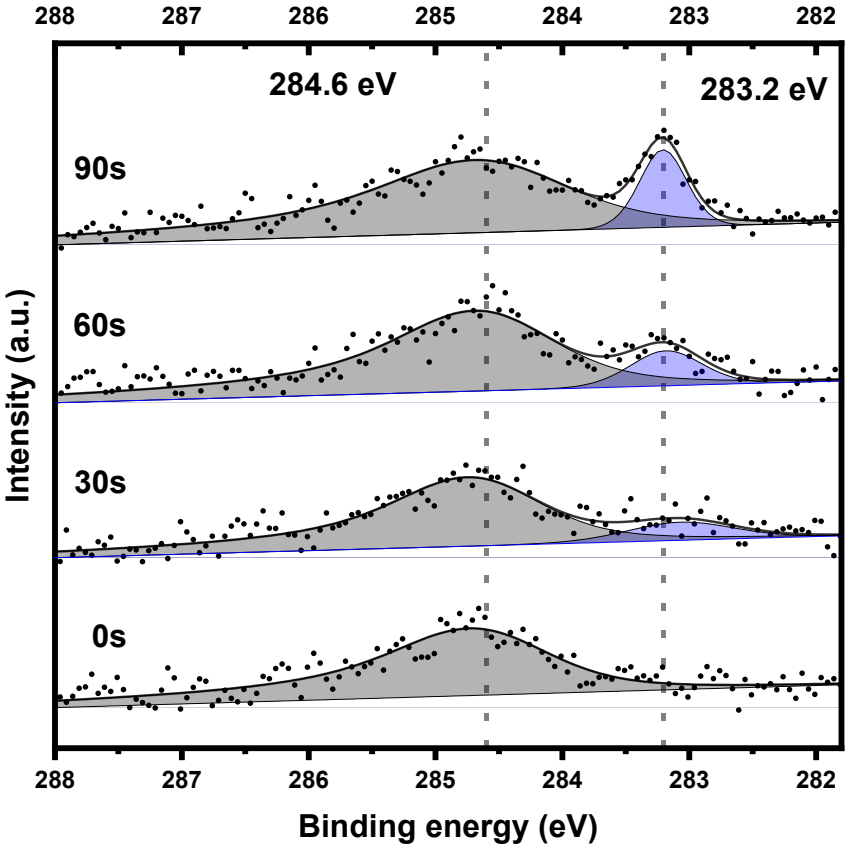

Figure 4.6: Time resolved detail spectra of the C1s region of the 1.0338 steel sample during C_2H_2 exposure at 750 °C. It shows the emergence of the Fe-C component (283.2 eV) in the beginning of the exposure sequence (exposure time in seconds indicated inside the graph on the left).

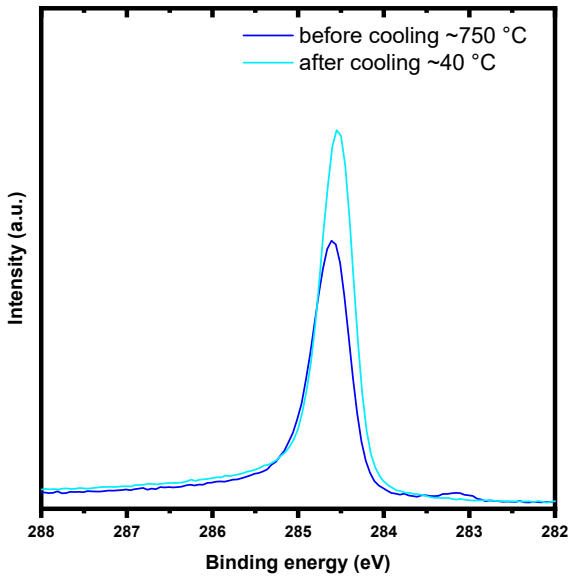

Figure 4.7: Time resolved detail spectra of the C1s region of the 1.0338 steel sample before and after cooling, showing the increase of the overall C1s signal by ~26 %.

4.3.2 Medium-alloyed high-carbon construction steel (DC01 1.0330).

Next we consider the medium-alloyed high-carbon construction steel (DC01 1.0330, steel composition in Table 4.1) as a good candidate towards more complex steels due to its increased carbon (0.12 weight-%) and (0.6 weight-%) Mn contents. Notably, the as received substrate surface of the medium-alloyed steel in Figure 4.1 differs from the low-carbon and stainless steel by displaying a significant amount of already initially present graphitic surface carbon (i.e. beyond the adsorbed adventitious carbon only noticeable in XPS), as evidenced by a pronounced G and D Raman peak for the as received medium-alloyed steel. Furthermore, the surface visually differs from the other steel grades by increased surface roughness.

When we apply our standard ex-situ CVD conditions to this medium-alloyed steel, we obtain only very poor growth results, as shown in Figure 4.8: Only amorphous carbon deposits characterised by wide and merging G and D peaks in Raman are predominantly found on the surface, with only very minor regions showing signs of graphitisation. Likewise, also, in-situ CVD in the NAP XPS results in only similarly poor amorphous carbon or, at best, nanocrystalline graphite growth, as shown in Figure 4.9.

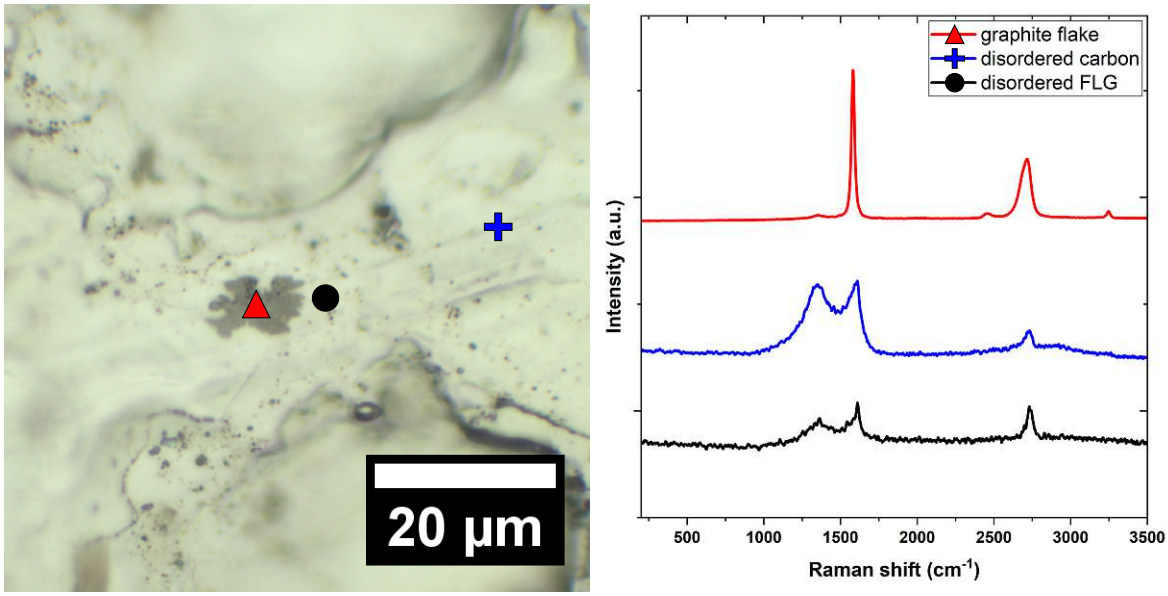

Figure 4.8: (left) Optical micrograph of medium alloyed high-carbon steel (1.0330) steel after standard ex situ CVD process at 750 °C. (right) Point localised Raman spectra corresponding to measurement locations in the optical image show an area of graphitic, highly ordered carbon, a region of disordered carbon and a region closer to the graphitic island showing slightly more ordered but defective few-layer graphene.

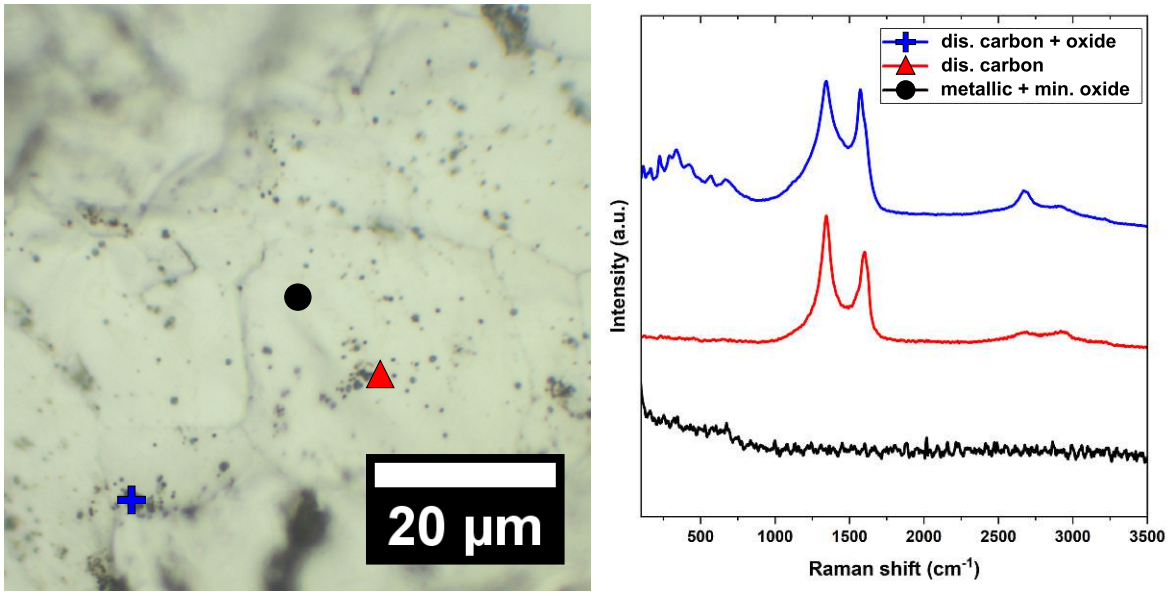

Figure 4.9: . (left) Optical micrograph of medium-alloyed, high-carbon steel (1.0330) steel after standard in situ XPS experimental run at 750 °C. (right) Point localised Raman spectra corresponding to measurement locations in the optical image showing an area of pristine metal with minimal surface oxidation, a region of disordered carbon closely matching the Raman signature of the as received sample and of disordered carbon with a complex oxide signature that can be related to oxide particles formed on the surface of the steel substrate.

We identify the initially present and persistent significant surface carbon (separate from usual adventitious carbon contamination) as the main obstacle for ordered graphene growth: In situ NAP XPS in Figure 4.10 shows that during H_2 annealing, in contrast to the low-carbon steel and pure iron (chapter 3), after the initial decrease in the C1s carbon signal, a significant amount of carbon remains in the form of graphitised sp^2 hybridised carbon (roughly 8-times more than in the case of the low-alloyed, low-carbon steel shown in Figure 4.4 above).

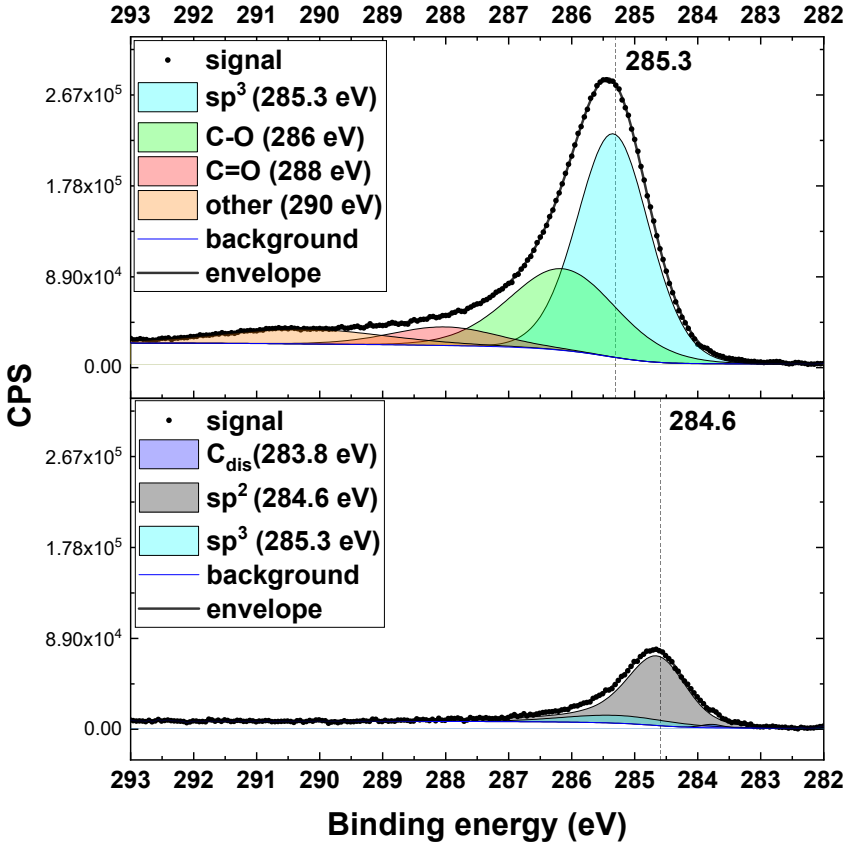

Figure 4.10: Carbon C1s XPS spectra of the steel (1.0330) surface before (upper panel) and after (lower panel) annealing in hydrogen at around 750 °C. The spectrum in the upper panel is indicative of mixed hydrocarbon contamination. The spectrum in the lower panel shows the change to almost exclusively sp^2 hybridised graphitic carbon upon hydrogen annealing. The component titled "other" is an interfering Auger signal.

We argue that this persistently present carbon prevents, during C_2H_2 exposure, further controlled high-quality graphene deposition via passivation of catalytic activity of the metal surface and/or also via inhibition of lateral expansion of nuclei to larger graphitic domains.[159] This is also experimentally observed whereby no noticeable isothermal surface growth arises even for prolonged C_2H_2 exposure times. Even after >50 min C_2H_2 exposure at 750 °C, no increase in the sp^2 peak is detected (correlating time-resolved XPS component fits are shown in Figure 4.11). Instead, we even find that the C1s sp^2 signal (284.6 eV) slightly diminishes with time of C_2H_2 exposure while we observe an emerging and increasing Fe-C component (283.3 eV). This shows that carbon diffuses between surface and sub-surface/bulk of steel, without nucleating further graphene. Our XPS data can, however, not resolve whether the carbon is arriving from the C_2H_2 exposure or liberated from the high-carbon steel's bulk. In either case, our data indicates that the initially present carbon inhibits graphene nucleation on the medium-alloy high-carbon steel.

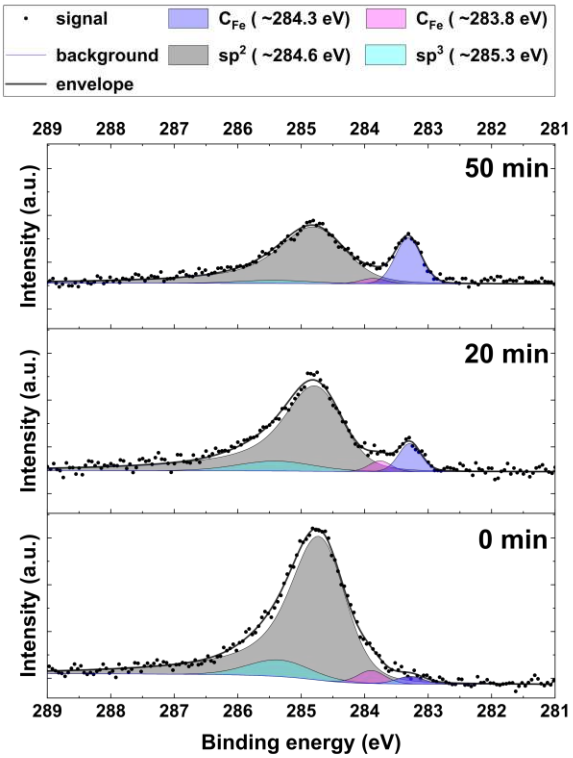

Figure 4.11: Time resolved XPS spectra of C1s region during in situ C_2H_2 exposure at around 750 °C for high-carbon (1.0330) steel. Exposure time is indicated on the right within each panel. The spectra show a gradual decrease in the main sp^2 carbon signal and a significant increase of the C_{Fe} component at ~283.3 eV after 50 min of hydrocarbon exposure.

Taking this finding into account, we then implement a novel strategy to facilitate surface graphene growth nevertheless. To eliminate the persistent sp^2 surface carbon contamination, we employ a deliberate pre-oxidation step with molecular oxygen gas (O_2 , 5×10^{-6} mbar) at elevated temperature inside the NAP XPS chamber. Figure 4.12 shows the gradual reduction of the C 1s intensity and the emergence of an intermediate C-O component, which recedes once most of the carbon has been removed. After the cleaning, the metal surface is reduced once more via H_2 annealing (~1 mbar) at a constant temperature. During this process, the Fe-C component noticeably increases while the sp^2 component signal remains constant, as shown in Figure 4.13. This shows that carbon is here coming from the bulk of the high-carbon steel (as C_2H_2 is not present during this step). This underscores that for CVD on steels not only the deliberate carbon feeding from the gas phase but also from the large carbon reservoir in the steel's bulk needs to be kept in mind.

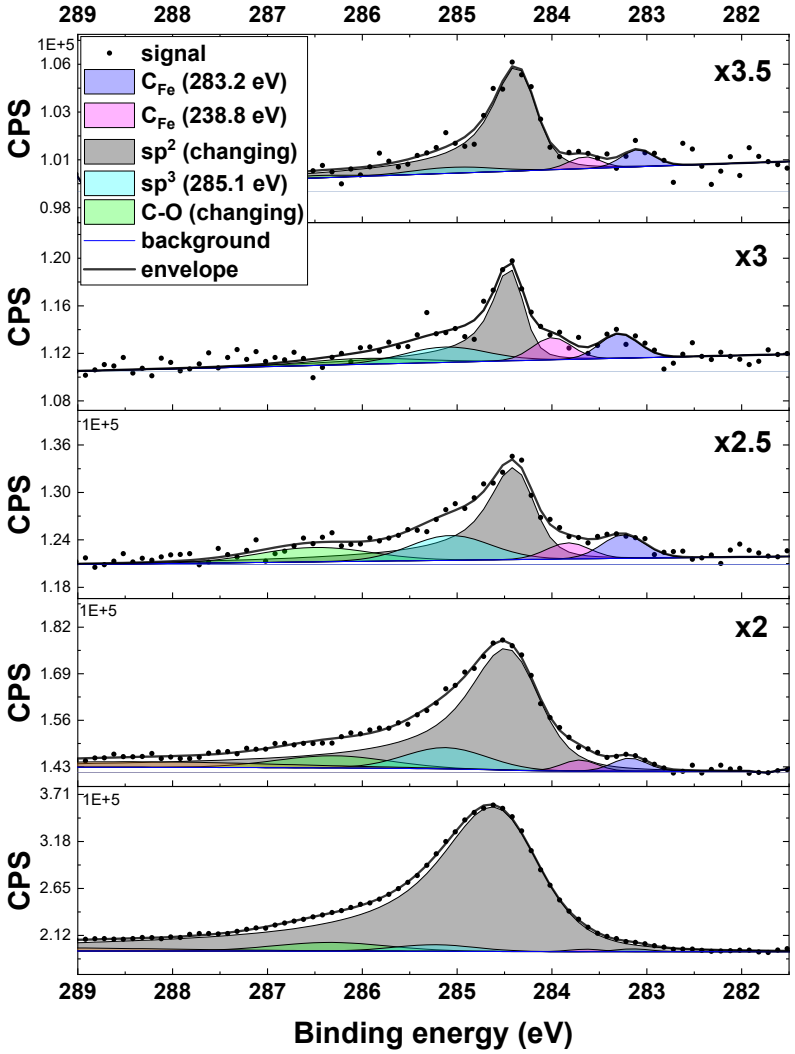

Figure 4.12: Time resolved in situ XPS of the C1s region during the pre-oxidation step in O_2 atmosphere at around 600 °C. Starting from the bottom, there is a clear reduction in the overall carbon signal and the initial increase in carbon-oxygen bonds. As the sp^3 component and the overall C 1s signal decrease, the intermediate carbon-oxygen components vanish, and a small sp^2 hybridized carbon signal remains. Y-axis magnification factors in relation to the bottom panel are indicated on the right in every panel.

The oxidation of the metal surface during the preceding oxygen-cleaning step produces a carbon-depleted surface oxide layer. The subsequent reduction of this oxide layer leaves a carbon-depleted metallic iron surface region. This region then absorbs carbon from the nearby carbon-rich steel by diffusion, resulting in lower than before surface carbon levels and the formation of a carbon-rich metal subsurface layer prior to precursor exposure.

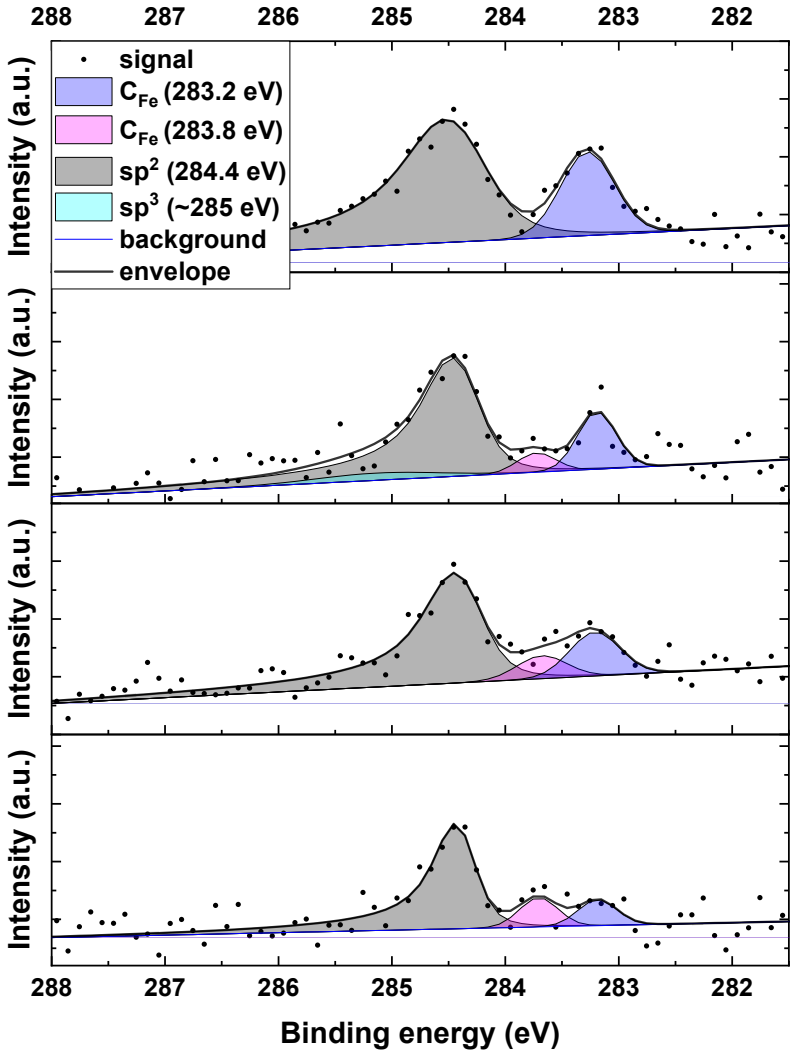

Figure 4.13: Time resolved in situ XPS of the C1s region during re-reduction step in H_2 atmosphere at around 700 °C. Starting from the bottom going up the sp^2 component remains somewhat stable while the C_{Fe} component noticeably increases.

Figure 4.14 follows the surface evolution when we introduce the C_2H_2 to the surface conditioned via the prior $H_2/O_2/H_2$ process. In stark contrast to the completely passivated sp^2 evolution for the standard conditions above (Figure 4.11), now after the $H_2/O_2/H_2$ process we observe an immediate sharp rise in the sp^2 C 1s component after only 20 s of C_2H_2 exposure. The sample is then exposed for a total of 30 min, before being left to cool down in H_2 atmosphere (akin as before).

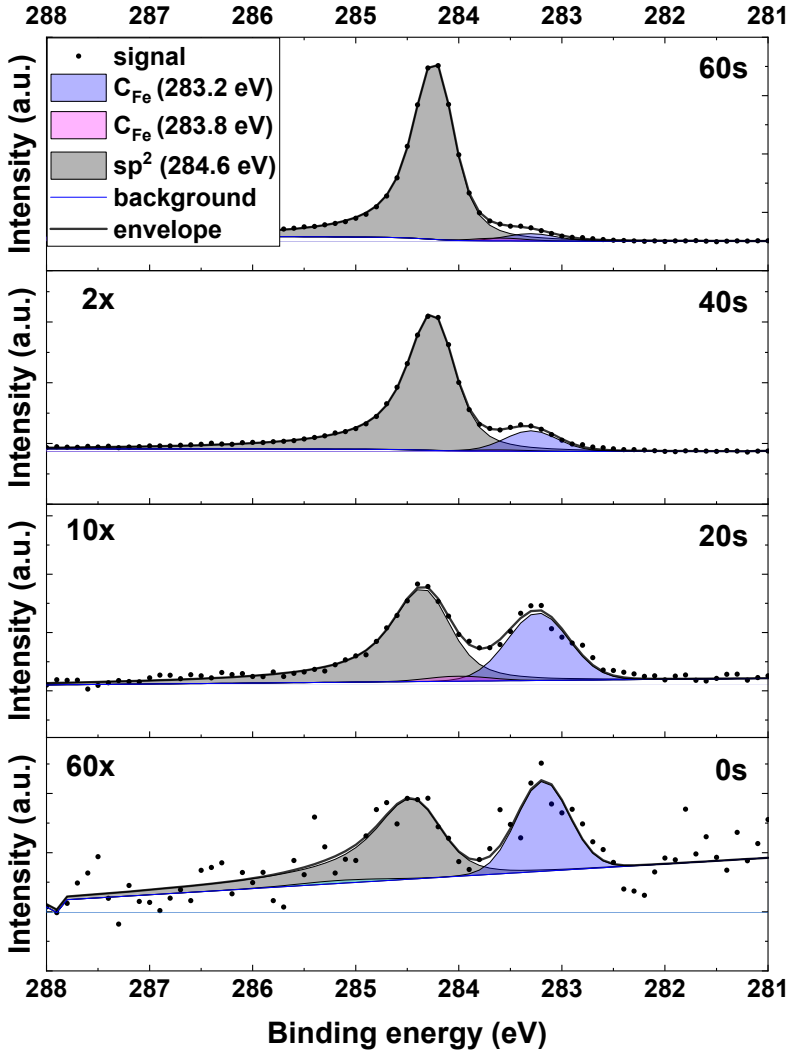

Figure 4.14: Time resolved in situ XPS of the C1s region during C_2H_2 exposure at around 750 °C. Exposure time in seconds is marked on the right side in each panel. Y-axis magnification factors in relation to the top panel is indicated on the left in every panel. The bottom panel shows the starting condition with two components (C_{Fe} at ~283.2 eV and sp^2 at 284.6 eV) after re-reduction in hydrogen. After 20s of exposure, the overall C 1s signal has already significantly increased, and the sp^2 component is starting to rise. The topmost panels show the steady rise of the sp^2 component during isothermal surface-mediated growth.

Optical microscopy and Raman spectroscopy in Figure 4.15 show the medium-alloyed surface covered in graphitic carbon/few-layer graphene with areas of varying thickness but generally good structural quality. This good quality few-layer graphene growth from our in-situ-guided $H_2/O_2/H_2$ process is a drastic improvement over the amorphous carbon growth obtained from the "standard" reference conditions in Figures 4.8 and 4.9. This data thereby clearly shows the usefulness of in situ characterisation of the graphene CVD process to optimise growth recipes.

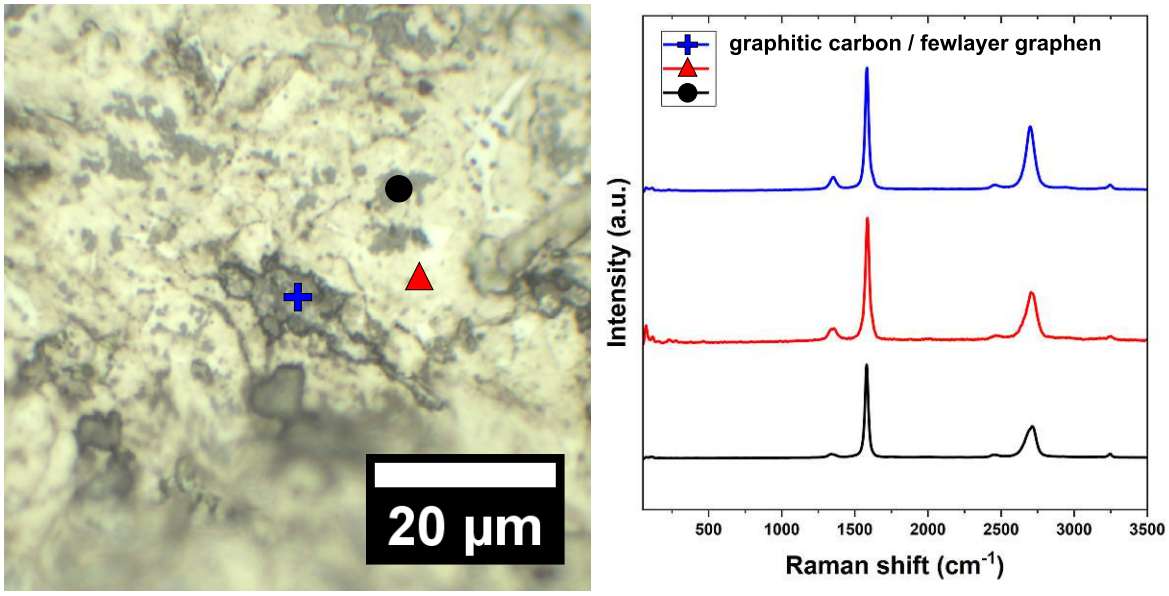

Figure 4.15: . (left) Optical micrograph of high-carbon (1.0330) steel after in situ XPS experimental run at around 750 °C with the pre-oxidation and re-reduction step. (right) Point localized Raman spectra corresponding to measurement locations in the optical image. All spectra show similar Raman signatures of highly ordered graphitic carbon with varying degrees of disorder and thickness.

4.3.3 High-alloy stainless steel (DN 1.4404)

The third archetypical steel investigated in this work is a high-alloy stainless steel with high Ni and Cr content (detailed steel composition in Table 4.1).

As shown in Figure 4.16 applying our standard ex situ CVD procedure results in extensive surface oxidation and visible disordered carbon agglomeration along substrate grain boundaries. Surface oxidation is also visually obvious from the vivid colours in the optical micrograph in Figure 4.16. Comparison with literature[167,168] helps identify a mix of chromium oxide (Cr_2O_3), iron oxide (Fe_2O_3) and spinel chromite ($FeCr^2O_4$) in the Raman spectrum. The formation of the oxides is ascribed to the only ~10^{-3} mbar base pressure of the ex-situ CVD system and the high propensity of Cr to form oxides. The Cr 2p region of ex-situ measured XPS also matches a mix of chromite and chromium oxide and can be readily fitted following previous work from Biesinger et. al.[169], which is shown in Figure 4.17.

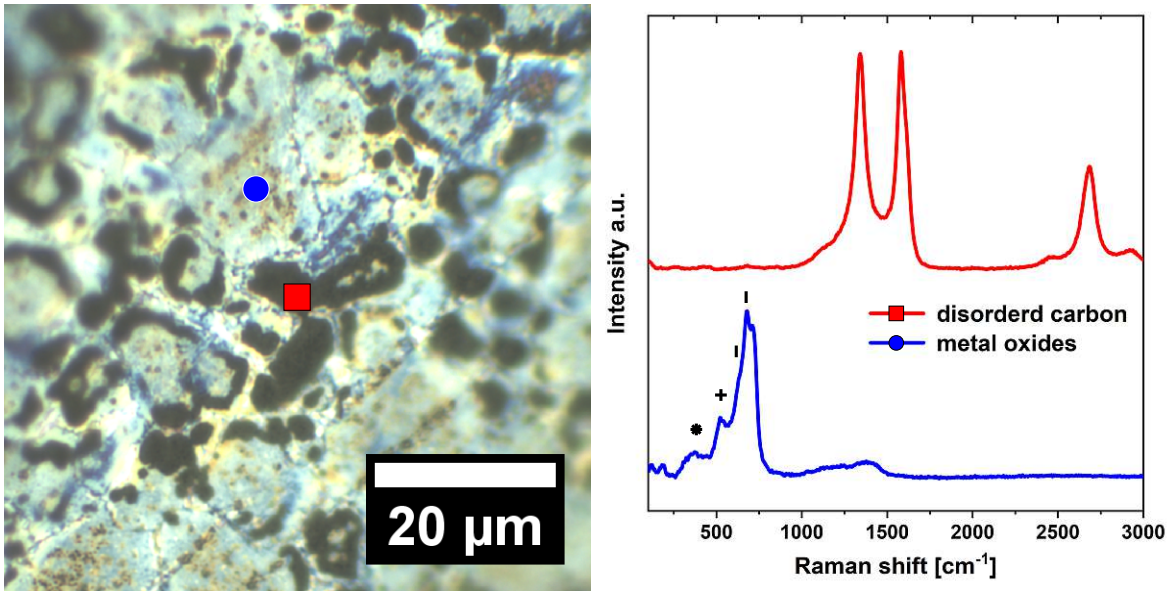

Figure 4.16: (left) Optical microscopy image of stainless steel surface after CVD graphene growth attempt. (right) Point localised Raman spectra of points indicated in optical microscopy image, showing disordered carbon and metal oxide signatures respectively. Metal oxide peaks are marked for identification: (|) chromite, (+) chromium oxide, (*) mixed peaks.

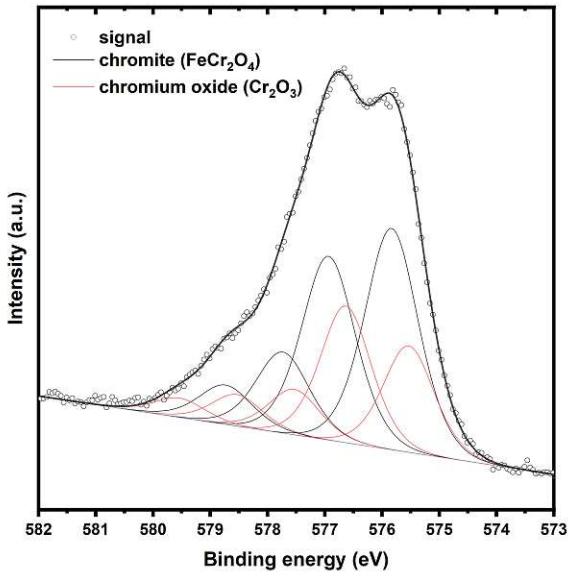

Figure 4.17: Ex situ XPS of the Cr 2p region of stainless steel (1.4404) after standard lab CVD process (Raman and optical analysis shown in Figure 4.16). Component fit of detail spectrum, considering mulitplet splitting, reveals both chromium oxide (Cr_2O_3) and iron chromite ($FeCr_2O_4$).

We refrain from fitting the more complex iron- and manganese oxide signatures also detected and shown in Figure 4.18. The carbon deposit obtained from the ex-situ CVD conditions is only in the form of patchy nanocrystalline graphite. Such poor growth on Cr-containing stainless steels was previously attributed to the persistence of the

Cr-oxides hindering graphene nucleation.[110]

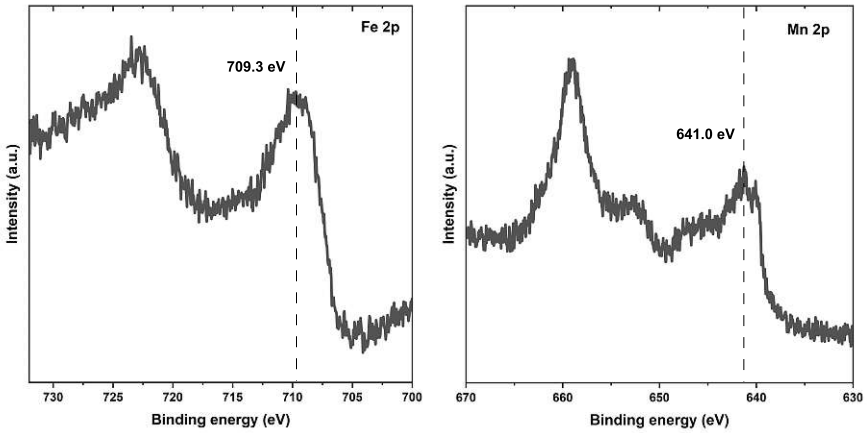

Figure 4.18: Ex-situ XPS of the Fe 2p and Mn 2p region of stainless steel (1.4404) after standard lab CVD process (Raman and optical analysis shown in Figure 4.16). Peak positions indicate both iron- (709.3 eV) and manganese (641.0 eV) surface oxides.

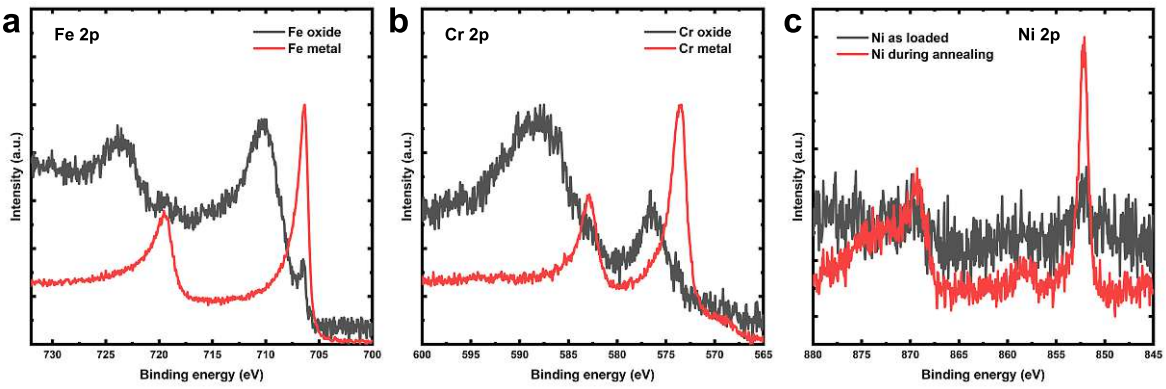

Figure 4.19: In-situ XPS of stainless steel surface as-received (grey) and during hydrogen annealing (red) shows complete reduction of both (a) iron- and (b) chromium oxides towards pure metal XPS signatures. Additionally, the Ni 2p region (c) shows the emergence of a metallic nickel signature.

To understand the high propensity for Cr-oxide formation and its impact on the graphene growth on stainless steel further, we also follow the CVD process in situ by NAP XPS. Interestingly, Figure 4.19(a,b) shows a full reduction of both chromium- and iron surface oxides upon low pressure H_2 annealing at around 750 °C. We note however that the in-situ NAP XPS system has a much lower base pressure of ~10^{-8} mbar compared to the ex situ CVD conditions (~10^{-3} mbar). Additionally, a noticeable increase in Ni XPS signal indicating a migration of Ni from the stainless steel to the surface can be seen in Figure 4.19(c). During the following C_2H_2 exposure in Figure 4.20 the characteristic primary rise of a carbon-metal component (~283.2 ± 0.1 eV) is detected followed by a rapid increase in surface carbon signal (~284.6 ± 0.1 eV), demonstrating the isothermal

surface growth of sp^2 hybridised carbon.

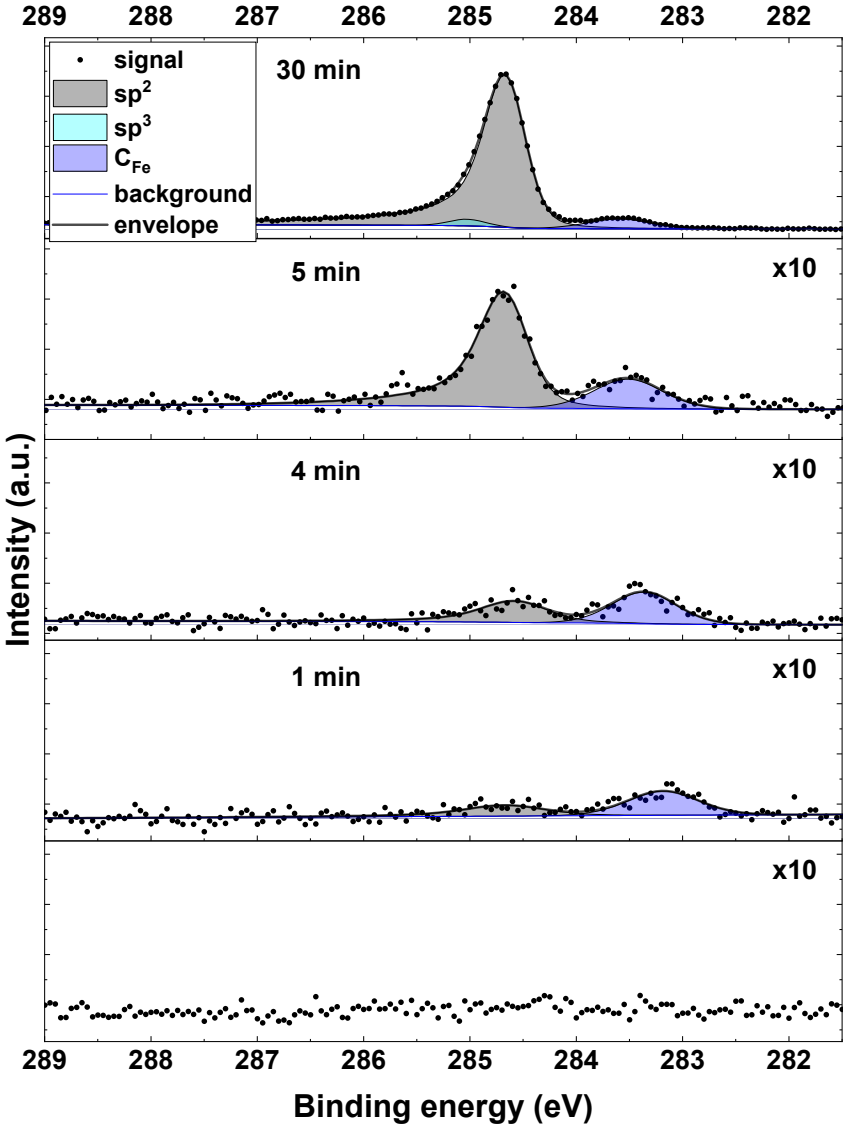

Figure 4.20: Time resolved in situ XPS of the C1s region during C_2H_2 exposure at around 750 °C. Exposure time in seconds is marked on the right side in each panel. Y-axis magnification factors in relation to the top panel is indicated on the right in every panel. The bottom panel shows the starting condition with no carbon signal. After 1 min of C_2H_2 exposure the C_{Fe} component (283.2 eV) and a minimal sp^2 component (284.6 eV) emerge. After 30 min of exposure, the overall C1s signal has significantly increased, and the sp^2 component is dominant.

The C1s signal continues to increase significantly (3.5 times increase in C1s signal) also during cooling of the substrate after C_2H_2 exposure as shown in Figure 4.21, indicating substantial precipitation of dissolved carbon to the substrate surface. We attribute this to the fcc structure of the stainless steel, which exhibits a large carbon solubility.

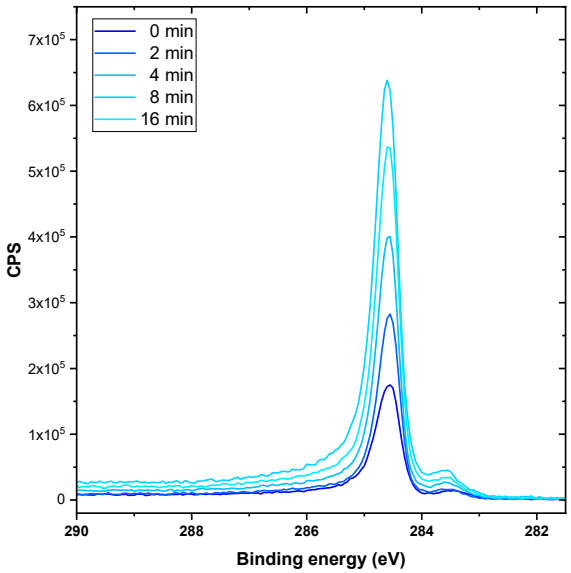

Figure 4.21: Time resolved in-situ XPS signal showing the increase of the C 1s component during cooling after C_2H_2 exposure in hydrogen environment, showing significant carbon precipitation.

Optical microscopy and Raman on this in situ CVD run in Figure 4.22 shows a largely continuous, thin film of carbon with limited inconsistencies, that visually appear as slightly brighter regions. The respective point localised Raman spectrum shows a very sharp D-peak and high-intensity 2D-peak, which matches a nano-crystalline graphite coating. The intensity ratio ($I_{2D}/I_G > 1$) and 2D peak fit (single Lorentzian, FWHM of ~51 cm^{-1}) are evidence of the turbostratic nature of the graphite layers.[170] Raman spectra of the uncoated region show no features, in line with a bare metal substrate. Thereby the in-situ NAP XPS data has shown that improvements upon the very poor ex-situ growth results of patchy nanocrystalline graphite in Figure 4.16 can be obtained by better base pressure conditions. We argue that these better base pressure conditions lead to a full reduction of all metallic surface species, thus facilitating better homogeneous carbon film growth. Additional work on kinetic conditions to allow more controlled carbon deposition towards thinner and better crystallised graphene layers remains however necessary for the highly-alloyed stainless steel substrates.

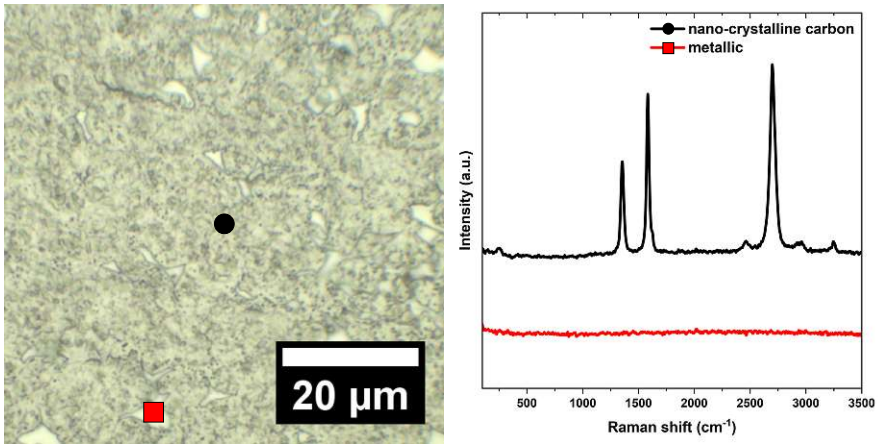

Figure 4.22: (left panel) Optical micrograph of stainless steel (1.4404) surface after in situ XPS CVD process. (right panel) Point localized Raman spectra of corresponding to measurement locations in (left panel), showing nano-crystalline turbostratic carbon and bare metal substrate signatures.

4.4 Conclusions

The differences in graphene CVD between three archetypical steel substrates have been shown via detailed ex-situ growth and in situ NAP XPS experiments. For low-alloyed, low-carbon (1.0338) steel, large-scale graphene growth was achieved. For medium alloyed, high-carbon (1.0330) steel, unfavourable surface conditions were improved via an in situ-guided pre-oxidation step of the substrate surface leading to a previously unattainable graphitic carbon coating. The high-alloyed stainless steel (1.4404) is highly sensitive to background oxygen due to its alloying elements, leading to pronounced surface oxidation of Fe, Cr and Mn under scalable ex-situ CVD conditions. We show that via better base pressure in our in situ CVD conditions, the native surface oxides, including Cr-oxides are readily reduced, allowing isothermal surface growth of a nanocrystalline graphite film using our standard approach.

We have identified key challenges for graphene growth on these complex steel substrates, such as the need for well-defined substrate surface conditions and an oxygen-free, reductive growth environment for high-alloy steels. This forms a guiding framework for future work on the optimisation of graphene growth on metallurgical alloys, incl. steels.

4.5 Publication Notice

This chapter is being prepared for publication and is listed as number 4 in the publication list.

Bibliography

57. Choi, S. H. *et al.* Large-scale synthesis of graphene and other 2D materials towards industrialization. *Nature Communications* **13.** Publisher: Nature Publishing Group, 1484. ISSN: 2041-1723. doi:10.1038/s41467-022-29182-y (2022).

60. Weatherup, R. S. *et al.* On the Mechanisms of Ni-Catalysed Graphene Chemical Vapour Deposition. *ChemPhysChem* **13,** 2544–2549. ISSN: 1439-7641. doi:10.1002/cphc.201101020 (2012).

70. You, Y. *et al.* A Controlled Carburization Process to Obtain Graphene–Fe3C–Fe Composites. *Advanced Materials Interfaces* **5,** 1–7. ISSN: 21967350. doi:10.1002/admi.201800599 (2018).

72. Vinogradov, N. A. *et al.* Formation and structure of graphene waves on Fe(110). *Physical Review Letters* **109,** 1–5. ISSN: 00319007. doi:10.1103/PhysRevLett.109.026101 (2012).

73. An, H., Lee, W. J. & Jung, J. Graphene synthesis on Fe foil using thermal CVD. *Current Applied Physics* **11.** Publisher: Elsevier B.V, S81–S85. ISSN: 15671739. doi:10.1016/j.cap.2011.03.077 (2011).

75. Lavin-Lopez, M. P., Fernandez-Diaz, M., Sanchez-Silva, L., Valverde, J. L. & Romero, A. Improving the growth of monolayer CVD-graphene over polycrystalline iron sheets. *New Journal of Chemistry* **41.** Publisher: Royal Society of Chemistry, 5066–5074. ISSN: 13699261. doi:10.1039/c7nj00281e (2017).

107. Tawfik, H., Hung, Y. & Mahajan, D. Metal bipolar plates for PEM fuel cell—A review. *Journal of Power Sources* **163,** 755–767. ISSN: 03787753. doi:10.1016/j.jpowsour.2006.09.088 (2007).

108. Xu, Z., Qiu, D., Yi, P., Peng, L. & Lai, X. Towards mass applications: A review on the challenges and developments in metallic bipolar plates for PEMFC. *Progress in Natural Science: Materials International* **30,** 815–824. ISSN: 10020071. doi:10.1016/j.pnsc.2020.10.015 (2020).

109. Wu, S. *et al.* A review of modified metal bipolar plates for proton exchange membrane fuel cells. *International Journal of Hydrogen Energy* **46,** 8672–8701. ISSN: 0360-3199. doi:10.1016/j.ijhydene.2020.12.074 (2021).

110. John, R., Ashokreddy, A., Vijayan, C. & Pradeep, T. Single-and few-layer graphene growth on stainless steel substrates by direct thermal chemical vapor deposition. *Nanotechnology* **22.** ISSN: 09574484. doi:10.1088/0957-4484/22/16/165701 (2011).

137. Romani, E. C. *et al.* Graphene Grown by Chemical Vapour Deposition on Steel Substrates: Friction Behaviour. *Tribology Letters* **65.** Publisher: Springer US. ISSN: 15732711. doi:10.1007/s11249-017-0879-8 (2017).

159. Weatherup, R. S. *et al.* Introducing carbon diffusion barriers for uniform, high-quality graphene growth from solid sources. *Nano Letters* **13,** 4624–4631. ISSN: 15306984. doi:10.1021/nl401601x (2013).

163. Bleu, Y. *et al.* Dynamics of carbon diffusion and segregation through nickel catalyst, investigated by in-situ XPS, during the growth of nitrogen-doped graphene. *Carbon* **155,** 410–420. ISSN: 0008-6223. doi:10.1016/j.carbon.2019.08.084 (2019).

164. Ghaemi, F., Abdullah, L. C., Tahir, P. M. & Yunus, R. Synthesis of Different Layers of Graphene on Stainless Steel Using the CVD Method. *Nanoscale Research Letters* **11,** 506. ISSN: 1556-276X. doi:10.1186/s11671-016-1709-x (2016).

165. Singh, S. *et al.* Tribological Performance of Steel With Multi-Layer Graphene Grown by Low-Pressure Chemical Vapor Deposition. *Journal of Tribology* **142.** ISSN: 0742-4787. doi:10.1115/1.4047458 (2020).

166. Kidambi, P. R. *et al.* The parameter space of graphene chemical vapor deposition on polycrystalline Cu. *Journal of Physical Chemistry C* **116,** 22492–22501. ISSN: 19327447. doi:10.1021/jp303597m (2012).

167. Farrow, R. L., Benner, R. E., Nagelberg, A. S. & Mattern, P. L. Characterization of surface oxides by Raman spectroscopy. *Thin Solid Films* **73,** 353–358. ISSN: 0040-6090. doi:10.1016/0040-6090(80)90499-X (1980).

168. Fan, C., Shi, J., Sharafeev, A., Lemmens, P. & Dilger, K. Optical spectroscopic and electrochemical characterization of oxide films on a ferritic stainless steel. *Materials and Corrosion* **71.** _eprint: https://onlinelibrary.wiley.com/doi/pdf/10.1002/maco.201911425, 440–450. ISSN: 1521-4176. doi:10.1002/maco.201911425 (2020).

169. Biesinger, M. C. *et al.* Resolving surface chemical states in XPS analysis of first row transition metals, oxides and hydroxides: Cr, Mn, Fe, Co and Ni. *Applied Surface Science* **257,** 2717–2730. ISSN: 0169-4332. doi:10.1016/j.apsusc.2010.10.051 (2011).

170. Malard, L. M., Pimenta, M. A., Dresselhaus, G. & Dresselhaus, M. S. Raman spectroscopy in graphene. *Physics Reports* **473.** Publisher: Elsevier B.V., 51–87. ISSN: 03701573. doi:10.1016/j.physrep.2009.02.003 (2009).

CHAPTER 5

Controllable Freezing Transparency for Water Ice on Scalable Graphene Films on Copper

5.1 Introduction

Environmental ice formation from the freezing of water on materials can critically impact their operational performance, safety and running cost in many application fields.[171] For instance, ice build-up can result in structural vulnerability in large metallic structures such as overhead power line cables made from uncoated steel/Cu/Al threading, degraded energy efficiency in appliances by blocking of metallic heat exchangers in, e.g., refrigerators, or functional failure in control and lift surfaces in aerospace structures. Therefore, solutions to control ice nucleation on materials are highly sought after.[171]

To date, the control of ice formation is often an active process where materials are either heated, sprayed with anti-icing chemicals or mechanically de-iced.[171] These measures always come at a cost of energy and time, which is why a great deal of research is currently focused on creating surface treatments or extraneous coatings with the ability to passively control ice nucleation.[171] In this context, the desired passive control of ice nucleation, on the one hand, often includes "anti-icing" capabilities, i.e. lowering the temperature of ice formation on a given surface below its operation conditions. On the other hand, sometimes however also controlled "icing" at pre-determined, operationally safe locations can be desired.

The formation of ice on a material is, however, a highly multifaceted and, as of yet, not sufficiently understood process. For heterogeneous ice nucleation it is intricately linked with a material's surface energies, nano-morphologies and wettabilities.[171] Most current solutions to passive "anti-icing" surfaces include fabrication of nm/µm hierarchically structured superhydrophobic surfaces incl., e.g., slippery liquid infused porous surfaces (SLIPS).[171] Such surfaces are however hard to produce at scale, prone to damage by wear and can under certain conditions even detrimentally increase ice nucleation (e.g., droplet impingement vs. water condensation "frosting").[171] Therefore new materials/surfaces/coatings that can control ice build-up remain highly sought after. Likewise, insights into the mechanistic processes of water freezing, heterogeneous ice nucleation and ice growth and how they are linked to given surface properties are still highly desired.

A multi-functional class of novel materials that has been under intense investigation over the past years are atomically-thin, two-dimensional (2D) materials such as graphene, a monolayer of sp^2-bonded carbon. In particular, the peculiar liquid water wetting behaviour on graphene incl. existence of a highly debated "wetting transparency" of graphene, coated onto metals, has recently been extensively studied and discussed.[172–179] Wetting transparency is defined as the case when the presence of graphene does not change a surface's wetting behaviour (mostly measured via contact angle) compared to the bare underlying support.[172–179] The occurrence of wetting transparency is commonly attributed to the atomic thinness of monolayer graphene, whereby the surface properties of the underlying substrate are transmitted through the, in comparison, chemically inert graphene monolayer. Consequently, the surface properties are still determined by the substrate, despite the presence of graphene.[172–183]

Despite this huge interest in graphene wetting, astonishingly practically no experimental work has been done to date on water freezing and ice nucleation on scalable graphene films on metals.[184–186] This is even more so a curious gap in literature since a sizeable number of computational studies have used graphene layers as model systems for computational ice nucleation investigation.[187–192] The lack of experimental work on ice nucleation on graphene films is furthermore surprising, since atmospheric soot composed of 2D nanocarbons, which are in first approximation nanoscopic graphene fragments, are well-known nuclei for heterogeneous atmospheric ice formation, with strong (and often conflictingly observed) dependencies of ice nucleation properties on the soot's/nanographene fragments' defect levels/chemical functionalizations.[193–202]

In turn, from an application perspective, the related question arises if (functionalised)

graphene on metals could be advantageously utilized to control the heterogeneous ice nucleation behaviour on metal surfaces? Such use of graphene would have high application relevance: Industrially scalable chemical vapour deposition (CVD) of graphene on a large variety of metals has been developed[104] and thus CVD graphene as a potential ice-control coating platform could be scalably employed on a range of application-wise important metals.

Despite this, the fundamental water freezing and ice nucleation properties of scalable graphene films have not been experimentally assessed yet and investigation of the exciting potentiality of scalable CVD graphene on technologically important metals as an ice nucleation control coating also remains underexplored.

Only two prior reports investigated changes in ice nucleation from graphene coatings, albeit both grown under non-scalable ultra-high-vacuum (UHV) conditions and not on a scalable metal, but on prohibitively expensive Ru/sapphire and Ir/sapphire single-crystal models.[184,185] From the literature on graphene's wetting transparency it is well known that there exists a key substrate-dependence on graphene's wetting properties.[176,195] This suggests that ice nucleation studies conducted on UHV single-crystal models may have limited applicability when it comes to making predictions about graphene-covered metal surfaces at a scalable level.

Towards filling these critical gaps in the literature, both in terms of experimental study of fundamentals of water ice nucleation on graphene as well as assessing scalable (functionalized) graphene as a potentially ice-control coating, we investigate the water freezing behaviour on scalably grown CVD graphene on application-relevant polycrystalline Cu. The employed Cu supports are hereby not only the most widely used support to produce CVD graphene[61,104] but Cu is also a highly important metal with respect to desired ice control due to Cu's widespread use in, for example, overland power line threads or appliance heat exchangers.

We show in this work that non-treated, as-grown CVD graphene on Cu can be (as we term it) "freezing transparent" i.e. the graphene's presence does not change the freezing temperature curves of water to ice on Cu in our measurements. Such "freezing transparency" has to date not been reported, and thus also not been considered in the many computational studies that used graphene as a model system for ice nucleation surfaces. Furthermore, we investigate how functionalisations to the CVD graphene (incl. oxygen-containing, -F and -polymethylmethacrylat (-PMMA) funcionalisations

via plasma and liquid phase treatments) can result in controllable changes of water freezing curves to lower/higher temperatures and how the freezing transparency can be lifted. We also explore extrinsic factors necessary for the observation of this freezing transparency, such as the storage time of our samples in ambient conditions and linked adventitious hydrocarbon adsorption levels. This work thereby not only introduces the concept of freezing transparency of graphene on a metal based on first experimental observation, but also introduces scalable CVD graphene as an ultimately thin platform towards control of ice nucleation on a technologically relevant metal.

5.2 Methods

5.2.1 Graphene CVD

We employed 25 µm thick Cu foils (Alfa Aesar Puratonic® 99.999 %) as catalysts for graphene CVD in a custom-made hot wall tube furnace at reduced pressure (base pressure 10-3 mbar), based on a prior reported CVD recipe.[147] The Cu foils were first pre-treated at 960 °C in 2000 sccm flow of Ar with 5% H_2 resulting in ~14 mbar pressure in order to facilitate Cu crystal domain growth and reduction of Cu-oxides from foil storage in ambient air. For graphene growth 50 sccm CH_4 were added for 7 min, increasing the total pressure to ~15 mbar. After growth, the Cu foils were left to cool in AR/H_2 atmosphere by sliding the tube furnace's hot zone from the samples. This recipe results in a closed film of high-quality graphene on Cu.[147] Graphene-free reference Cu samples with the same Cu grain structure were prepared using the same processing with the exception of the CH_4 exposure step.

5.2.2 Functionalisation treatments

Air plasma. Samples were air plasma treated in a commercial plasma chamber (Atto from Diener Electronic GmbH & Co KG, Germany). A plasma (at 50 % power level of 40 kHz 0-200 W; 13.56 MHz 0-300 W) was struck in ~0.5 mbar air with exposure of the samples to the air plasma for 2 s.

SF_6 plasma. For SF_6plasma treatment a PlasmaPro 100 Cobra (OXFORD Instruments) system was used with a pressure of ~0.05 mbar, a SF_6 gas flux of 40 sccm and a bias of 21 V with RF = 18 W.

PMMA. PMMA functionalisation of graphene/Cu and annealed Cu samples was done by drop casting PMMA photoresist (200K, AR-P 642.04, Allresist GmbH, Germany) onto the foil samples and curing the PMMA on a hotplate at 100°C in air. Samples were subsequently put into acetone for 2 h and rinsed with DI water and isopropanol to remove the PMMA film, which is however known to be an imperfect process, resulting in persistent decoration of the graphene with PMMA micro- and nanoparticles.[203] Samples were stored in ambient air.

5.2.3 Materials Characterisation

Optical Microscopy and Raman Spectroscopy.[149,204] Optical microscopy and Raman spectroscopy were conducted using a WITec alpha 300 RSA+ system with laser wavelength 488 nm, laser power 10 mW and spot size ~2 µm and in a NT MDT Ntegra Spectra system with laser wavelength of 473 nm.

XPS. X-ray photoelectron spectroscopy (XPS) measurements were performed with a Specs XR50© high-intensity non-monochromatic Al/Mg dual anode and an X-ray source Phoibos 100 energy analyzer (EA) with a multichannel plate. The spectra were obtained at room temperature, an emission angle of 0°, a pass energy of 20 eV and using an Al anode with K_α radiation at 1486.6 eV. Data analysis was performed via CasaXPS. Calibration of the spectra was deemed unnecessary, as due to the high conductivity of the copper foils minimal sample charging was anticipated. All spectra were analyzed with an energy step width of 0.1 eV, though only every third data point is shown in the figures for improved clarity.

5.2.4 Ice nucleation measurements

Samples were measures ~24 h after the last process step unless otherwise stated. Samples were sprayed with MiliQ (18.2 MΩ·cm) water by hand, using a spray bottle and fine nozzle creating a mist of fine droplets. This results in reproducible droplet sizes and densities on the samples overall (example in first frame in Figure 5.1b). Ice nucleation measurements[205] on these various samples were performed in an optical cryo-microscopy setup (schematic in Figure 5.1a),[206] consisting of a cryo-cell containing a Peltier element (Quick-cool QC-31-1.4-3.7M) that can cool down to –40 °C through thermoelectric cooling and is temperature controlled via feedback from a K-type thermocouple mounted directly on the sample stage. The cryo-cell has a glass window and is mounted directly on an optical light microscope stage so that the freezing of individual water droplets can be observed as a function of temperature in the optical microscope. The freezing

stage is housed inside an air-tight cell at atmospheric pressure, which was purged with dry N_2 gas before ice nucleation measurements. This results in a low humidity atmosphere inside the chamber and thus suppresses secondary water droplet formation from condensation during cooling runs.[206]. The Cu foil backside was contacted to the stage with a small amount of paraffin oil to ensure optimal thermal contact between the Peltier stage and Cu samples.

During the freezing experiments, the Peltier element is cooled at a steady rate of 10 K/min. Concurrently, optical microscope images of the water droplets are recorded at a rate of 20 images/s during cooling incl. a temperature stamp in each recorded image. The freezing of an individual droplet can readily be detected in the optical microscope image sequences by a change in optical appearance whereby the water droplet changes contrast upon freezing (Figure 5.1b). The freezing event of a given water droplet is therefore here assigned to this change in optical appearance of a given water droplet, in line with prior literature.[184,207] We note that freezing of small water droplets is a fast process occurring over a timescale of fractions of a second.[207] Since our cooling rate of 10 K/min is on a much slower timescale, we can assign the temperature at which this freezing event is observed as the freezing temperature of this given water droplet. An exemplary freezing series, incl. temperature stamps, is shown in Figure 5.1b. As the contrast change upon freezing can be quite subtle, a freezing event can be further accentuated by employing image difference calculations (Figure 5.1c).

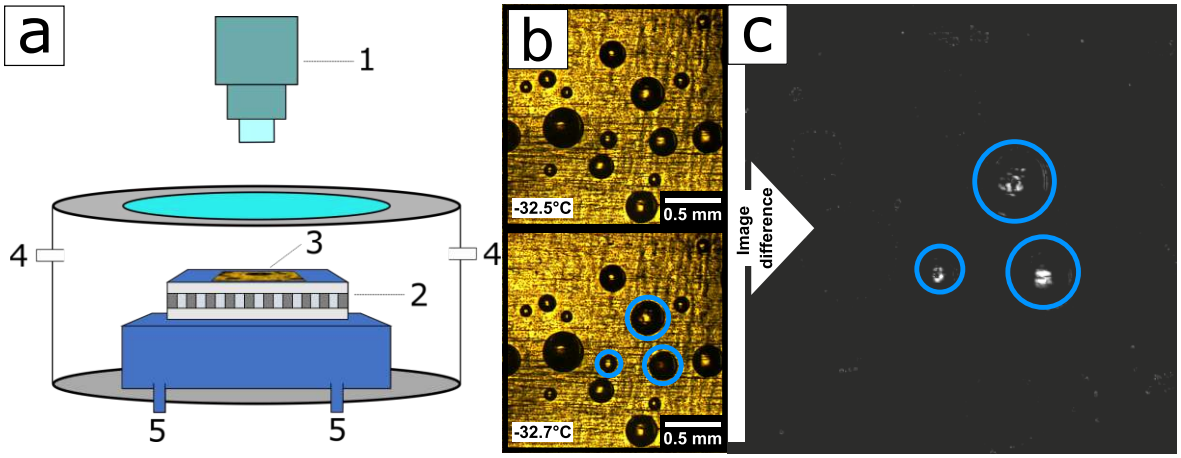

Figure 5.1: **(a)** Schematic illustration of cryo-microscopy setup (1: microscope objective, 2: Peltier cooling element, 3: copper foil sample, 4: in-/outlet for N_2 purging, 5: in-/outlet water-cooling). **(b)** Optical micrograph series, incl. temperature-stamps, depicting sample region before (upper frame) and after multiple exemplary freezing events of the marked (blue circles) water droplets. **(c)** Image difference calculations based on the data presented in **(b)** accentuating the freezing event of the marked water droplets for easier detection.

5.2.5 Freezing Data Processing

Freezing experiments were recorded as video (20 fps) with temperature- and time stamps and separate temperature log files. Temperature was recorded in ~0.15 K steps, which is, therefore, the limit for temperature resolution in our measurements. The video was then analysed, either manually with the help of image processing software (ImageJ/Fiji[208,209]) by converting the video to an image stack and running an image difference operation ("stack difference") before going through the stack frame by frame to extract individual freezing events, or with the help of an automated Python script. The algorithm, in the first step, extracts the drop location and size (diameter) from the first frame of the video. As the drops appear much darker than the copper background, only simple image processing is needed to extract this information. First, the image is converted to greyscale, blurred slightly to remove any contrast from the texture of the copper sheet and a threshold is applied to convert the image to a binary black-white image. In this state, only the drops should appear as black blobs while the copper sheet should be mostly white. To further isolate the drops, a morphological erosion operation is performed and the connected black regions that are large enough (in the number of pixels) are retained and assigned a label. From this the diameter and position is computed, assuming spherical drops and a region of interest (ROI) is drawn for each drop.

At this point, the user gets to check if the drop assignment was done correctly before the freezing event detection resumes. To detect freezing events the algorithm analyses the change in brightness between 2 subsequent frames. If inside one ROI, which was computed as previously described, a large enough absolute change in brightness occurs, this is detected as a freezing event. Together with the temperature log file, the freezing temperature for individual freezing events is recorded. The output is then manually checked for irregular or double detection of freezing events as contrast change upon freezing may happen over a time span of more than one frame. This raw data in form of droplet freezing events was then converted to freezing fraction curves (0 % to 100 %) and interpolated between 0.1 K temperature steps with the condition that the freezing fraction is considered constant between freezing events. This results in freezing fraction curves that show a stepwise increase in the fraction of frozen droplets with decreasing temperature.

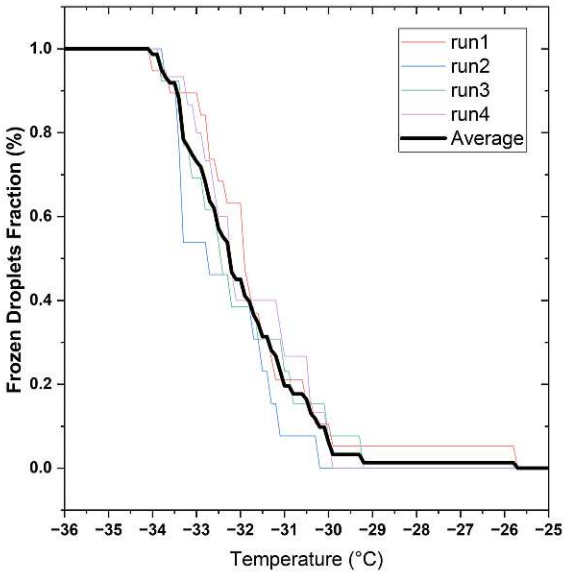

Figure 5.2: Visual depiction of our method of freezing curve average calculation exemplary for the dataset for graphene/Cu SF_6 plasma treated samples. For all four freezing curves (thin, faint curves), we average the frozen fraction value for each temperature value, resulting in our freezing curve average (thick, black curve). Individual freezing curves are calculated by interpolating between single droplet freezing events with a temperature step of 0.1 K. The freezing fraction is considered constant between freezing events in order to more accurately depict the actual measured datapoints, which leads to the stepwise increase of the freezing fraction with decreasing temperature.

These freezing fraction curves of different experimental runs are then averaged to give the displayed average freezing curves. A visualization of this process is shown in Figure 5.2. It should be noted that not all average freezing curves contain the same number of experimental runs and freezing events and, therefore, vary in their statistical significance, which is reflected in the difference in standard deviation (error bands). T_{10}, T_{25} T_{50} and T_{75} represent the temperature at which 10 %, 25 %, 50 % and 75 % of the droplets are frozen, respectively. The temperature values are extracted for each experimental run and then averaged to obtain the values in Tables 5.1 and 5.2. The error values represent the standard deviation from the mean value.

5.3 Results

For our ice nucleation measurements, we prepared a homogeneously covering, high-quality polycrystalline monolayer graphene film on Cu foils (25 µm thickness) by CVD (graphene/Cu).[147] For comparison we also produced bare reference Cu foil samples (Cu) with the same Cu microstructure by annealing under the same conditions as used in CVD but without the hydrocarbon exposure/graphene growth step. This similarity in Cu microstructure between CVD graphene/Cu and bare reference Cu samples is

essential to allow us to attribute changes in ice nucleation temperatures solely to the presence of the CVD graphene (i.e. differences arising from Cu microstructure are thereby excluded). Microscopic and spectroscopic characterisation of the graphene/Cu and bare Cu samples is shown in Figure 5.3.

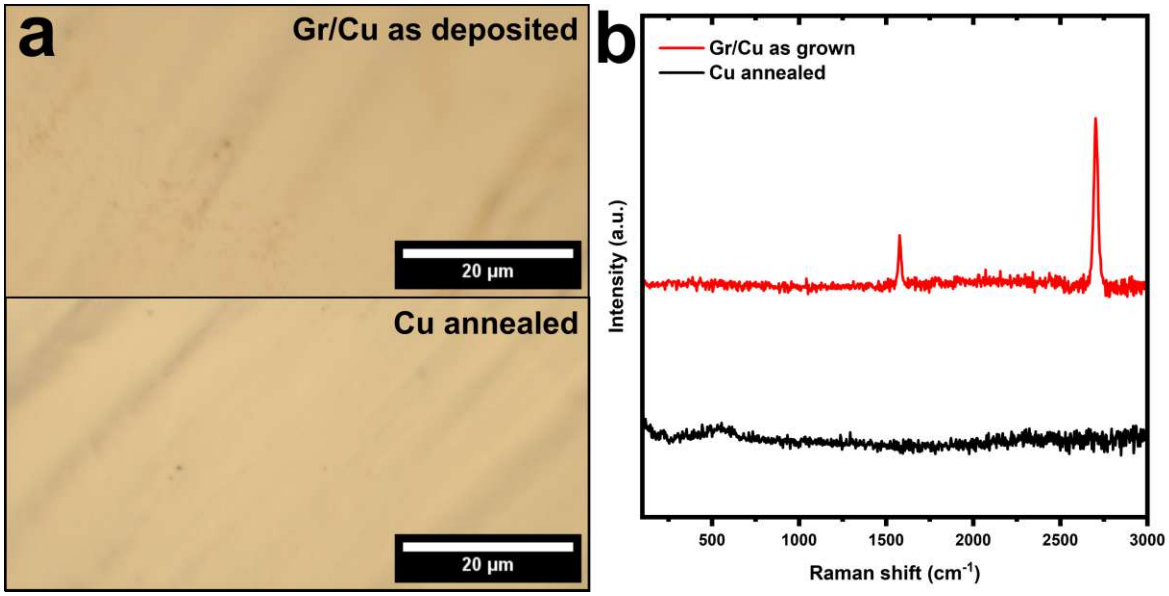

Figure 5.3: (a) Optical microscopy and (b) Raman spectroscopic characterisation of as deposited graphene/Cu (top) and annealed bare Cu (bottom) samples. The Raman spectrum in (b) clearly confirms that our CVD graphene films on Cu are almost exclusively monolayer and of high quality.[147,149] Additional transfer experiments of the monolayer graphene films from the Cu to SiO_2(90 nm)/Si wafers (not shown) allow us to confirm via optical microscopy[150] that the coverage of the Cu samples with monolayered graphene is >99 % areal coverage. Raman also confirms the bare annealed Cu sample to be void of significant carbon deposits (beyond adventitious hydrocarbon adsorbates).[149]

Additionally, we investigated the effect of several functionalization treatments to the graphene/Cu stacks (and the bare Cu references). Firstly, the exposure of CVD graphene to an air plasma (2 s), resulting in physical damage to the graphene and covalent bonding of oxygen-containing groups to the graphene defects from subsequent air exposure (Figure 5.4). Secondly, the exposure to an SF_6 plasma (2 s), resulting in damage of the graphene and covalent formation of fluorographene (also known as "2D Teflon", Figure 5.14).[32] Thirdly, the functionalization of the graphene with polymeric PMMA particles via deposition and subsequent removal of a drop cast PMMA layer on the samples, which is known to result in persistent PMMA nanoparticle contamination of CVD graphene (Figure 5.5).[203] Samples were stored in ambient air after fabrication. The state of samples was investigated by optical microscopy, Raman spectroscopy and X-ray photoelectron spectroscopy (XPS) in parallel to ice nucleation measurements. Unless otherwise stated, ice nucleation measurements were always performed after ~24 h after

the last fabrication step in order to ensure a comparable level of inevitable adventitious hydrocarbon contamination adsorption from ambient air storage accumulated on the samples.[175,176] This is key, as prior work on wetting transparency of water on graphene has shown that different adventitious carbon contamination levels can significantly alter graphene's wetting behaviour, making comparison for non-ambient-exposure-time controlled samples difficult.[172–176,178,179] For selected samples in our study also the time evolution of freezing behaviour as a function of storage time in ambient (2 h to 1 month) and corresponding hydrocarbon contamination was assessed in order to disentangle the effect of the inevitable hydrocarbon adsorption. Further details on sample preparation and characterisation can be found in the methods section 5.2.

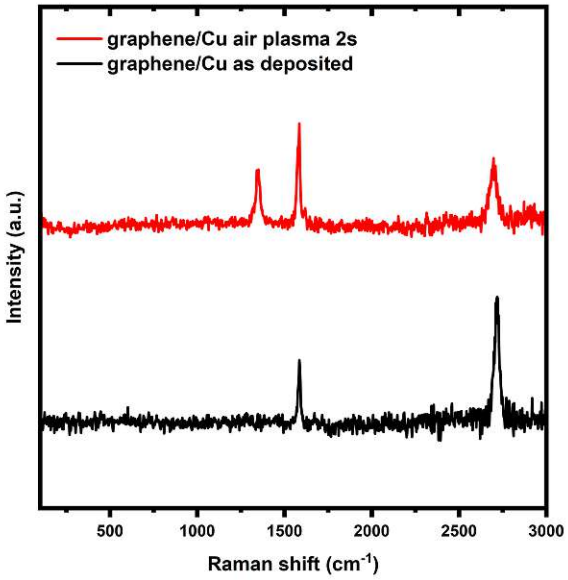

Figure 5.4: Raman spectra of graphene/Cu samples after 2 s air plasma, confirming plasma induced damage to the graphene via appearance of a pronounced defect-related D peak (~1350cm^{-1}).[149] These defects are known to be readily decorated with oxygen-containing groups during the air plasma and when exposed to ambient air.[210]

The detailed experimental procedure is explained in the methods section 5.2. The recorded optical microscope image sequences were analysed manually and with the help of a custom-programmed image analysis algorithm (see Methods section 5.2), measuring freezing temperatures (and diameters) for multiple (10 to >40) water droplets per individual sample from such freezing optical microscopy video series. Multiple individual samples were measured per every sample fabrication run. This data is then presented as freezing curves for each sample condition (e.g., Figure 5.6), showing the fraction (in %) of frozen water droplets (frozen droplets fraction) versus temperature. The here presented freezing curves all consist of data from repeated runs and plot interpolated, averaged curves (detailed explanation on data treatment in Methods section 5.2). We emphasize

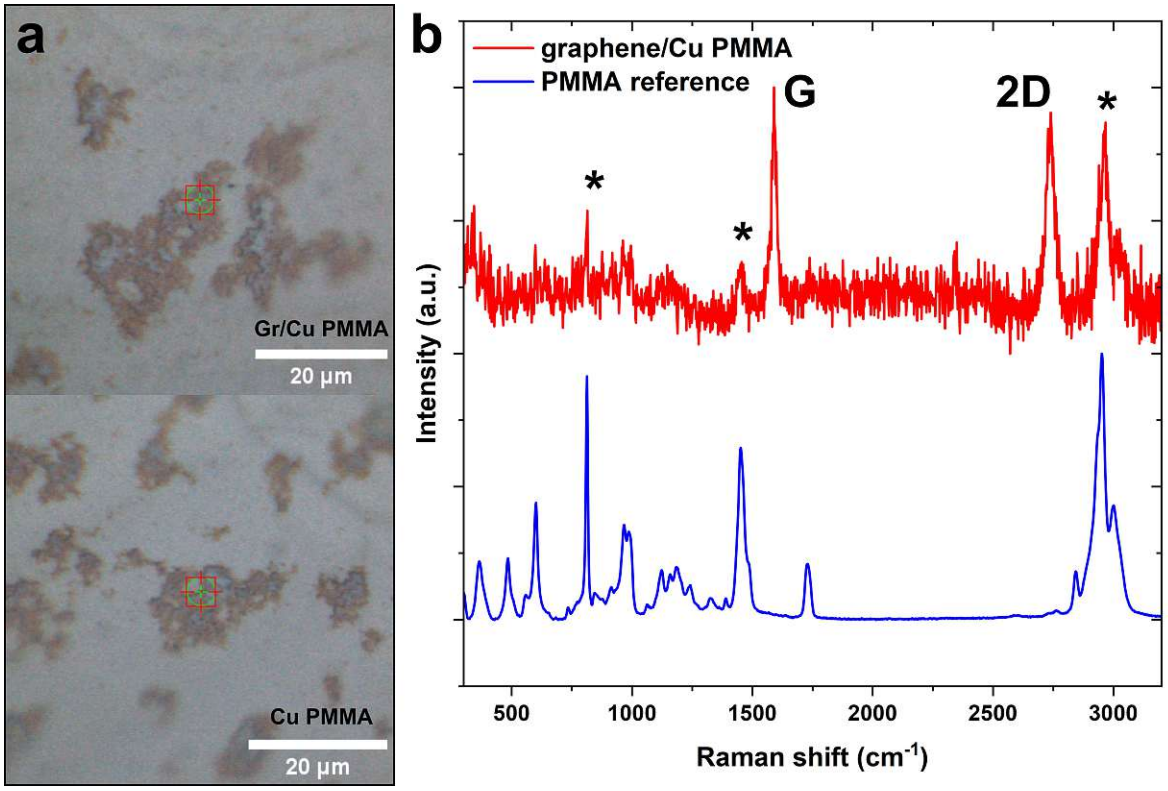

Figure 5.5: (a) Optical micrographs of graphene/Cu (top) samples decorated with PMMA functionalization via deposition and subsequent removal of a drop cast PMMA layer.[203] Large persistent PMMA deposits are visible on the surface in addition to the well-known nanoscopic residual PMMA nanoparticles from this treatment.[203] Reference bare Cu (bottom) shows a similar amount of macroscopic PMMA residue after PMMA drop cast and removal. (b) Raman spectrum of graphene/Cu (top) sample decorated with PMMA, confirming the presence of PMMA functionalization on the CVD graphene and reference Raman spectrum of PMMA film[211] (bottom). PMMA peaks visible in graphene/Cu Raman spectrum are marked with '*'. We note that the PMMA signal overlaps in the region of the D peak of graphene (~1350cm^{-1}), therefore complicating interpretation. It is however well known that graphene does not structurally degrade from such PMMA functionalization.[149]

that to date no experimental work has studied such ensemble freezing curves for water on graphene films.[61,104] Estimated uncertainties based on the standard deviation of the freezing curves and extracted values are presented. For applications, the onset temperature of freezing for a macroscopic water deposit is often important. To extract a simple comparative estimate for such onset of freezing for a given droplet ensemble on a macroscopic sample, we extracted a T_{10} value at which 10% of water droplets have frozen for a given sample, from our freezing curves. Likewise, we also extract T_{25}, T_{50} and T_{75} values at which 25%, 50% and 75% of droplets have frozen, respectively. We tabulate these temperature values for the various studied sample conditions in Table 5.1 and 5.2. Further details on the freezing experiments and their analysis procedure can be found in the methods section 5.2.

5.3.1 Freezing on as-grown graphene/Cu

Figure 5.6 compares freezing curves of the CVD graphene/Cu stack (solid black line) compared to the bare Cu reference (dashed black line). The freezing curve data shown in Figure 5.6 shows averaged freezing fraction curves of >20 separate runs for each sample type with 10 to 30 droplet freezing events in each run and also includes uncertainty bands (shaded bands, calculated from standard deviations). What is strikingly apparent from Figure 5.6 is that no significant difference in the freezing behaviour between CVD graphene/Cu stacks (solid black line) and bare Cu references (dashed black line) is observed. For both sample types, little freezing is observed before reaching –25 °C, with then a small increase in frozen droplets between –25 °C to –30 °C and then rapid freezing starting at around –30 °C and ending with all droplets frozen around –34 °C. For comparison, homogeneous ice nucleation temperature of water in the absence of a heterogeneous surface to nucleate is commonly reported at –36 °C to –38 °C.[212]

The data shows that under our measurement conditions, both graphene/Cu and Cu allow significant undercooling of water droplets below 0 °C before heterogeneous ice nucleation occurs. Importantly, comparing graphene/Cu and Cu, we neither observe differences in the onset temperatures of freezing, nor significant differences in the further freezing fraction evolution upon further cooling. This suggests that non-treated, as-grown CVD graphene on Cu is (as we term it) "freezing transparent" compared to bare Cu references at our measurement conditions. We here introduce the term "freezing transparency" in analogy to the prior studied "wetting transparency" of graphene[172–179] and define it as the case when the presence of the graphene on a given support does not change the freezing temperature evolution of water compared to on the bare support.

The freezing transparency behaviour of the graphene on Cu in our measurements is also reflected in the calculated T_{10}, T_{25}, T_{50} and T_{75} values in Table 5.1 and which are identical within our error margin for Cu/graphene and the bare Cu reference. We note that we do not evidence a distinct difference in water droplet sizes for graphene/Cu stacks and bare Cu, as both show largely similar droplet size distributions (Figure 5.7). Within the respective size distributions, we find a weak trend of larger droplets freezing at higher temperatures similarly for both samples (Figure 5.8), which is well in line with general heterogeneous ice nucleation theory, where a larger contact area from a larger water droplet is related to a larger propensity for ice nucleation.[213]

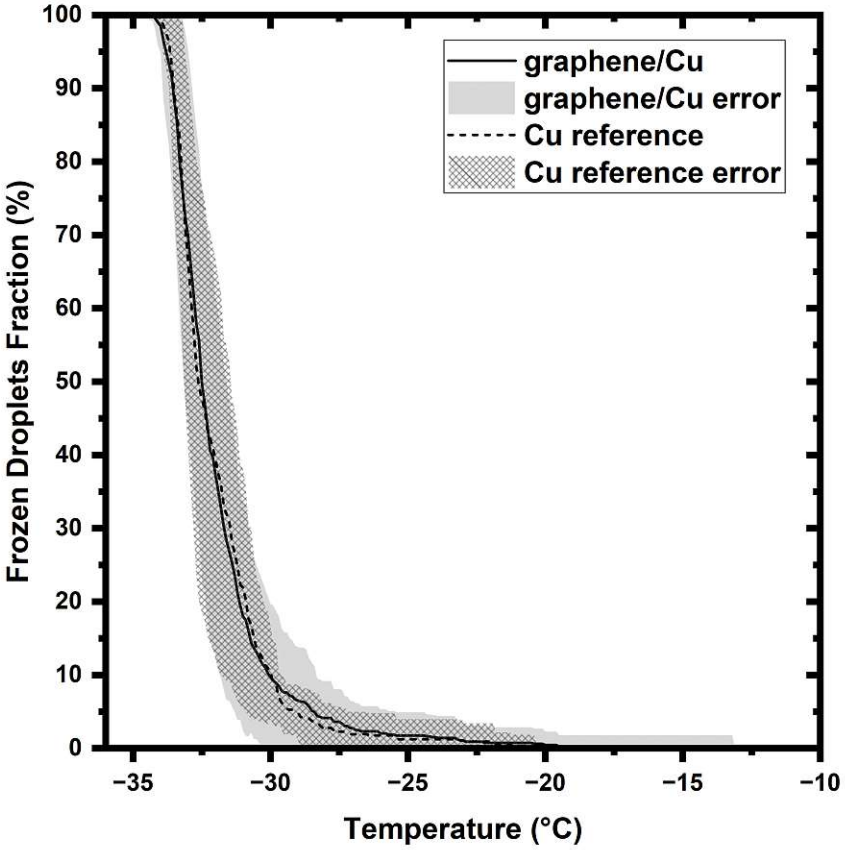

Figure 5.6: Freezing curves of non-treated, as-grown CVD graphene/Cu stacks (solid black) and bare Cu references (dashed black). Curves are averages of >20 separate runs for each sample type with 10 to 30 droplet freezing events in each run from multiple sample preparations. Shaded areas represent standard deviation bands to the freezing curves.

To date, such freezing transparency of graphene to water ice, as observed here, has not been reported in the literature. Therefore, we first discuss our here reported observation of freezing transparency in light of the existing and related literature on the wetting transparency of graphene for liquid water.[172–179]

Wetting transparency of graphene is defined as water having the same wetting behaviour (defined typically by contact angle) to a given substrate even if a monolayer of graphene is sandwiched between the water and the given substrate (i.e. analogous to our above introduced definition of freezing transparency).[172–179] Across a series of reports, graphene has been reported to be fully wetting transparent, partially wetting transparent or not wetting transparent at all.[172–179] Full wetting transparency is said to occur when the contact angle of the graphene/substrate stack is the same as of the bare substrate, partial wetting transparency when the measured contact angle is between freestanding graphene's and bare substrate's respective contact angles and no

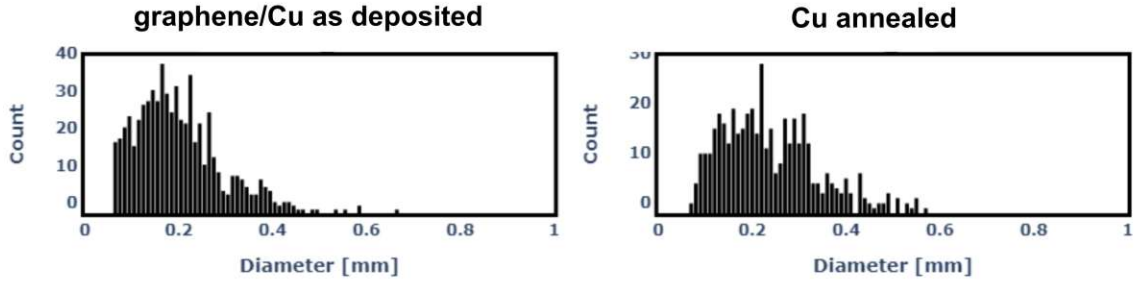

Figure 5.7: Histograms of water droplet diameters for graphene/Cu (left panel) and bare annealed Cu (right panel).

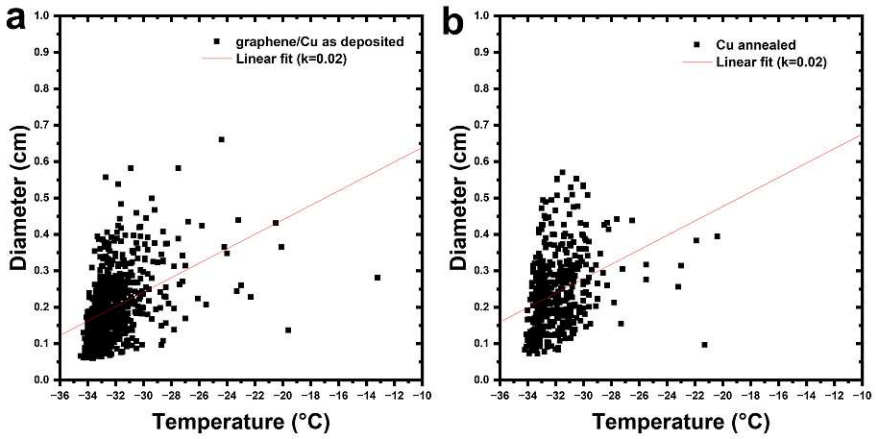

Figure 5.8: Dependence of freezing temperature on droplet diameter for as-deposited graphene/Cu (right panel) and bare annealed Cu (left panel). Linear fit and slope (k) as a guide for the eye.

wetting transparency when the measured contact angle is the same as on freestanding graphene irrespective of its substrate. The disparities in the literature regarding the presence, partial, or absence of wetting transparency have emerged to be related to several factors contributing to the wettability of graphene, incl. not only graphene's intrinsic wettability but also environmental factors.[172–179] In terms of environmental factors in particular adsorbed adventitious carbon contamination build-up and the type of substrate underneath the graphene have been identified to play key roles in graphene's wetting transparancy.[172–179] An emerging consensus in the literature is that graphene can be at least partially wetting transparent when: i. the graphene is monolayered, ii. the graphene's interaction with its substrates is weak (i.e. the substrate does not strongly alter the graphene's electronic structure) and iii. the graphene has only low levels of adventitious carbon adsorbate build-up on top.[172–179]

Cu, as used in our study as substrate, is such a weakly interacting substrate for

graphene.[61,176] Consequently, for fresh, monolayered CVD graphene on Cu (partial) wetting transparency has been experimentally observed.[172–176] In contrast for strongly interacting Ni no wetting transparency of monolayered CVD graphene was observed.[176] Notably however, the observed wetting behaviour of graphene/Cu showed a significant time dependence for samples stored under ambient conditions, with over time changing presence or absence of (partial) wetting transparency over timeframes from h to years.[175,176] This has been shown to be related to adventitious carbon contamination from ambient building up on all samples over time, which with long enough storage time in ambient leads to the adventitious carbon contamination's wetting properties completely overshadowing the sample's wetting properties.[175,176]

To ensure a constant level of adventitious carbon contamination in our sample series,[175,176] all above-presented measurements have therefore been acquired ~24 h after sample fabrication. To further explore the evolution of the freezing behaviour on our samples as a function of longer storage time, we present in Figure 5.9 freezing curves for storage in ambient until 1 month. We find that after 1 week, freezing curves on Cu are similar to the ~24 h measurements, while for graphene/Cu, after 1 week, a shift of the freezing curve to a slightly higher temperature is observed. This suggests that the freezing transparency has been lifted by the longer ambient air storage. After 1 month of storage, the onset temperatures of freezing for Cu and the entire freezing curves for graphene/Cu have shifted to higher temperatures. Importantly, also after 1 month, the curves for graphene/Cu and Cu do not overlap any more, i.e. freezing transparency has disappeared (Figure 5.9). We suggest that this upshift of freezing temperatures and disappearance of freezing transparency is related to the substantial adventitious carbon contamination build-up from extended ambient storage.[175,176] Importantly, the 1 month data in Figure 5.9 thereby also shows that the freezing transparency at shorter storage times is not only a result of adventitious carbon contamination since such contamination would be most dominating for the 1 month sample, where freezing transparency was however lifted.

On the other hand, in Figure 5.10, we probe the freezing behaviour of our graphene/Cu and Cu samples after shorter storage times of only ~2 h in ambient. Based on prior literature,[175,176] we know that for these samples the adventitious carbon contamination levels will be as low as technically possible for our measurement facilities (given how fast we can reliably bring samples from fabrication to ice nucleation measurements). We find that for such samples the onset temperature for freezing and entire freezing curves are significantly shifted to higher temperatures. Also, the freezing curves for

graphene/Cu and Cu do not overlap perfectly any more for the ~2 h stored samples, indicating an at least partial absence of the freezing transparency of the ~2 h stored samples.

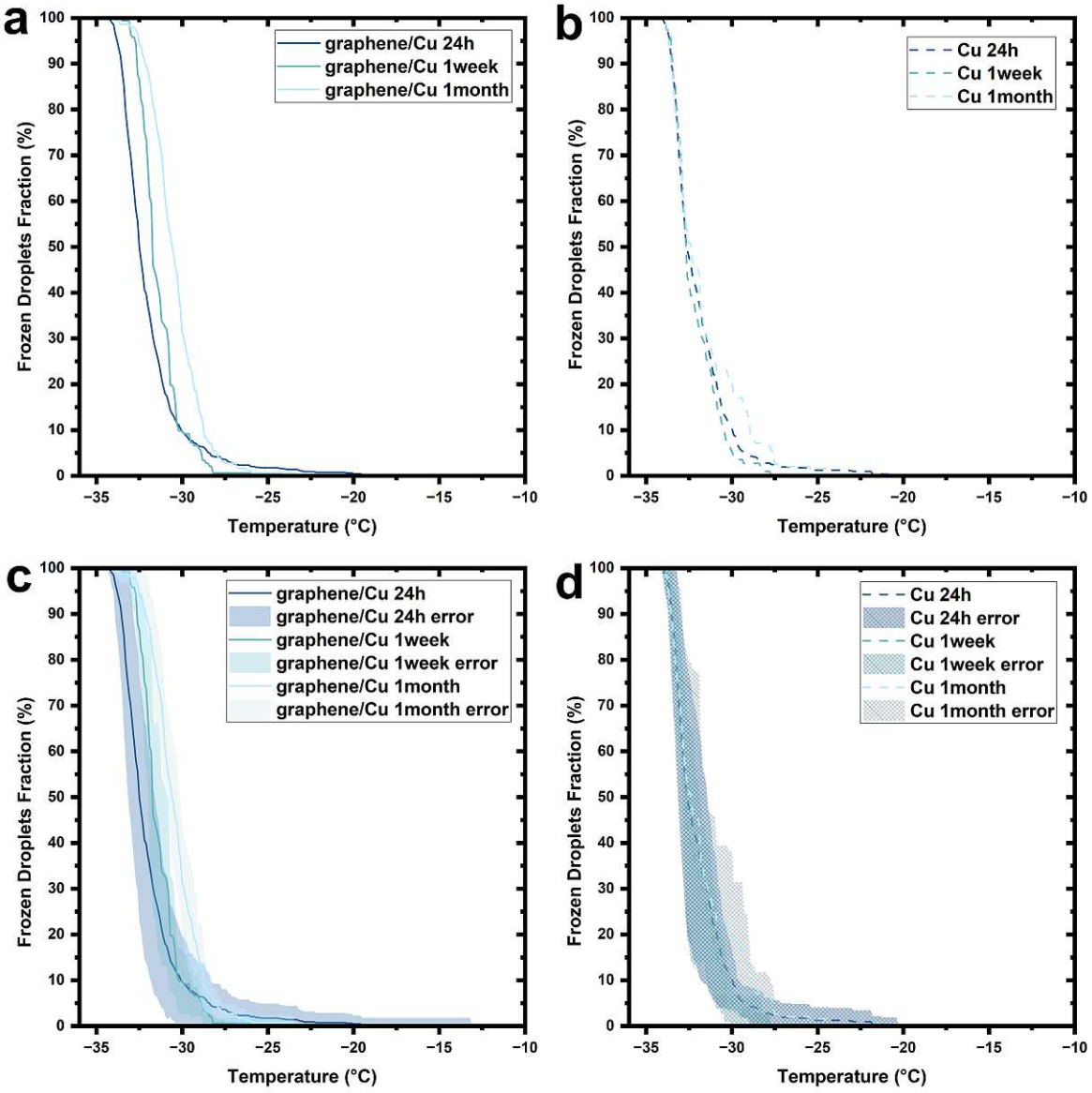

Figure 5.9: Freezing curves on (a) graphene/Cu as-deposited and (b) Cu annealed as a function of storage time in ambient conditions from ~24 h to 1 month (24 h data replotted from Figure 5.6). Panels (c) and (d) show respective plots of (a) and (b) with error bands representing their standard deviation.

Combined, Figure 5.9 and 5.10 therefore indicate that the freezing transparency for graphene/Cu and graphene is only observed for intermediate storage time in ambient (~24 h). We suggest that this is linked to the medium adventitious carbon contamination levels after ~24 h in ambient. We emphasize, however, that for massive adventitious carbon build-up (after 1 month), the freezing transparency vanishes, which in turn suggests that the observed freezing transparency is not just an effect of freezing on

substrate-independent adventitious carbon. In fact, combining Figure 5.6, Figures 5.9 and 5.10 suggests that in order to establish the here observed freezing transparency not only the graphene in the graphene/Cu vs. Cu systems is necessary but also a mediating level of adventitious carbon on the graphene. This conclusion is reminiscent of the findings in the prior wetting transparency literature,[172–179] suggesting that similar underlying mechanisms are at play in the case of freezing on graphene films.

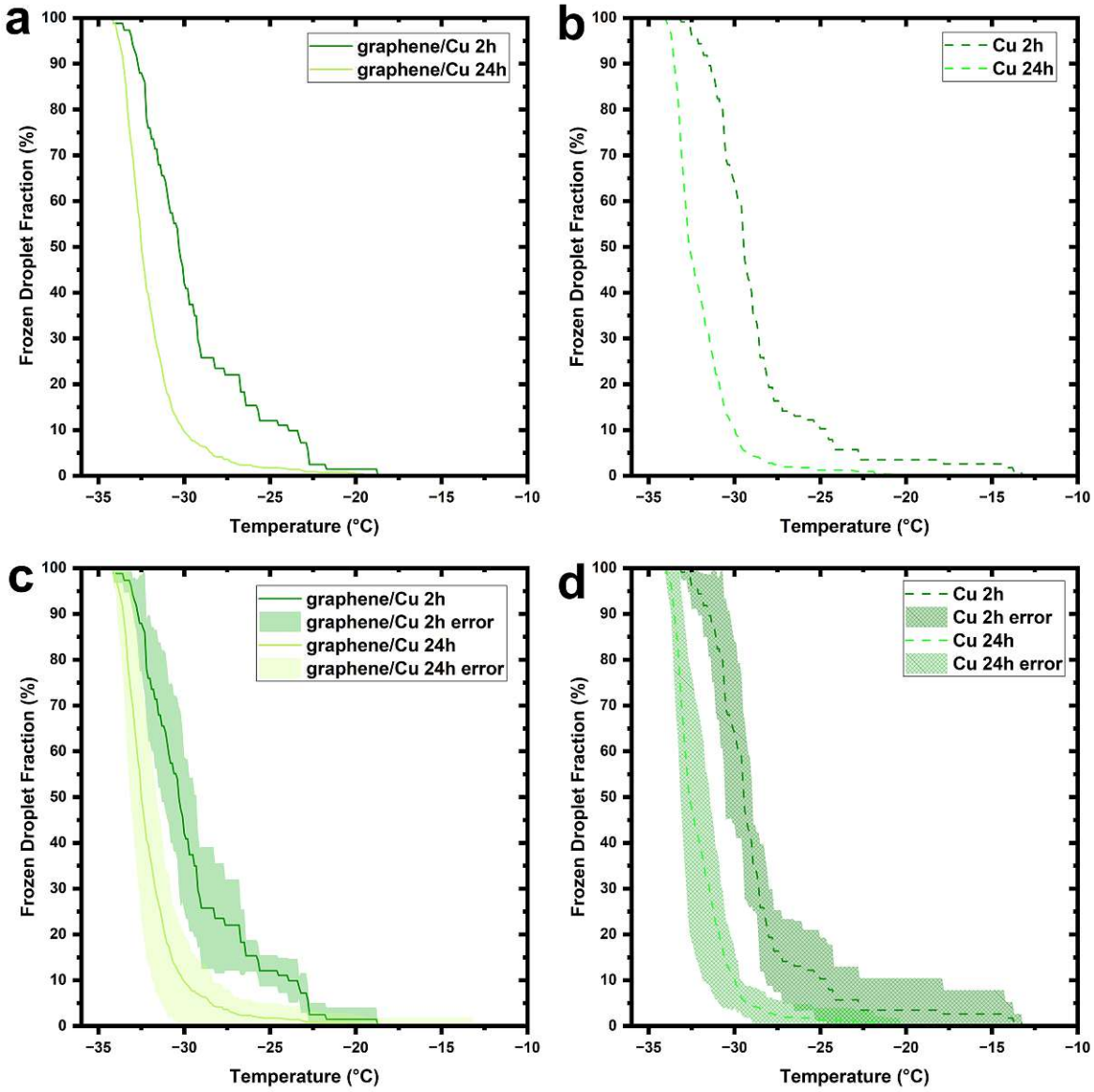

Figure 5.10: . Freezing curves on (a) graphene/Cu as-deposited and (b) Cu annealed as a function of storage time in ambient from ~2 h to ~24 h (24 h data replotted from Figure 5.6). Panels (c) and (d) show respective plots of (a) and (b) with error bands representing their standard deviation.

5.3.2 Freezing on functionalized graphene/Cu

So far, we have investigated the freezing properties of as-grown graphene on Cu, which displays the here reported freezing transparency and elucidated its time dependence on inevitable adventitious carbon contamination. In order to test if the graphene's freezing behaviour on a metal can also be controlled in a deliberate fashion beyond storage time, Figure 5.11 compares droplet freezing curves for graphene/Cu stacks and bare Cu references that additionally underwent deliberate functionalization treatments before the ice nucleation measurements. For comparison, the non-treated, as-grown graphene/Cu and bare Cu freezing curves from Figure 5.6 are re-plotted as solid and dashed black lines, respectively. All measurements in Figure 5.11 are taken after ~24 h storage in ambient conditions after the last fabrication/treatment step to ensure a fair comparison to the data in Figure 5.6.

The first treatment we investigate is covalent functionalization of the CVD graphene with oxygen-containing groups by air plasma treatment (2 s) (Figure 5.11a, red solid and dashed curves). As shown via Raman spectroscopy in Figure 5.4, such air plasma treatment incl. subsequent ambient air exposure results in severe damage to the graphene lattice and thus covalent defect functionalization of the graphene with oxygen-containing functional groups.[210] A similar state of samples has previously also been labelled as "graphene oxide"-like.[185] Such treatment is motivated by prior observation of freezing behaviour changes in atmospheric soot by different oxygen-containing groups.[193–202]

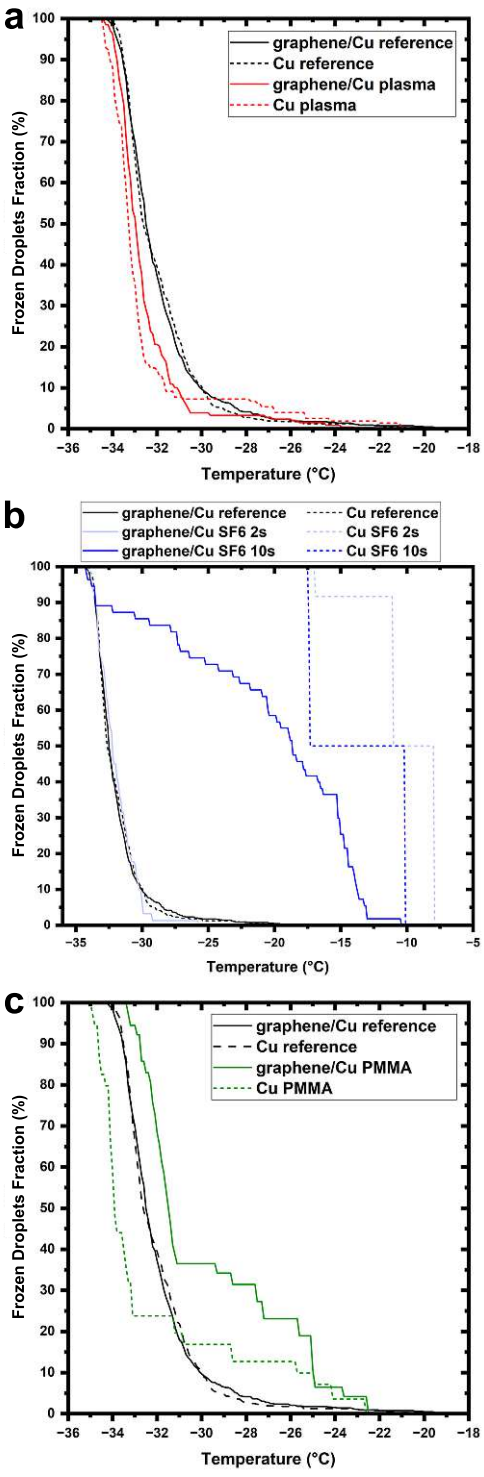

Figure 5.11: (a) Freezing curves for air plasma treated samples (x-axis scale –18 °C to –36 °C). (b) Freezing fraction curves for SF6 plasma treated samples (x-axis scale –5 °C to –36 °C). (c) Freezing curves for PMMA treated samples (x-axis scale –18 °C to –36 °C). Graphene/Cu samples are represented by solid lines and Cu samples by dashed lines, respectively. All diagrams include freezing curves of untreated, as-grown graphene/Cu (black solid) and Cu (black dashed), replotted from Figure 5.6. All curves are averages of several experimental freezing runs; a version of this figure with uncertainty bands included is shown in Appendix Figure A.5.

Notably, we find in Figure 5.11 and Table 5.1 that such air plasma-treated graphene/Cu (red solid curve) does show freezing at slightly lower temperatures (by around –1 °C) compared to non-treated, as-grown graphene/Cu (solid black) for the same ambient air storage time. Importantly also, between air-plasma-treated graphene/Cu and air-plasma-treated Cu little difference is observed, i.e. both Cu/graphene and Cu are similarly shifted to slightly lower freezing temperatures. We note that measured water droplet size distributions are not significantly different for air-plasma-treated Cu/graphene and air-plasma-treated Cu (Figure 5.12 and 5.13) compared to their non-plasma-treated counterparts (Figure 5.7 and 5.8). This suggests that it is not a different water droplet size distribution that is indirectly responsible for the slightly lower freezing temperatures, but rather suggests that the introduced oxygen-containing groups on the air-plasma-treated surfaces chemically mediate the freezing behaviour to slightly lower temperatures. The oxygen plasma experiments show that the functionalisation of graphene (here with oxygen-containing groups) can downshift the freezing temperature curve on graphene to slightly lower temperatures.

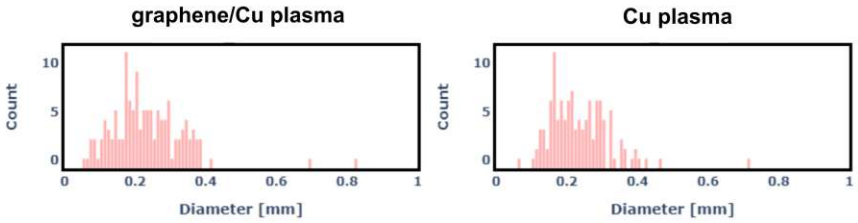

Figure 5.12: Histograms of water droplet diameters for air-plasma-treated graphene/Cu (left panel) and air-plasma-treated Cu (right panel)

The second treatment we investigate is covalent functionalization of the graphene by F i.e. formation of highly hydrophobic fluorographene or "2D Teflon".[32] This is motivated by hydrophobicity often being linked to lower freezing temperatures.[171] We fabricate this material by exposure of graphene/Cu and bare Cu references to a SF_6 plasma (2 s and 10 s). Figure 5.14 confirms that this results in strong damage to the graphene lattice and covalent functionalization of the graphene with F towards fluorographene for the 2 s SF_6 plasma. The Raman spectrum of graphene/Cu sample after 2 s SF_6 plasma treatment in Figure 5.14a confirms plasma-induced damage to the graphene via appearance of a pronounced defect-related D peak (~1350cm^{-1}) and suppression of 2D peak (~2700cm^{-1})[149] in line with partial formation of fluorographene.[32] In Figure 5.14 panels (b) and (c), for all samples the Cu 2p region consists of a doublet at around 932.4 eV and 952.2 eV matching with either Cu0 or Cu^+. Indeed, the Cu LMM region (not

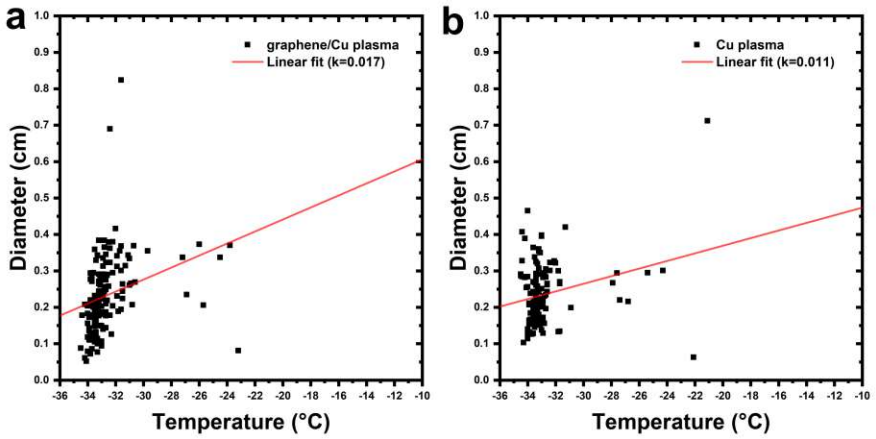

Figure 5.13: Dependence of freezing temperature on droplet diameter for air plasma treated graphene/Cu (left panel) and air plasma treated annealed Cu (right panel). Linear fit and slope (k) as guide for the eye.

shown) contains two peak maxima at a kinetic energy of 916.5 eV and 918.3 eV pointing to the presence of both Cu species.[214,215] While all non-SF_6 -plasma-treated samples are void of any F signal, the SF_6 -plasma-treatment leads to formation of an organic fluoride species ~688.5 eV (likely C-F) in the F 1s region.[32,216] For the graphene/Cu samples this is related to graphene reacting with F towards flourographene. For the Cu samples, adventitious hydrocarbon deposits react with the F. Moreover, SF_6 -plasma treatment results in the formation of CuF_2, as evident from both the presence of a metal fluoride species ~684.5 eV in the F1s region and by the Cu^{2+} doublet and satellite feature.[216,217] That said, the graphene layer appears to present a barrier against the fluorination of copper as the amount of CuF_2 present in graphene/Cu SF_6 10s is significantly lower than that of Cu SF_6 10 s. In summary, the XPS data is consistent with the Raman data in showing incorporation of F into the graphene layer for SF_6 plasma 2 s towards formation of flourographene.[32]

The corresponding freezing curves in Figure 5.11b of the 2 s SF_6-plasma-treated sample shows for graphene/Cu (solid light blue curve) a surprisingly similar freezing behaviour as on non-treated, as-grown graphene/Cu (solid black curve). This result, in turn, shows that even with a covalent functionalization, the freezing behaviour of graphene does not necessarily change. This is quite noteworthy, as in contrast the 2 s SF_6-plasma-treated Cu reference (dashed light blue curve in Figure 5.11b) shows a drastically different freezing behaviour with a very much higher freezing temperature interval already between –10 °C to –15 °C. Similarly, the 10 s SF_6-plasma-treated graphene/Cu (solid dark blue) and the 10 s SF_6 -plasma-treated Cu (dashed dark blue) samples show drastically upshifted freezing behaviour. Based on XPS in Figure 5.14, we attribute

this high-temperature onset of freezing on SF_6-plasma-treated Cu (2 s and 10 s) and on SF_6-plasma-treated graphene/Cu (10 s) to the formation of CuF_2. Notably, CuF_2 formation also results in a drastic change in water droplet sizes, shown in Figure 5.15. The presence of comparatively still intact graphene during SF_6 plasma (2 s) prevents the formation of CuF_2, while for longer SF_6 plasma (10 s) treatments, the graphene has been strongly destroyed, making room for CuF_2 formation. The SF_6-plasma experiments show that functionalization of graphene (here for F, 2 s plasma) can also leave the freezing temperature curve unaffected compared to untreated graphene.

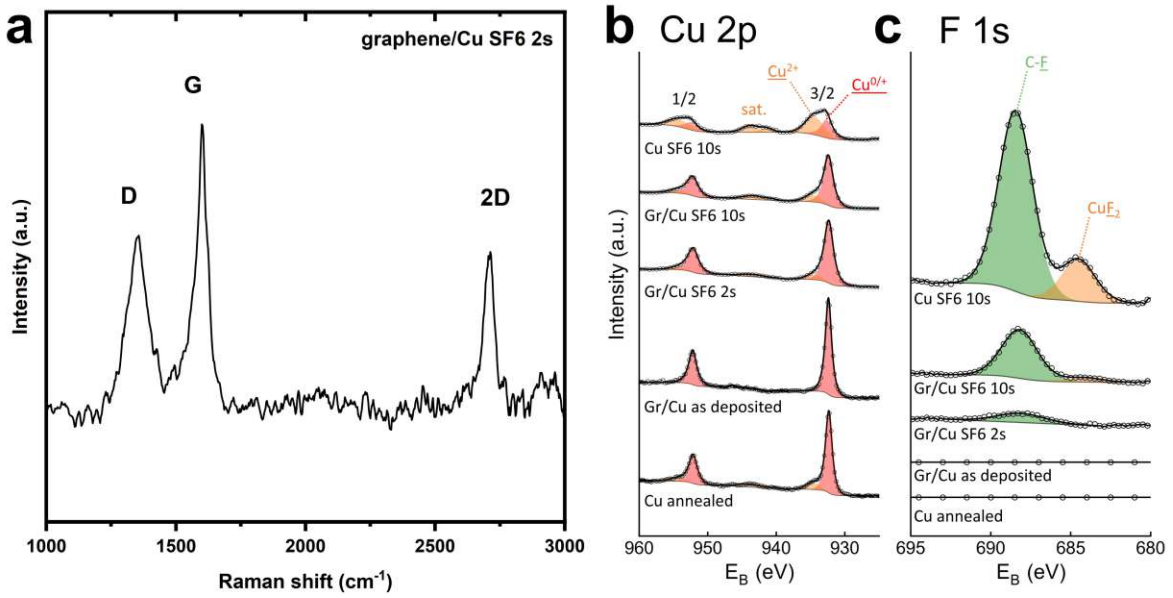

Figure 5.14: (a) Raman spectrum of graphene/Cu sample after 2 s SF_6 plasma treatment, confirming plasma induced damage to the graphene via appearance of a pronounced defect-related D peak (~1350 cm^{-1}) and suppression of 2D peak (~2700 cm^{-1}).[149] (b) Cu 2p and (c) F 1s X-ray photoelectron spectra of graphene/Cu ("Gr/Cu") and bare annealed Cu samples after 10 s plasma (top) and 2 s plasma (middle) compared to as deposited graphene/Cu and bare Cu samples (bottom). See main text for XPS and Raman data interpretation.

The third treatment that we apply to the graphene is wet chemical, non-covalent functionalization with PMMA particles that are persistently anchored onto the graphene.[203] We achieved this by drop-casting and hot plate-hardening of PMMA in anisole on the graphene/Cu and bare Cu reference samples, followed by subsequent removal of hardened PMMA in acetone/isopropanol. This is well known from prior work to lead to persistent contamination of the CVD graphene with PMMA microparticles and nanoparticles, while the graphene lattice remains structurally perfectly intact (see also our characterisation data in Figure 5.5).[203] In the corresponding freezing data in Figure 5.11c we find that for such PMMA-functionalized graphene/Cu (solid green

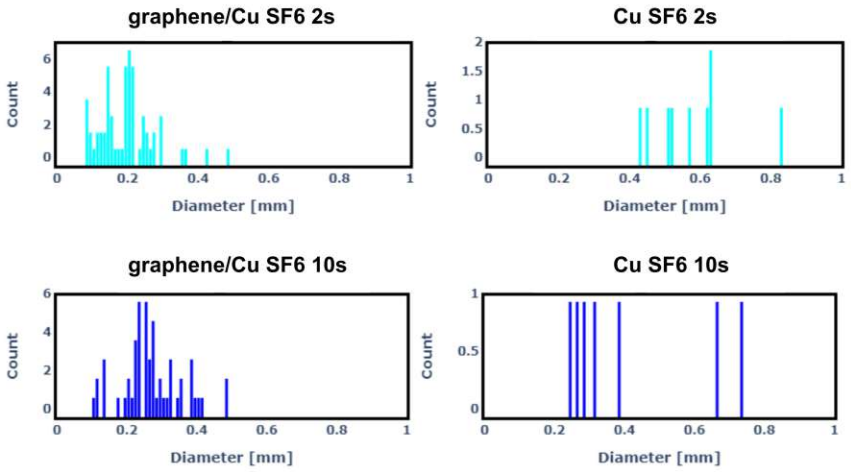

Figure 5.15: (a) Histograms of water droplet diameters for SF_6 -plasma treated (2s top panels and 10 s bottom panels) graphene/Cu (left panels) and bare annealed Cu (right panels). Showing very few and large diameter droplets for bare Cu SF_6 -plasma treated samples.

curve) this translates to a significant fraction of the water droplets already nucleating at between –25 °C and –30,°C, which is at a significantly higher temperature than for untreated, as-grown graphene/Cu (solid black curve). This is also reflected by the higher T_{10} temperature for PMMA-treated graphene/Cu compared to as-grown graphene/Cu (Table 5.1). We attribute this to the persistent PMMA particles acting as preferential nucleation sites for ice nucleation, as compared to the comparatively atomically smooth, chemically inert basal plane of non-treated, as-grown CVD graphene. This is also reaffirmed by the freezing data on PMMA-treated bare Cu (dashed green curve) which also shows a higher temperature onset of freezing (albeit less pronounced than for the PMMA-treated graphene/Cu). The PMMA experiments thus show that functionalization of graphene (here with PMMA particles) can also lead to a higher onset temperature of freezing compared to untreated graphene.

Combined, the results in Figure 5.11 indicate that the here first observed freezing behaviour of water on graphene on a metal surface (Figure 5.6) can be modified by functionalization treatments. While for the addition of oxygen-containing groups, we observe a slight down-shift of freezing temperatures (air plasma in Figure 5.11a), for the addition of polymeric residues, we observe an up-shift of freezing temperatures (PMMA in Figure 5.11c). The former down-shift is suggested to be related to a change of chemical interaction of water with the introduced oxygen-containing groups, while the latter up-shift is suggested to be related to polymeric particles acting preferential

nucleation centres for ice nucleation. Interestingly, for functionalisation with F, the freezing behaviour on graphene is not affected, while on the Cu substrate, it is strongly changed (SF_6 plasma in Figure 5.11b). The observation that introduction of oxygen-containing groups (Figure 5.11a) can decrease freezing temperatures is in line with a prior paper[185] that reported a lower freezing temperature for oxidized graphene vs. pristine graphene on UHV Ir single crystals (note that possible freezing transparency between graphene/Ir vs. Ir was not studied in this ref.[185]). The results in Figure 5.11c on the effect of deliberate PMMA contamination to alter freezing behaviour via increased ice nucleation, links well with prior work on PMMA residues (and similar polymer residues) to have an significant effect on graphene wetting.[178] Also, the results in Figure 5.11b regarding SF_6 plasma (flourographene) are interesting compared to prior literature: While in our experiments we do not evidence any significant change in freezing behaviour for the fluorinated graphene on Cu, in contrast a prior study[184] reported a lower freezing temperature for flourographene vs. pristine graphene on UHV Ru single crystals (note that possible freezing transparency between graphene/Ru vs. Ru was not studied in this ref.[184]). This discrepancy suggests that substrate effects (Ru vs. Cu) could be important in the freezing behaviour of graphene, which is also in line with the importance of substrate effects in wetting behaviour of graphene.[176,178]

We also want to discuss the limitations of our here presented study. We report hitherto not observed water freezing transparency of graphene/Cu vs. Cu under our conditions. We emphasize, however, that the presence or absence of such freezing transparency is suggested to be contingent on several factors. As already shown here, a key factor is storage time in ambient and its linked adventitious carbon contamination build-up. We further suggest that the type of substrate is key to the observed freezing behaviour. While here freezing transparency on weakly interacting Cu is observed, more interacting substrates such as Ni[176] or Fe as supports may result in different freezing behaviour on such supported CVD graphene. Furthermore, in comparison to wetting experiments, freezing experiments also have a much wider parameter space in terms of environmental conditions and experimental approaches.[171] While wetting experiments almost exclusively use contact angle measurements, for freezing experiments, the experimental pathways to bring the water to the surface and induce its freezing are much more varied: We here employ freezing of pre-supported water droplets in a dry atmosphere. Freezing experiments can however also include other water delivery pathways such as condensation freezing from a highly humid atmosphere or droplet impingement freezing on pre-cooled surfaces.[171] The type of droplet delivery and cooling pathways have been prior shown to significantly alter freezing behaviour on various surfaces incl., e.g., widely

studied SLIPS.[171]

We therefore emphasize that our reported findings here are a first experimental impetus to explore the currently critically under-investigated freezing behaviour on scalable graphene and other 2D materials films, incl. the here found freezing transparency, in a similar fashion as the wetting behaviour of graphene and other 2D materials has been extensively studied in the recent past.[172–179] We also note that such experimental investigations will provide key feedback to all the computational work that currently uses graphene as model surfaces for fundamental investigation of ice nucleation and on the hitherto overlooked freezing transparency.

We also note that the here introduced freezing transparency concept not only links to prior work on wetting behaviour/wetting transparency of graphene, but in a wider realm also to other phenomena that rely on substrate properties to emanate through atomically thin graphene/2D materials:[183] These include, e.g., graphene-substrate-assisted growth modes of extraneous films on graphene from vapour phase techniques[32,214] as well as "remote" epitaxy in which epitaxial relations between a substrate and a deposited film are kept despite the presence of a sandwiched graphene interlayer.[215] These processes similarly rely on a phase transition of an extraneous material (here water/ice) on an atomically thin 2D material sandwiched between the extraneous material and a bulk support, as explored here for water freezing on graphene/Cu.

5.4 Conclusion

In summary, we have experimentally studied the water-freezing behaviour of scalable CVD graphene films grown on application-relevant Cu. It was found that as-grown CVD graphene on Cu can be "freezing transparent", which is a term that we introduce to describe the phenomenon when freezing curves on graphene/Cu vs. bare Cu reference samples are identical i.e. the presence of graphene does not change the water freezing behaviour compared to on its bare underlying substrate. We explored the conditions in which such freezing transparency can be observed and also explored how chemical functionalisation of the graphene films can result in changes to freezing evolution to lower/higher temperatures. Our work thus introduces the concept of freezing transparency of graphene on a metal based on the first experimental observation and also introduces scalable CVD graphene as an ultimately thin materials platform for control of ice nucleation and water freezing behaviour on a technologically relevant metal.

5.5 Publication Notice

This chapter has been submitted for publication and is listed as number 2 in the publication list.

	T_{10}	ΔT_{10}	T_{25}	ΔT_{25}	T_{50}	ΔT_{50}	T_{75}	ΔT_{75}
Graphene/Cu as-grown	–30.1	± 2.0	–31.6	± 1.1	–32.4	± 0.8	–33.0	± 0.7
Graphene/Cu air plasma	–30.9	± 1.7	–32.3	± 0.7	–33.0	± 0.5	–33.4	± 0.5
Graphene/Cu PMMA	–26.4	± 3.2	–28.4	± 3.5	–29.3	± 3.5	–32.1	± 0.5
Graphene/Cu SF6 plasma 2 s	–30.4	± 0.6	–31.1	± 0.5	–32.4	± 0.3	–33.1	± 0.3
Graphene/Cu SF6 plasma 10 s	–15.5	± 2.5	–17.6	± 5.2	–20.6	± 6.3	–23.8	± 7.9
Cu annealed	–30.5	± 1.4	–31.6	± 1.1	–32.3	± 0.9	–32.9	± 0.5
Cu air plasma	–30.4	± 4.0	–32.1	± 2.0	–33.3	± 0.4	–33.8	± 0.4
Cu PMMA	–26.9	± 3.8	–30.4	± 4.3	–33.9	± 0.3	–34.2	± 0.2
Cu SF6 plasma 2s	–9.6	± 2.2	–9.6	± 2.2	–9.6	± 2.2	–9.6	± 2.2
Cu SF6 plasma 10s	–13.8	± 5.1	–13.8	± 5.1	–13.8	± 5.1	–13.8	± 5.2

Table 5.1: T_{10}, T_{25}, T_{50} and T_{75} values in °C and their standard deviations (ΔT_{xx}) for our various samples for graphene/Cu and bare annealed Cu as fabricated and after the various functionalizations (all measured 24 h after last fabrication step).

	T_{10}	ΔT_{10}	T_{25}	ΔT_{25}	T_{50}	ΔT_{50}	T_{75}	ΔT_{75}
Graphene/Cu as-grown	–30.1	± 2.0	–31.6	± 1.1	–32.4	± 0.8	–33.0	± 0.7
Graphene/Cu 2 h	–25.6	± 2.6	–28.1	± 1.7	–30.6	± 1.0	–31.8	± 1.2
Graphene/Cu 24 h	–29.8	± 0.6	–31.0	± 0.4	–31.8	± 0.6	–32.6	± 0.6
Graphene/Cu 1 week	–30.1	± 1.1	–31.0	± 0.7	–31.6	± 0.5	–32.2	± 0.3
Graphene/Cu 1 month	–28.9	± 0.6	–29.6	± 0.5	–30.6	± 0.5	–31.3	± 0.5
Cu annealed	–30.5	± 1.4	–31.6	± 1.1	–32.3	± 0.9	–32.9	± 0.5
Cu 2 h	–23.4	± 5.5	–28.1	± 1.3	–29.6	± 0.8	–30.4	± 0.7
Cu 24 h	–28.9	± 3.7	–31.4	± 1.2	–32.4	± 0.6	–32.9	± 0.3
Cu 1 week	–30.7	± 0.6	–31.9	± 0.9	–32.4	± 0.7	–33.1	± 0.5
Cu 1 month	–29.2	± 1.8	–31.2	± 1.5	–32.2	± 1.5	–32.9	± 0.7

Table 5.2: T_{10}, T_{25}, T_{50} and T_{75} values in °C and their standard deviations (ΔT_{xx}) for graphene/Cu and bare annealed Cu samples after various storage times in ambient conditions.

Bibliography

32. Robinson, J. T. *et al.* Properties of Fluorinated Graphene Films. *Nano Letters* **10,** 3001–3005. ISSN: 1530-6984, 1530-6992. doi:10.1021/nl101437p (2010).

61. Kidambi, P. R. *et al.* Observing graphene grow: Catalyst-graphene interactions during scalable graphene growth on polycrystalline copper. *Nano Letters* **13,** 4769–4778. ISSN: 15306984. doi:10.1021/nl4023572 (2013).

104. Lin, L., Deng, B., Sun, J., Peng, H. & Liu, Z. Bridging the Gap between Reality and Ideal in Chemical Vapor Deposition Growth of Graphene. *Chemical Reviews* **118,** 9281–9343. ISSN: 15206890. doi:10.1021/acs.chemrev.8b00325 (2018).

147. Fuchs, D. *et al.* Electrochemical Behavior of Graphene in a Deep Eutectic Solvent. *ACS applied materials & interfaces* **12,** 40937–40948. ISSN: 1944-8252. doi:10.1021/acsami.0c11467 (2020).

149. Ferrari, A. C. Raman spectroscopy of graphene and graphite: Disorder, electron-phonon coupling, doping and nonadiabatic effects. *Solid State Communications* **143,** 47–57. ISSN: 00381098. doi:10.1016/j.ssc.2007.03.052 (2007).

150. Blake, P. *et al.* Making graphene visible. *Applied Physics Letters.* ISBN: 0003-6951. ISSN: 00036951. doi:10.1063/1.2768624. arXiv: 0705.0259 (2007).

171. Kreder, M. J., Alvarenga, J., Kim, P. & Aizenberg, J. Design of anti-icing surfaces: Smooth, textured or slippery? *Nature Reviews Materials* **1.** ISSN: 20588437. doi:10.1038/natrevmats.2015.3 (2016).

172. Rafiee, J. *et al.* Wetting transparency of graphene. *Nature Materials* **11.** Publisher: Nature Publishing Group, 217–222. ISSN: 14764660. doi:10.1038/nmat3228 (2012).

173. Shih, C.-J. *et al.* Breakdown in the Wetting Transparency of Graphene. *Physical Review Letters* **109.** Publisher: American Physical Society, 176101. doi:10.1103/PhysRevLett.109.176101 (2012).

174. Raj, R., Maroo, S. C. & Wang, E. N. Wettability of graphene. *Nano Letters* **13,** 1509–1515. ISSN: 15306984. doi:10.1021/nl304647t (2013).

175. Li, Z. *et al.* Effect of airborne contaminants on the wettability of supported graphene and graphite. *Nature Materials* **12.** Publisher: Nature Publishing Group, 925–931. ISSN: 1476-4660. doi:10.1038/nmat3709 (2013).

176. Aria, A. I. *et al.* Time Evolution of the Wettability of Supported Graphene under Ambient Air Exposure. *Journal of Physical Chemistry C* **120,** 2215–2224. ISSN: 19327455. doi:10.1021/acs.jpcc.5b10492 (2016).

177. Prydatko, A. V., Belyaeva, L. A., Jiang, L., Lima, L. M. C. & Schneider, G. F. Contact angle measurement of free-standing square-millimeter single-layer graphene. *Nature Communications* **9.** Publisher: Nature Publishing Group, 4185. ISSN: 2041-1723. doi:10.1038/s41467-018-06608-0 (2018).

178. Belyaeva, L. A. & Schneider, G. F. Wettability of graphene. *Surface Science Reports* **75.** Publisher: Elsevier B.V. ISSN: 01675729. doi:10.1016/j.surfrep.2020.100482 (2020).

179. Snapp, P. *et al.* Interaction of 2D materials with liquids: wettability, electrochemical properties, friction, and emerging directions. *NPG Asia Materials* **12.** Publisher: Nature Publishing Group, 1–16. ISSN: 1884-4057. doi:10.1038/s41427-020-0203-1 (2020).

180. Dlubak, B., Kidambi, P. R., Weatherup, R. S., Hofmann, S. & Robertson, J. Substrate-assisted nucleation of ultra-thin dielectric layers on graphene by atomic layer deposition. *Applied Physics Letters* **100,** 173113. ISSN: 0003-6951. doi:10.1063/1.4707376 (2012).

181. Bayer, B. C., Aria, A. I., Eder, D., Hofmann, S. & Meyer, J. C. Resolving the Nucleation Stage in Atomic Layer Deposition of Hafnium Oxide on Graphene. arXiv: 1909.00712 (2019).

182. Kim, Y. *et al.* Remote epitaxy through graphene enables two-dimensional material-based layer transfer. *Nature* **544.** Publisher: Nature Publishing Group, 340–343. ISSN: 1476-4687. doi:10.1038/nature22053 (2017).

183. Kong, W. *et al.* Polarity governs atomic interaction through two-dimensional materials. *Nature Materials* **17.** Publisher: Nature Publishing Group, 999–1004. ISSN: 1476-4660. doi:10.1038/s41563-018-0176-4 (2018).

184. Akhtar, N., Anemone, G., Farias, D. & Holst, B. Fluorinated graphene provides long lasting ice inhibition in high humidity. *Carbon* **141.** Publisher: Elsevier Ltd, 451–456. ISSN: 00086223. doi:10.1016/j.carbon.2018.09.008 (2019).

185. Kyrkjebø, S. *et al.* Graphene and graphene oxide on Ir(111) are transparent to wetting but not to icing. *Carbon* **174,** 396–403. ISSN: 00086223. doi:10.1016/j.carbon.2020.12.030 (2021).

186. Cline, C. *et al.* Heterogeneous Ice Nucleation Studied with Single-Layer Graphene. *Langmuir* **38.** Publisher: American Chemical Society, 15121–15131. ISSN: 0743-7463. doi:10.1021/acs.langmuir.2c02144 (2022).

187. Lupi, L., Hudait, A. & Molinero, V. Heterogeneous nucleation of ice on carbon surfaces. *Journal of the American Chemical Society* **136,** 3156–3164. ISSN: 00027863. doi:10.1021/ja411507a (2014).

188. Lupi, L. & Molinero, V. Does Hydrophilicity of Carbon Particles Improve Their Ice Nucleation Ability? *The Journal of Physical Chemistry A* **118.** Publisher: American Chemical Society, 7330–7337. ISSN: 1089-5639. doi:10.1021/jp4118375 (2014).

189. Zhang, X.-X. & Chen, M. Icephobicity of Functionalized Graphene Surfaces. *Journal of Nanomaterials* **2016.** Publisher: Hindawi, e6731840. ISSN: 1687-4110. doi:10.1155/2016/6731840 (2016).

190. Bi, Y., Cabriolu, R. & Li, T. Heterogeneous ice nucleation controlled by the coupling of surface crystallinity and surface hydrophilicity. *Journal of Physical Chemistry C* **120,** 1507–1514. ISSN: 19327455. doi:10.1021/acs.jpcc.5b09740. arXiv: 1510.01371 (2016).

191. Wang, Y., Guo, Y. & Guo, W. Screening effect of monolayer van der Waals crystals on surface deicing: a molecular simulation study. *Physical Chemistry Chemical Physics* **22.** Publisher: The Royal Society of Chemistry, 27873–27881. ISSN: 1463-9084. doi:10.1039/D0CP04656F (2020).

192. Jiang, B. *et al.* Patterning Configuration of Surface Hydrophilicity by Graphene Nanosheet towards the Inhibition of Ice Nucleation and Growth. *Coatings* **12.** Number: 1 Publisher: Multidisciplinary Digital Publishing Institute, 52. ISSN: 2079-6412. doi:10.3390/coatings12010052 (2022).

193. Kimmel, G. A. *et al.* No Confinement Needed: Observation of a Metastable Hydrophobic Wetting Two-Layer Ice on Graphene. *Journal of the American Chemical Society* **131.** Publisher: American Chemical Society, 12838–12844. ISSN: 0002-7863. doi:10.1021/ja904708f (2009).

194. Xu, K., Cao, P. & Heath, J. R. Graphene Visualizes the First Water Adlayers on Mica at Ambient Conditions. *Science* **329.** Publisher: American Association for the Advancement of Science, 1188–1191. doi:10.1126/science.1192907 (2010).

195. Feng, X., Maier, S. & Salmeron, M. Water Splits Epitaxial Graphene and Intercalates. *Journal of the American Chemical Society* **134.** Publisher: American Chemical Society, 5662–5668. ISSN: 0002-7863. doi:10.1021/ja3003809 (2012).

196. Zheng, Y., Su, C., Lu, J. & Loh, K. P. Room-Temperature Ice Growth on Graphite Seeded by Nano-Graphene Oxide. *Angewandte Chemie* **125,** 8870–8874. ISSN: 1521-3757. doi:10.1002/ange.201302608 (2013).

197. Whale, T. F., Rosillo-Lopez, M., Murray, B. J. & Salzmann, C. G. Ice Nucleation Properties of Oxidized Carbon Nanomaterials. *The Journal of Physical Chemistry Letters* **6,** 3012–3016. ISSN: 1948-7185. doi:10.1021/acs.jpclett.5b01096 (2015).

198. Singla, S. *et al.* Insight on Structure of Water and Ice Next to Graphene Using Surface-Sensitive Spectroscopy. *ACS Nano* **11.** Publisher: American Chemical Society, 4899–4906. ISSN: 1936-0851. doi:10.1021/acsnano.7b01499 (2017).

199. Biggs, C. I. *et al.* Impact of sequential surface-modification of graphene oxide on ice nucleation. *Physical Chemistry Chemical Physics* **19.** Publisher: The Royal Society of Chemistry, 21929–21932. ISSN: 1463-9084. doi:10.1039/C7CP03219F (2017).

200. Häusler, T. *et al.* Ice Nucleation Activity of Graphene and Graphene Oxides. *Journal of Physical Chemistry C* **122,** 8182–8190. ISSN: 19327455. doi:10.1021/acs.jpcc.7b10675 (2018).

201. Tamtögl, A. *et al.* Motion of water monomers reveals a kinetic barrier to ice nucleation on graphene. *Nature Communications.* Publisher: Springer US, 4–11. ISSN: 2041-1723. doi:10.1038/s41467-021-23226-5. arXiv: 1810.00650 (2018).

202. Sacchi, M. & Tamtögl, A. Water adsorption and dynamics on graphene and other 2D materials: computational and experimental advances. *Advances in Physics: X* **8.** Publisher: Taylor & Francis _eprint: https://doi.org/10.1080/23746149.2022.2134051, 2134051. ISSN: null. doi:10.1080/23746149.2022.2134051 (2023).

203. Kratzer, M. *et al.* Effects of polymethylmethacrylate-transfer residues on the growth of organic semiconductor molecules on chemical vapor deposited graphene. *Applied Physics Letters* **106.** ISSN: 00036951. doi:10.1063/1.4913948 (2015).

204. Sadezky, A., Muckenhuber, H., Grothe, H., Niessner, R. & Pöschl, U. Raman microspectroscopy of soot and related carbonaceous materials: Spectral analysis and structural information. *Carbon* **43,** 1731–1742. ISSN: 0008-6223. doi:10.1016/j.carbon.2005.02.018 (2005).

205. DeMott, P. J. *et al.* The Fifth International Workshop on Ice Nucleation phase 2 (FIN-02): laboratory intercomparison of ice nucleation measurements. *Atmospheric Measurement Techniques* **11.** Publisher: Copernicus GmbH, 6231–6257. ISSN: 1867-1381. doi:10.5194/amt-11-6231-2018 (2018).

206. Häusler, T., Witek, L., Felgitsch, L., Hitzenberger, R. & Grothe, H. Freezing on a Chip-A new approach to determine heterogeneous ice nucleation of micrometer-sized water droplets. *Atmosphere* **9.** ISSN: 20734433. doi:10.3390/atmos9040140 (2018).

207. Jung, S. *et al.* Are Superhydrophobic Surfaces Best for Icephobicity? *Langmuir* **27.** Publisher: American Chemical Society, 3059–3066. ISSN: 0743-7463. doi:10.1021/la104762g (2011).

208. Abràmoff, M., Magalhães, P. J. & Ram, S. Image processing with ImageJ (2004).

209. Schindelin, J. *et al.* Fiji: an open-source platform for biological-image analysis. *Nature Methods* **9,** 676–682. ISSN: 1548-7105. doi:10.1038/nmeth.2019 (2012).

210. Bianco, G. V. *et al.* Engineering graphene properties by modulated plasma treatments. *Carbon* **129,** 869–877. ISSN: 0008-6223. doi:10.1016/j.carbon.2017.11.015 (2018).

211. *Polymethyl Methacrylate Raman Spectrum*

212. Murray, B. J. *et al.* Kinetics of the homogeneous freezing of water. *Physical Chemistry Chemical Physics* **12.** Publisher: The Royal Society of Chemistry, 10380–10387. ISSN: 1463-9084. doi:10.1039/C003297B (2010).

213. Pruppacher, H. & Klett, J. *Microphysics of Clouds and Precipitation* red. by Mysak, L. A. & Hamilton, K. ISBN: 978-0-7923-4211-3. doi:10.1007/978-0-306-48100-0 (Springer Netherlands, Dordrecht, 2010).

214. Miller, A. C. & Simmons, G. W. Copper by XPS. *Surface Science Spectra* **2,** 55–60. ISSN: 1055-5269. doi:10.1116/1.1247725 (1993).

215. Vasquez, R. P. Cu2O by XPS. *Surface Science Spectra* **5,** 257–261. ISSN: 1055-5269. doi:10.1116/1.1247881 (1998).

216. Struzzi, C. *et al.* Probing plasma fluorinated graphene via spectromicroscopy. *Physical Chemistry Chemical Physics* **19.** Publisher: The Royal Society of Chemistry, 31418–31428. ISSN: 1463-9084. doi:10.1039/C7CP05305C (2017).

217. Vasquez, R. P. CuF2 by XPS. *Surface Science Spectra* **2,** 155–159. ISSN: 1055-5269. doi:10.1116/1.1247735 (1993).

CHAPTER 6

Summary and Outlook

This work has examined graphene as an ultimately thin functional coating and concentrated on improving the underdeveloped graphene synthesis via CVD on metallurgical substrates such as iron and steels, as well as the ice nucleation behaviour of well-established CVD graphene on copper.

Chapter 3 presented a scalable approach for the production of large-scale, high-quality monolayer graphene on iron under scalable conditions. It demonstrated that the optimal growth conditions were achieved at a temperature in close proximity to the Fe-C eutectoid at 750°C. Insights into the graphene growth process were gained through in-situ material characterisation techniques (XRD and XPS), which elucidated the carbon interaction with the Fe substrate during CVD conditions. The growth of graphene was demonstrated to be isothermal under ideal conditions, with carbon precipitation towards the surface during cooling resulting in the formation of multilayer graphitic regions. In-situ XRD analysis revealed that the substrate undergoes a transformation into a pure fcc-Fe phase during hydrocarbon exposure, indicating substantial carbon diffusion into the substrate. The in-situ NAP XPS analysis demonstrated that carbon diffusion into the substrate occurs immediately upon exposure to the carbon precursor, and that saturation of the Fe subsurface with carbon is a prerequisite for isothermal surface graphene growth. The substantial uptake of carbon into the subsurface and bulk of the substrate also results in a substantial increase in surface hardness, as evidenced by nanoindentation measurements. This shows the potential to incorporate graphene growth into existing industrial surface hardening processes.

The study also addresses the challenge of persistent surface oxidation as a result of non-negligible residual oxygen under scalable CVD conditions that inhibit graphene growth due to low catalytic ability. It also suggests that the carbon precursor can act as a carbothermal reducing agent, facilitating graphene growth under the tested conditions.

The coverage of 70% monolayer and 80% overall carbon coverage constitutes a substantial improvement in scalable monolayer graphene growth on iron. Nevertheless, for application as a functional barrier coating a non-complete coverage constitutes an unacceptable problem. As mentioned, the incomplete coating is believed to be caused by competing surface oxidation of the substrate during the CVD process. This could in principle be addressed by adding a gas purification module to the CVD setup towards oxygen-free CVD, which has shown to improve quality and reproducibility for CVD graphene on copper.[118] This, however, would come at the cost of easy scalability of the process.

The role of carbothermal reduction of surface oxides is implied in this work on the basis of ex-situ measurements. To further understand the mechanism and impact of this reduction, further experiments should be conducted. For example, the controlled partial oxidation with O_2 and reduction with varying H_2 and C_2H_2 pressures during in-situ XPS could help illuminate the process.

The discussion on the impact of substrate microstructure and grain orientation on CVD graphene growth was deliberately not included in this work due to its significant added scope. In order to fully understand the system, this, of course, should be considered. For this, detailed electron backscatter diffraction (EBSD) measurements would be needed, before and after the CVD process to visualise grain size and orientation distributions. Together with correlative Raman maps of the same area after CVD, this could provide information on the impact of substrate microstructure.

Chapter 4 provided a comparison of CVD graphene growth on three archetypical steel substrates with varying complexity. It focused primarily on the in-situ NAP XPS analysis of the CVD process, which provided valuable insights and guidance towards improving the growth of carbon coating. For low-carbon, low-alloyed steel, the large-scale synthesis of high-quality monolayer graphene was achieved under non-scalable UHV conditions in the XPS system and partial monolayer graphene was grown under scalable CVD conditions. The imperfect surface conditions of the high-carbon, medium-alloyed steel were identified to interfere with ordered graphene growth. In-situ NAP XPS

showed persistent graphitic surface carbon after annealing in H_2 , which we argue could drastically decrease substrate catalytic activity and prohibit hydrocarbon decomposition. Based on this finding, we introduced an additional oxidation step, substantially decreasing the surface carbon and enabling ordered, isothermal surface carbon growth, resulting in a previously unattainable multilayer graphitic carbon coating. The high-alloyed stainless steel surface exhibited a mix of various oxide and carbide species as a result of attempted scalable CVD graphene growth. This was prescribed to the known residual oxygen in the CVD system and the high propensity of the alloying elements Cr and Mn to form oxides. Under UHV conditions, in the NAP XPS system, the surface oxides were readily reduced and a nanocrystalline carbon film with good coverage was grown on the stainless steel substrate, using the same conditions as before.

The fact that the pre-oxidation of the medium-alloyed steel resulted in a significant improvement and isothermal surface carbon growth is quite interesting and should be further explored. Firstly the pre-oxidation step could be applied in the lab-CVD system to test if this procedure translates to improved growth under scalable conditions. Secondly, the fact that isothermal surface growth, very similar to pure Fe substrates, was achieved on this substrate implies the possibility of monolayer graphene growth with improved parameters and kinetic control. This could be done with additional NAP XPS experiments, for which, however, further beamtime at a synchrotron facility would be necessary.

The already discussed issue of substrate microstructure and grain orientation is evidently even more interesting for complex steels such as the stainless CrNi-steel. However, the added complexity of course would significantly increase the experimental and analysis effort.

Chapter 5 explores the freezing behaviour of water droplets on scalably grown CVD graphene on copper. In an effort to clarify conflicting reported freezing behaviour and provide a more straightforward and statistically significant alternative to wetting angle measurements of single droplets, this study analysed thousands of freezing events on graphene-covered and reference annealed copper substrates. The study revealed a previously unreported phenomenon, termed "freezing transparency". This "transparency" could be lifted through various applied functionalisations of the graphene and is thought to be intricately substrate-dependent, based on graphene-substrate interaction. This study not only provided the first water freezing experiments on CVD graphene on copper but the freezing transparency phenomena could be of interest to the

computational community, where graphene is used as a model system for soot particles relevant for atmospheric ice nucleation. Furthermore, the effect of adventitious carbon contamination build-up through sample storage under ambient conditions in relation to ice nucleation was examined.

Further experiments could include graphene grown on different other scalable substrates such as Nickel or Iron, in order to see if the phenomenon of "freezing transparency" also translates to other substrates and provide further insight into the intricate mechanism of the graphene ice system.

Additionally, computational studies simulating the graphene-copper interaction together with surface water freezing would be conceivably complex and computationally costly but could provide invaluable insights into the underlying mechanism of water ice nucleation on graphene. This, in turn, could guide the production of a more rationally designed passive anti-icing coating.

Bibliography

118. Amontree, J. *et al.* Reproducible graphene synthesis by oxygen-free chemical vapour deposition. *Nature*. Publisher: Nature Publishing Group, 1–7. ISSN: 1476-4687. doi:10.1038/s41586-024-07454-5 (2024).

APPENDIX A

Glossary and Appendix

Abbreviations

CVD	chemical vapour deposition
MLG	monolayer graphene
FLG	fewlayer graphene
ICCP	impressed current cathodic protection
FET	field effect transistor
HOPG	highly ordered pyrolytic graphite
TMD	transition metal dichalcogenide
LPE	liquid phase exfoliation
LPCVD	low pressure chemical vapour deposition
hBN	hexagonal boron nitride
UHV	ulta-high vacuum
hBN	hexagonal boron nitride
SME	shape memory effect
IR	infrared
XPS	X-ray photoelectron spectroscopy
NAP-XPS	near ambient pressure X-ray photoelectron spectroscopy
SEM	scanning electron microscopy
TEM	transmission electron microscopy
SAED	selected area electron diffraction
XRD	X-ray diffraction
EBSD	electron backscatter diffraction

A.1 Obstacles of scalable CVD graphene growth on NiTi shape memory alloys

As discussed in section 1.2.5, the growth of graphene via CVD on alloy substrates in general and NiTi shape memory alloys in particular face complex challenges.

Using graphene CVD on NiTi (Nitinol) shape memory alloys as a case study, we illustrate the constraints arising from low catalytic activity and the tendency to form oxides due to the Ti in the NiTi alloy in terms of graphene growth results. We show that using a scalable low-temperature CVD process at 650°C we can deposit homogeneous carbon films on the NiTi, albeit at limited structural quality. Notably, we also demonstrate that our CVD process does not degrade the bulk microstructure of the NiTi during carbon deposition and importantly leaves the crystallographic shape memory effect evolution intact. This underscores the potential of CVD for depositing graphene films on NiTi alloys while emphasizing the necessity for further exploration of CVD conditions to achieve high-quality graphene deposits akin to those on prior widely investigated dedicated (often sacrificial) high-purity metal substrates such as Ni.

Prior literature has either used graphene grown on copper substrates that were transferred onto the NiTi alloy[83,84] or atmospheric pressure CVD under argon or nitrogen atmosphere[85,86], which have used temperatures of around 1000 °C. They report a native oxide layer on the substrate and that rutile TiO_2 was persistent under their conditions up to 950°C. At temperatures above 1000°C, no oxide was detected via XRD and instead a prominent TiC phase was measured, which they identified as the active substrate for graphene growth.

A.1.1 Results and Discussion

Our attempt to apply standard low-pressure CVD parameters for graphene growth on copper, which are similar to the ambient pressure recipe of Li et al.,[85] produced a severely oxidized sample without any surface carbon. Analysis with optical microscopy and Raman spectroscopy of the sample is shown in figure A.1. This indicates that our CVD system has a non-negligible amount of oxygen remaining during the process, even at a base pressure of $3e^{-3}$ mbar, which does not affect the graphene growth on copper but inhibits the growth on NiTi through the formation of persistent TiO_2 surface oxide and subsequent elimination of the substrate's catalytic activity.

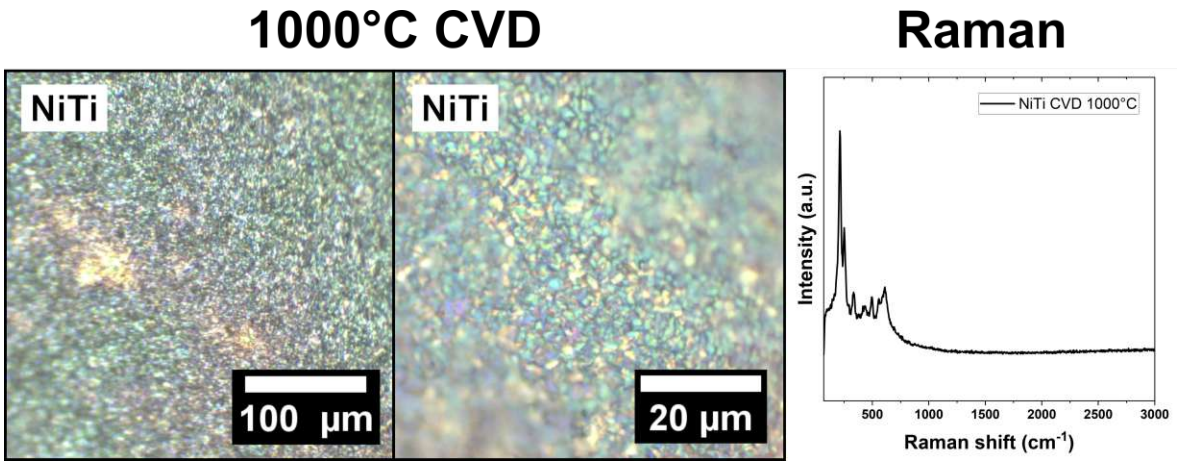

Figure A.1: Optical micrograph and Raman spectrum NiTi surface after CVD at 1000°C with CH_4 precursor. Raman spectrum shows mixed ti-oxide signal.[218]

A second approach was tried in accordance with our procedure for graphene growth on iron and steel (chapters 3,4) and used the same growth procedure. We surveyed low-temperature (650 °C to 750 °C) CVD conditions for graphene growth on NiTi using C_2H_2 as hydrocarbon precursor conditions. We chose these rather lower CVD temperatures to reduce the propensity of the NiTi substrates to undergo drastic bulk microstructure changes/degradation during the CVD process. C_2H_2 was chosen because it is the ideal hydrocarbon precursor for lower temperatures due to its high reactivity down to ~450 °C for graphene growth.[58] The substrate used was a commercial NiTi foil of 127 um thickness (Alfa Aesar, Nitinol foil, 45514, flat annealed) with a stated transition temperature martensite →austenite of ~45 °C. In the same CVD runs we also add elemental foil samples of the NiTi constituent elements, Ni (Alfa Aesar Puratonic 99.994% Nickel foil, 12046, 100µm thickness) and Ti (Alfa Aesar, 99.99% Titanium foil, 13976, 127 µm thickness), to explore differences in carbon growth behaviour for the individual elements against their equimolar alloy. Note that for Ni we expect reasonable graphitic film growth under these conditions based on our prior work,[58,60] while refractory Ti is expected to behave as a hard to grow on substrate under these temperatures based on prior work by others on similar refractory Ta substrates.[91,105] An optical micrograph and a Raman spectrum of the as-received NiTi foils are shown in Figure A.2. The optical microscopy and Raman confirm the as-received NiTi foils to be of homogeneous appearance without signs of crystalline surface oxides or prior carbon coverage.

Figure A.3 shows optical microscopy images and point localized Raman spectra of the three sample surfaces (NiTi, Ti, Ni) after a typical CVD run with 1 mbar H_2 and 1

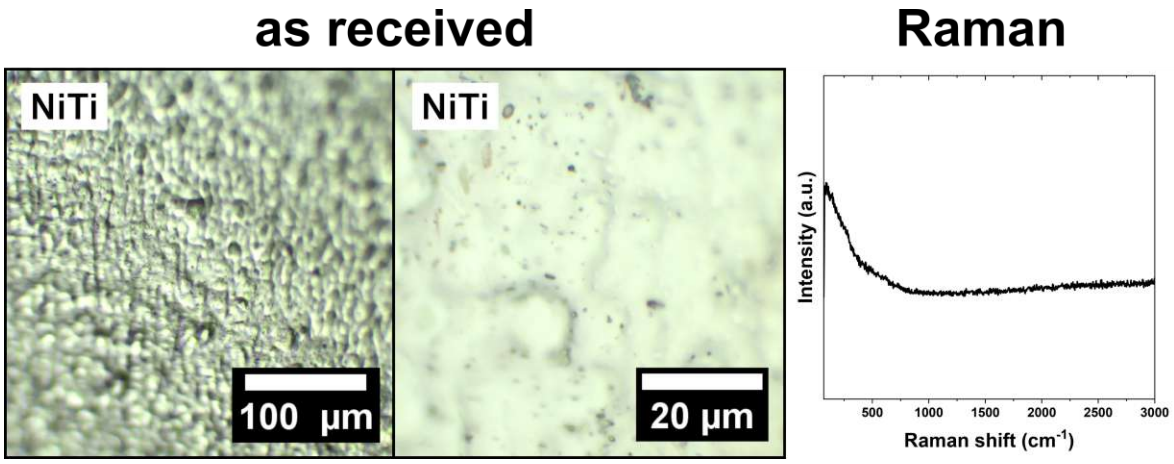

Figure A.2: Optical micrograph and Raman spectrum of as received NiTi substrate foils.

sccm C_2H_2 at 750 °C. The samples exhibit visually distinct surfaces, already indicating differences in carbon growth.

On the reference Ni a carbon coating of mixed multilayered and monolayered graphene with very low defect levels was produced, as evidenced by the sharp G and 2D peaks in the Raman spectra and the lack of an appreciable defect-related D peak.[102,149] We note however that 1 sccm C_2H_2 is a too high flux of carbon feeding for Ni compared to our prior optimized homogeneous monolayered Ni recipes,[58,60] which translates to too fast carbon feeding on the highly catalytically active Ni substrates leading to the observed mixed multilayer and monolayer graphene growth.[102] Ni would thus show better-controlled graphene growth a lower carbon fluxes (<0.1 sccm C_2H_2 in our system).[58,60] We however note that for the NiTi and Ti substrates we find that C_2H_2 fluxes <1 sccm under otherwise constant conditions led to diminishing carbon coverage down to practically no carbon-related Raman signals after CVD (not shown). Therefore here only the 1 sccm C_2H_2 results are presented and the Ni results serve only as an internal reference in terms of certainly achievable graphitisation under these conditions with an established graphene CVD catalyst. We note that the Ni shows no signs of surface oxidation after CVD growth in Raman. This shows that our here employed CVD system has suitable low oxygen and water residual trace levels for typical graphene catalysts.[134,147] In contrast to the clear graphitic Raman features and high structural graphene quality on the Ni, the NiTi shows carbon deposition of much lower structural quality, whereby the carbon Raman spectra on NiTi in Figure A.3 are best attributed to an amorphous carbon film fully covering the substrate. This is evidenced by the broad, merging D and G peaks and the lack of an appreciable 2D peak.[149] Additionally, the NiTi shows clear signs of Ti-oxide (TiO2) formation on the

surface during the CVD process in the Raman in Figure A.3.[218,219] This implies that the scalable CVD conditions that we have applied are low enough in residual oxygen and water traces in the process atmosphere to avoid oxidation of Ni but that for the addition of refractory Ti, which is a much stronger oxygen getter than Ni, our vacuum conditions are not sufficiently controlled with respect to oxygen/water traces to avoid oxidation during CVD for the NiTi sample. The formation of the amorphous carbon layer is found to be present all over the NiTi surface in Figure A.3 and the formation of the Ti-oxide is also indicated by the change in colour in the optical micrographs in Figure A.3 after CVD compared to the as received state of the NiTi foil in Figure A.2.

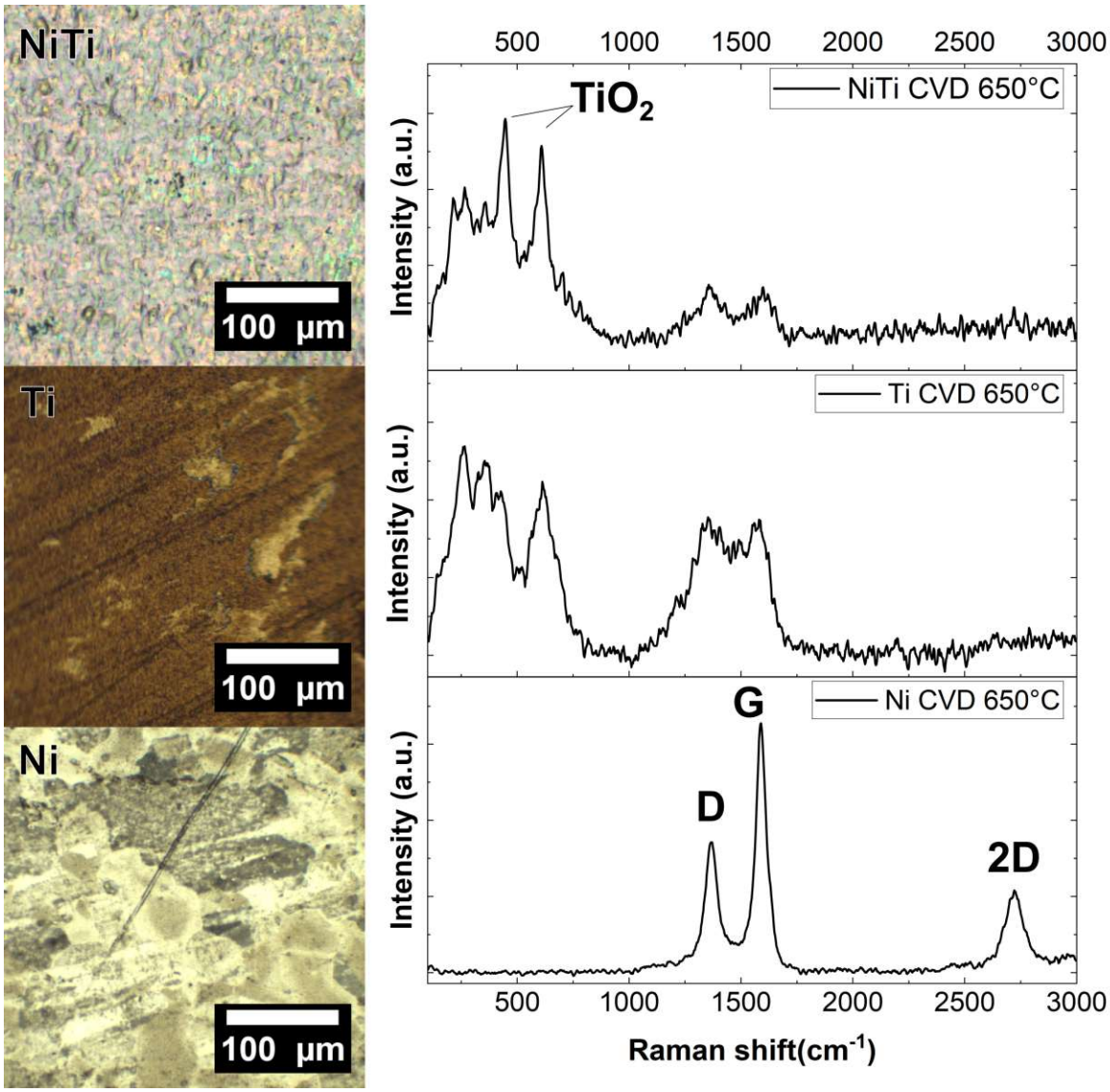

Figure A.3: Raman of second NiTi CVD experiments

Notably, in terms of Raman quality our CVD results on the NiTi in Figure A.3 are not too dissimilar to prior literature on graphene CVD on NiTi and were in particular

grown at much lower temperature (650 °C – 750 °C instead of 1000 °C).[85,86] Compared to established recipes on other (non-refractory) substrates the structural quality of the deposited carbon film ("amorphous carbon") is however still quite poor and open to improvement. Additionally, concurrently with the amorphous carbon deposition, surface oxidation of the NiTi substrate has occurred, which is also undesired.

The Raman spectrum for the Ti reference in Figure A.3 similarly only shows the growth of amorphous carbon and similar surface oxidation to TiO_2 under our CVD conditions. Thereby, a comparison of the reference growths on Ni and Ti, indicates that the low structural quality growth results on NiTi arise from the Ti in the NiTi compound. This implies that the 50:50 mixture of Ni and Ti in the NiTi is, in terms of catalytic properties toward carbon deposition and resistance against oxidation, more dominated by the Ti properties than by the Ni properties. This highlights the problem of lacking activity for graphene CVD from an alloy substrate (here NiTi) even if one principal component element itself is usually catalytically active (here, Ni).[58,60]

To further improve our graphene CVD on NiTi future work will therefore need to explore a wider set of kinetic conditions (temperatures, pre-treatments, carbon precursors, feeding rates, etc.) to overcome the limitation of insufficient substrate catalytic activity towards graphene growth from the Ti component.

Nevertheless, our here presented carbon films on NiTi at 650 °C – 750 °C are not too dissimilar in structural quality to prior work and grown at substantially lower temperatures.[85,86] Therefore, we proceed to check if the CVD process has detrimentally impacted the NiTi bulk microstructure properties,[86] which would be a highly detrimental factor in 2D materials CVD on metallurgical substrates, as outlined above, or if the NiTi bulk microstructure functionality has been retained throughout the graphene CVD process. A key test for preservation of bulk microstructure functionality in NiTi is the exhibition of the SME, which is known to be dependent on the preservation of suitable martensitic/austenitic NiTi microstructure evolution with temperature.[220]
In order to check if the basic shape memory property has been preserved post CVD, in-situ XRD measurements were conducted, which are shown in figure A.4. A reference untreated NiTi sample and the CVD treated sample were heated in steps of 20°C to a temperature of 100°C in two separate experiments. Please note that the expected martensite →austenite transition temperature for our NiTi substrates is ~45 °C. The as-received NiTi sample shows both austenitic and martensitic phases at room temperature, characteristic for this composition.[121]

As it is heated to 40°C the martensitic peaks disappear and a complete change to the austenitic phase is observed. No additional changes occur when increasing the temperature to 100°C. This is in excellent agreement with the stated martensite →austenite transition temperature of ~45 °C. Upon cooling some of the martensitic features reappear forming again a mixture of martensite and austenite, albeit the austenitic peaks have become more prominent. This run is thereby typical for exhibiting the reversible martensitic/austenitic phase transformation (with some hysteresis) as a function of temperature that is responsible for the SME.[220] We therefore take this behavior as a reference for a functional SME XRD evolution and compare in the following if the graphene CVD process has impacted on this SME XRD evolution.

For the amorphous carbon covered NiTi after graphene CVD, the XRD diffractogram at room temperature shows a similar mixture of martensitic and austenitic NiTi phases (International Centre for Diffraction Data (ICDD), PDF-5+ database, powder diffraction file entries: martensite: 04-015-5901, austenite: 04-002-7201) like in the as received reference NiTi sample. Additionally however rutile and anatase TiO_2 signals as well as a Ni_3Ti phase are detected. (Rutile: 04-001-7847, Anatase: 04-004-3579, Ni_3Ti: 04-007-1577) The TiO_2 phases are readily explained by the surface oxidation already observed in Raman in Figure A.3. The existence of the Ni_3Ti phase shows the extent of the surface oxidation, which formed TiO_2 and left the NiTi subsurface region with an excess of Ni, leading to the formation of Ni_3Ti. Upon heating to 40°C, the CVD-treated NiTi sample undergoes the same transformation towards the full austenitic NiTi phase like the untreated as received NiTi reference sample. The oxide and Ni_3Ti phases are stable and do not change. Again, no further changes occur when increasing the temperature to 100°C. Upon cooling, the post CVD NiTi sample regains all of the martensitic phase peaks, converting back to the original state. Combined, the in situ XRD data shows that the SME XRD evolution overall has not been affected by the CVD process. This is a strong indication, that the CVD process has left the SME property of the NiTi intact, just as desired.

A.1.2 Conclusions

In summary, we have here exemplified the challenges of 2D material synthesis on complex metal alloy substrates discussed in section 1.2.5, by presenting graphene CVD results on the shape memory alloy NiTi. We show that due to the low catalytic activity in the NiTi arising from the Ti, graphene growth is currently restricted to homogeneous

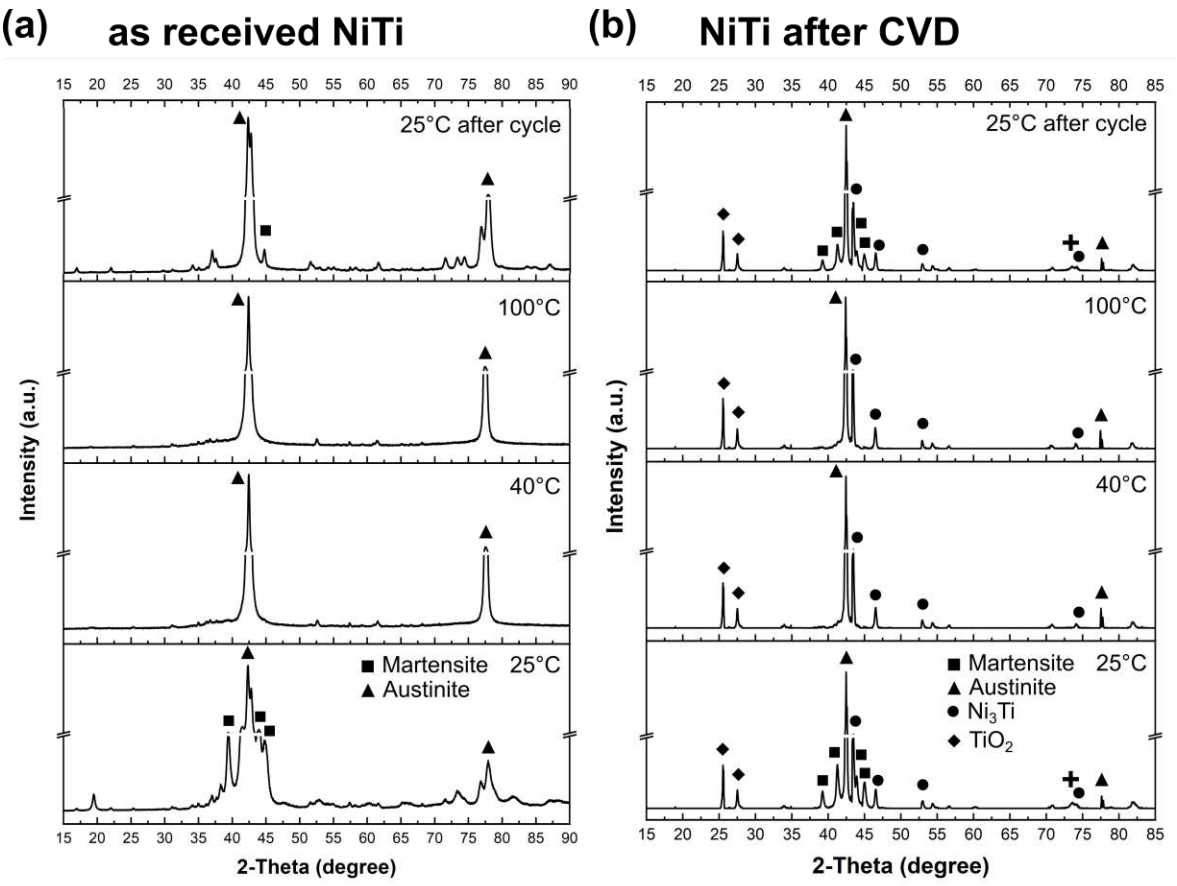

Figure A.4: (a) Temperature-resolved in-situ XRD of as received NiTi substrate, showing a temperature cycle to 100°C with martensitic (■, International Centre for Diffraction Data (ICDD), PDF-5+ database, powder diffraction file entry: 04-015-5901) and austenitic (▲, 04-002-7201) NiTi phases indicated. (b) Temperature-resolved in-situ XRD of NiTi substrate after CVD process at 650°C. Salient phases are indicated. As loaded, at 25°C austenitic NiTi (▲, 04-002-7201), maternsitic NiTi (■, 04-015-5901), Ni_3Ti (●, 04-007-1577) and TiO_2 (◆, Rutile 04-001-7847, Anatase 04-004-3579) are present. We note that the background of the in situ XRD patterns was manually treated in order to remove signals from the sample holder. This manual background treatment does not affect the measured structural evolution associated with the NiTi samples.

but low quality amorphous carbon coatings instead of high quality graphene. Also the propensity of Ti to oxide formation makes the NiTi samples susceptible to surface oxidation from oxygen/water residues in the CVD atmosphere, which is much less of a problem for standard graphene CVD catalysts like Ni. Nevertheless, our scalable low temperature recipe at 750 °C yields carbon films not too dissimilar to prior work on graphene CVD on NiTi. Notably, we here also demonstrate that our CVD process does not degrade the majority bulk martensite/austenite phases of the NiTi and importantly leaves the crystallographic SME evolution intact. This shows that CVD of 2D films on metallurgical NiTi substrates is possible while retaining their desired bulk functionality, but that more work on kinetic CVD condition exploration on the NiTi is necessary to

achieve similarly high quality carbon deposits towards good quality graphene as we have prior achieved on dedicated high-purity elemental catalyst substrates like Ni.

A.2 Publication Notice

This section has been accepted for publication and is listed as number 3 in the publication list.

A.3 Ice Nucleation Figure

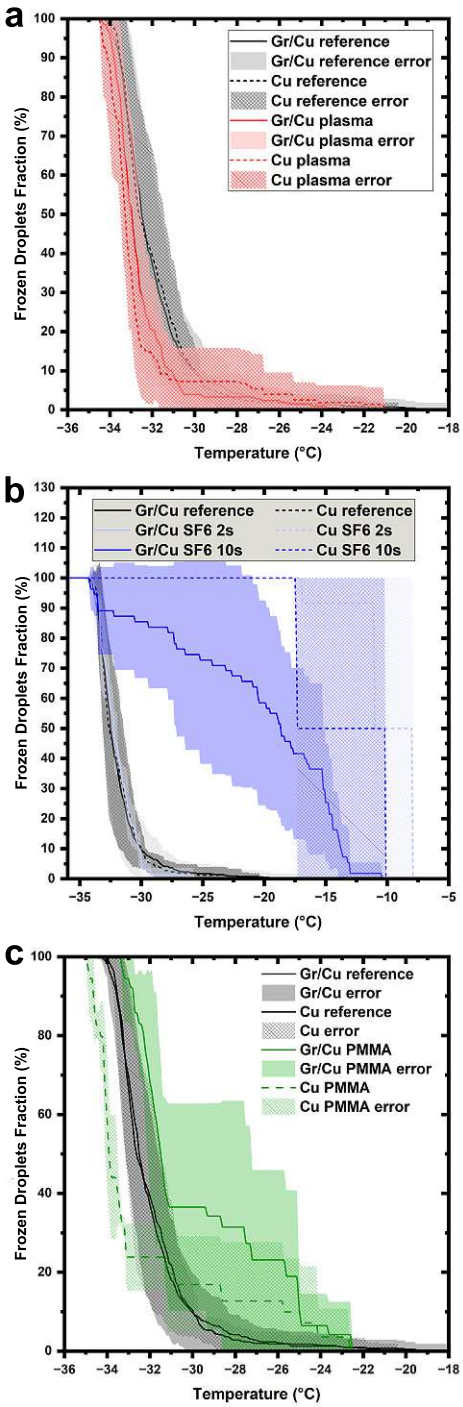

Figure A.5: Replot from Figure 5.11 with uncertainty bands from standard deviations as shaded areas added.

Bibliography

58. Weatherup, R. S. *et al.* In situ characterization of alloy catalysts for Low-temperature graphene growth. *Nano Letters* **11,** 4154–4160. ISSN: 15306984. doi:10.1021/nl202036y (2011).

60. Weatherup, R. S. *et al.* On the Mechanisms of Ni-Catalysed Graphene Chemical Vapour Deposition. *ChemPhysChem* **13,** 2544–2549. ISSN: 1439-7641. doi:10.1002/cphc.201101020 (2012).

83. Podila, R., Moore, T., Alexis, F. & Rao, A. M. Graphene coatings for enhanced hemo-compatibility of nitinol stents. *RSC Advances* **3,** 1660–1665. ISSN: 20462069. doi:10.1039/c2ra23073a (2013).

84. Zhang, L. *et al.* Graphene enhanced anti-corrosion and biocompatibility of NiTi alloy. *NanoImpact* **7,** 7–14. ISSN: 2452-0748. doi:10.1016/j.impact.2016.10.003 (2017).

85. Li, J. *et al.* CVD growth of graphene on NiTi alloy for enhanced biological activity. *ACS Applied Materials and Interfaces* **7,** 19876–19881. ISSN: 19448252. doi:10.1021/acsami.5b06639 (2015).

86. Zou, J., Wang, X., Zhang, P. & Du, X. Ultrafast flame coating of carbon and chemical vapor deposition of graphene on NiTi alloy to enhance its corrosion resistance. *Diamond and Related Materials* **128,** 109231. ISSN: 0925-9635. doi:10.1016/j.diamond.2022.109231 (2022).

91. Nazarova, M. *et al.* Growth of graphene on tantalum and its protective properties. *Carbon* **139.** Publisher: Elsevier Ltd, 29–34. ISSN: 00086223. doi:10.1016/j.carbon.2018.06.027 (2018).

102. Bayer, B. C. *et al.* In Situ Observations of Phase Transitions in Metastable Nickel (Carbide)/Carbon Nanocomposites. *Journal of Physical Chemistry C* **120,** 22571–22584. ISSN: 19327455. doi:10.1021/acs.jpcc.6b01555 (2016).

105. Fan, X. *et al.* Chemical vapor deposition of graphene on refractory metals: The attempt of growth at much higher temperature. *Synthetic Metals* **247,** 233–239. ISSN: 0379-6779. doi:10.1016/j.synthmet.2018.12.016 (2019).

121. Sanjabi, S., Sadrnezhaad, S. K., Yates, K. A. & Barber, Z. H. Growth and characterization of TixNi1−x shape memory thin films using simultaneous sputter deposition from separate elemental targets. *Thin Solid Films* **491,** 190–196. ISSN: 0040-6090. doi:10.1016/j.tsf.2005.06.004 (2005).

134. Fickl, B. *et al. Controllable Freezing Transparency for Water Ice on Scalable Graphene Films on Copper* 2024. doi:10.48550/arXiv.2403.15629. arXiv: 2403.15629[cond-mat].

147. Fuchs, D. *et al.* Electrochemical Behavior of Graphene in a Deep Eutectic Solvent. *ACS applied materials & interfaces* **12,** 40937–40948. ISSN: 1944-8252. doi:10.1021/acsami.0c11467 (2020).

149. Ferrari, A. C. Raman spectroscopy of graphene and graphite: Disorder, electron-phonon coupling, doping and nonadiabatic effects. *Solid State Communications* **143,** 47–57. ISSN: 00381098. doi:10.1016/j.ssc.2007.03.052 (2007).

218. Frank, O. *et al.* Raman spectra of titanium dioxide (anatase, rutile) with identified oxygen isotopes (16, 17, 18). *Physical Chemistry Chemical Physics* **14,** 14567–14572. ISSN: 14639076. doi:10.1039/c2cp42763j (2012).

219. Ohsaka, T., Izumi, F. & Fujiki, Y. Raman spectrum of anatase, TiO2. *Journal of Raman Spectroscopy* **7,** 321–324. ISSN: 10974555. doi:10.1002/jrs.1250070606 (1978).

220. Bayer, B. C. *et al.* Carbon nanotube forest growth on NiTi shape memory alloy thin films for thermal actuation. *Thin Solid Films* **519,** 6126–6129. ISSN: 00406090. doi:10.1016/j.tsf.2011.03.044 (2011).